Advancements in Non-Enzymatic Nucleic Acid Diagnostics for Point-of-Care Testing Using Enantiomeric Left-Handed DNA

By

Zackary A. Zimmers

Dissertation

Submitted to the Faculty of the

Graduate School of Vanderbilt University

in partial fulfillment of the requirements

for the degree of

DOCTOR OF PHILOSOPHY

in

Biomedical Engineering

September 30, 2021

Nashville, Tennessee

Approved:

Frederick Haselton, Ph.D.

Anita Mahadevan-Jansen, Ph.D.

Todd Giorgio, Ph.D.

David Wright, Ph.D.

Jonathan Schmitz, Ph.D., M.D

TABLE OF CONTENTS

Page

ACKNOWLEDGEMENTS

First, I would like to thank my loving and supportive fiancé Lynn, who has been there for me through the best and worst parts of this process. A huge thank you goes to Dr. Haselton for the years of mentorship which helped shape me into the scientist I am today. Thank you to my committee members, Dr. Wright, Dr. Mahadevan-Jansen, Dr. Schmitz, and Dr. Giorgio, for your wisdom and advice as I made new discoveries and formed new hypotheses. I would also like to thank the two undergraduate students who provided invaluable help over the years. Alex Boyd helped me to build the prototype autoPiLOT device, and Hannah Stepp collected a great deal of data during the final months as I raced to the finish line. A grand and sweeping thank you goes to all of my colleagues, Stephanie Pearlman, Dalton Nelson, David Evans, Nick Spurlock, Emily Kight, and Nicole Malofsky; you've all provided intellectual and emotional support over the years. Thank you to Dr. Adams for your additional mentorship and expertise, and Dr. Pask for keeping the lab running and making all of our research possible. Finally, thank you to my family, whose lifelong support is the reason I am here today writing my Thesis Dissertation.

LIST OF TABLES

LIST OF FIGURES

LIST OF ABBREVIATIONS

DNA: Deoxyribonucleic acid. “Nucleic acids” typically refers to both DNA and RNA (ribonucleic acid), which are closely related and both composed of nucleotides.

D-DNA: Right-handed DNA. This is the naturally-occurring form of DNA present in living systems.

L-DNA: Left-handed DNA. A synthetic form of DNA which is the chiral mirror-image of D-DNA.

dsDNA: Double-stranded DNA.

ssDNA: Single-stranded DNA.

cf-DNA: cell-free DNA.

bp: base-pair. dsDNA sequence lengths are typically described in bp, as opposed to just bases (nucleotides).

NAT: Nucleic acid test. This refers to any diagnostic test which detects the presence of nucleic acids.

PCR: Polymerase chain reaction. A gold standard diagnostic test which amplifies DNA using thermal cycling and enzymatic activity.

CHA: Catalyzed hairpin assembly. This is a non-enzymatic nucleic acid test which the presence of a target nucleic acid catalyzes a chain reaction of opening DNA hairpins.

TMSD: Toehold-mediated strand displacement. This is a type of reaction in which a single strand displaces one strand in a dsDNA duplex.

FRET: Förster (or fluorescence) resonance energy transfer. A phenomenon in which energy is transferred between two chromophores; this process is often used during fluorescence imaging.

ANOVA: Analysis of variance. A type of statistical test used to analyze the variance in samples means caused by one specific variable.

PAGE: Polyacrylamide gel electrophoresis. A technique used to separate molecules based on their size and electrical charge.

BSA: Bovine serum albumin. Often used as a protein standard in laboratory protocols.

U1, U1*, and U2: The dumbbells used in the autoPiLOT amplification assay. U1* is a modified version of U1 for binding to the target sequence.

Chapter 1

1. INTRODUCTION

1.1 Schistosomiasis: A Neglected Tropical Disease

Burden on public health.

Schistosomiasis is a leading neglected tropical disease, with over 240 million people infected worldwide across 76 countries.[2, 3] The neglected nature of this disease is due in part to the fact that the symptoms are not as severe as some other tropical infectious diseases; schistosomiasis is a chronic disease which decreases the quality of life over a long period of time. In fact, it is responsible for the loss of an estimated 4.5 million disability-adjusted life years.[3] The other factor preventing schistosomiasis, also known as bilharzia, from receiving more attention is its localization to resource-poor settings. Schistosomiasis is promoted by poor sanitation, flourishing in areas where water sanitation standards are not sufficient to control the spread of disease. The disease is caused by infection with one of six species of parasitic flatworm in genus *Schistosoma*: *S. mansoni*, *S. japonicum*, *S. haematobium*, *S. intercalatum*, *S. malayensis* and *S. mekongi*. Of these, *S. mansoni* is the most widespread species; it can be found in sub-Saharan Africa, the middle east, and the Americas.[4, 5] Of the estimated 400 million people at risk of infection worldwide, over 90% reside in sub-Saharan Africa and are at risk of *S. mansoni* infection.[6]

Parasite life cycle.

The schistosome life cycle is complex and includes many unique stages; this life cycle is illustrated in **Figure 1**. Schistosome development requires a freshwater snail as an intermediate host, which localizes infection to sources of freshwater where the appropriate snail species can live. The eggs are secreted inside the human host and enter the water via the feces or urine. *S. haematobium* is the only species in which the adult worm resides in the bladder and eggs are secreted via urine; all other species inhabit the mesenteric veins which connect to both the small intestine and the hepatic veins, resulting in secretion of eggs via

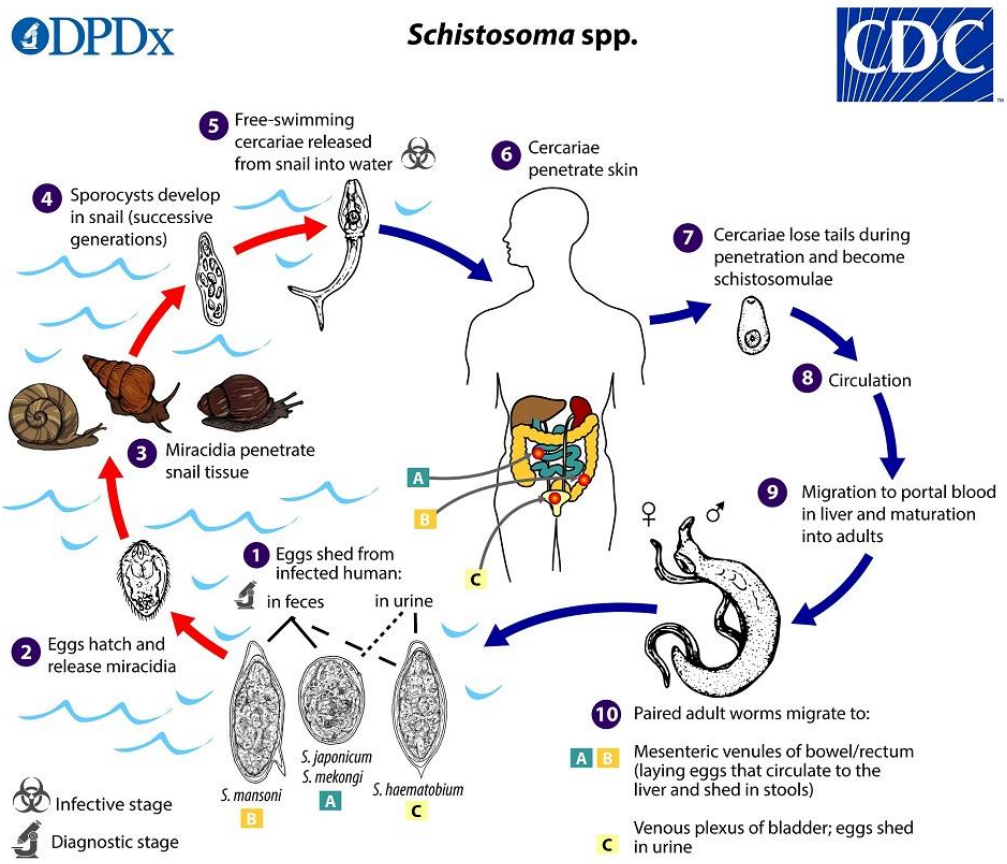

Figure 1. The life cycle of Schistosoma species though both the snail intermediate host and the human primary host. Figure adapted from CDC website for schistosomiasis: https://www.cdc.gov/parasites/schistosomiasis/biology.html.

feces.[7, 8] Once in the water, the eggs hatch to release miracidia, which swim until they find the snail intermediate host. After entering the intermediate host, the miracidia develop into mother sporocysts which reproduce asexually to produce daughter sporocysts. The daughter sporocysts also reproduce asexually, producing several generations and eventually producing cercariae, the infectious life stage for humans. After exiting the snails, the cercariae are able to swim freely until they find a human host to enter via tissue penetration, often the feet or legs. Inside the human blood vessels, the cercariae develop into schistosomula and travel to the lungs via the blood vessels or the lymphatic vessels. Once in the lungs, further development transforms the schistosomula into worms that can travel into the veinous system. Here, worms enter the final stage of their complex life cycle and become adults seeking a sexual partner. This duo of adult worms travels together to the final destination, which varies depending on species. For *S. mansoni*, as well as most

other *Schistosoma* species, this location is the mesenteric veins. Here, eggs are produced by the female and released into the host.

Disease pathology.

After initial infection by the cercaria, symptoms may arise including an itchy rash at the site of penetration, fever, fatigue, coughing, eosinophilia, and occasionally even weight loss or hepatosplenomegaly.[7, 9, 10] These early symptoms are also known as Katayama Fever; however, up to 50% of patients remain asymptomatic at this stage.[11-13] Beyond Katayama Fever, the body's immune response is caused by the release of eggs, rather than the worms themselves. Chronic schistosomiasis triggered by the secretion of eggs causes inflammation and scarring of the tissue. Eggs which become lodged in the tissue and do not escape the body trigger the formation of granulomas. In the intestine, this can cause abdominal pain, bleeding, and diarrhea. In the liver, this can cause inflammation, periportal fibrosis, portal hypertension, splenomegaly, and even internal bleeding.[9, 14, 15] Over time, symptoms tend to become more severe as more eggs accumulate in the body. Although more rare, released eggs can also enter the brain and cause cerebral schistosomiasis, which is much more difficult to diagnose.[16] Schistosomiasis is also an important disease during pregnancy, as it can neonatal prematurity and increased maternal morbidity.[17]

Disease prevention and treatment.

Currently, there is no available vaccine for schistosomiasis. Therefore, the primary method to reduce infections is improved water sanitation; a meta-analysis of schistosome infection rates found a significant correlation between water sanitation and infection rates.[18] Improving water sanitation practices is a multi-faceted and complex problem for many schistosomiasis-endemic areas, where there is often a lack of resources, knowledge of proper practices, or both. Additionally, largescale changes in infrastructure like this take a long time to enact. An alternative strategy is to eliminate populations of the snail intermediate host. Water treatment with molluscicides has shown promise, although they are typically toxic to aquatic plants, fish, and amphibians as well.[19, 20] Some naturally-derived essential oils have demonstrated

molluscicidal properties, but further studies are needed to validate their efficacy and ecotoxicity.[21] Although both of these strategies, improved infrastructure/sanitation and elimination of the intermediate host, are valuable long-term goals, human treatment will still be necessary for the short-term future, and may still prove the most effective method to control schistosomiasis.

The World Health Organization (WHO) has set guidelines for the control and eventual elimination of schistosomiasis; these guidelines involve administering treatment to school-age children based on the prevalence of infection in the area.[22] Praziquantel is an effective treatment for all disease-causing species of schistosomes, and the WHO guidelines use this drug as a first line of defense and prevention for children, who are typically considered the most at-risk. The administration of treatment varies based on reports of infection prevalence; under-treatment fails to protect people from infection, while over-treatment is expensive and may contribute to Praziquantel-resistant parasites.[23, 24] Therefore, it is crucial to obtain accurate regional evaluations of disease prevalence through widespread and accurate diagnostic testing. Not only do powerful diagnostic tests increase our ability to identify and subsequently treat infected individuals, but they help to guide large-scale treatment programs designed to curb the spread of disease.

Diagnostic strategies.

The current standard for diagnosis of *S. mansoni* is known as the Kato-Katz technique, which involves microscopic examination of a fecal sample for eggs.[25] The Kato-Katz technique is simple to perform and provides a quantitative measure of parasite load (eggs/gram of feces), but it requires complex equipment and trained personnel to judge microscopic images. Additionally, the test lacks the sensitivity to reliably identify positive cases, and is subject to variation between users.[26, 27] Egg count varies from day-to-day, necessitating multiple samples for an accurate diagnosis. One study found that by examining a single slide created from a single stool sample, only 22 of 69 positive samples were detected.[28] Testing 12 duplicate slides from a single stool sample raised this number to 38 of 69. Testing duplicate slides of the following three stool samples (for a total of 18 slides created from four stool samples) raised the number of positives to 64 of 69. Additional techniques were required for the remaining five positive samples to be

identified. This example highlights the high workload, variability, and sub-optimal sensitivity of the Kato-Katz technique.

Serological assays which detect antibodies against worms or egg antigens offer an alternative diagnostic strategy to the Kato-Katz method.[9] An evaluation of the performance of many leading serological tests found them to have sensitivities ranging from 41% - 78%, and specificities ranging from 76% - 100%.[29] While promising, these tests still suffer from poor sensitivity. Additionally, antibodies persist in the blood even after a complete cure of infection, meaning many patients may test positive due to past infections.[7, 29] Diagnostic tests which use eggs or antibodies as a biomarker suffer from drawbacks; the ideal biomarker is one that can be detected with high sensitivity and specificity, and does not persist after the infection has been cured.

1.2 Nucleic Acids as Biomarkers

Background.

Nucleic acids, namely DNA and RNA, have emerged as leading biomarkers for diagnostic technologies, as they allow for extremely specific discrimination of targets via Watson-Crick base-pair binding. Each nucleotide binds selectively with a partner – thymine to adenine and guanine to cytosine – which allows for the formation of double-stranded DNA (dsDNA) when the sequences are complementary. Advances in nucleic acid tests (NATs) such as polymerase chain reaction, rolling circle amplification, and loop-mediated isothermal amplification have taken advantage of this predictable hybridization behavior to detect a variety of diseases with very high sensitivity and specificity, including Zika virus, malaria, cancer, and others.[30-33] The specificity and sensitivity of NATs can be attributed to the recognition and amplification steps, respectively (shown in **Figure 2**). The recognition step occurs when DNA which has been designed to bind to the target sequence is added to the sample. Assuming sample preparation was successful, this DNA will recognize the target nucleic acids – and only the target nucleic acids – and bind to them. The amplification step is facilitated by one or several enzymes which, if the target sequence was recognized, amplify the target nucleic acid by creating copies of them. Once the target has been amplified, there are

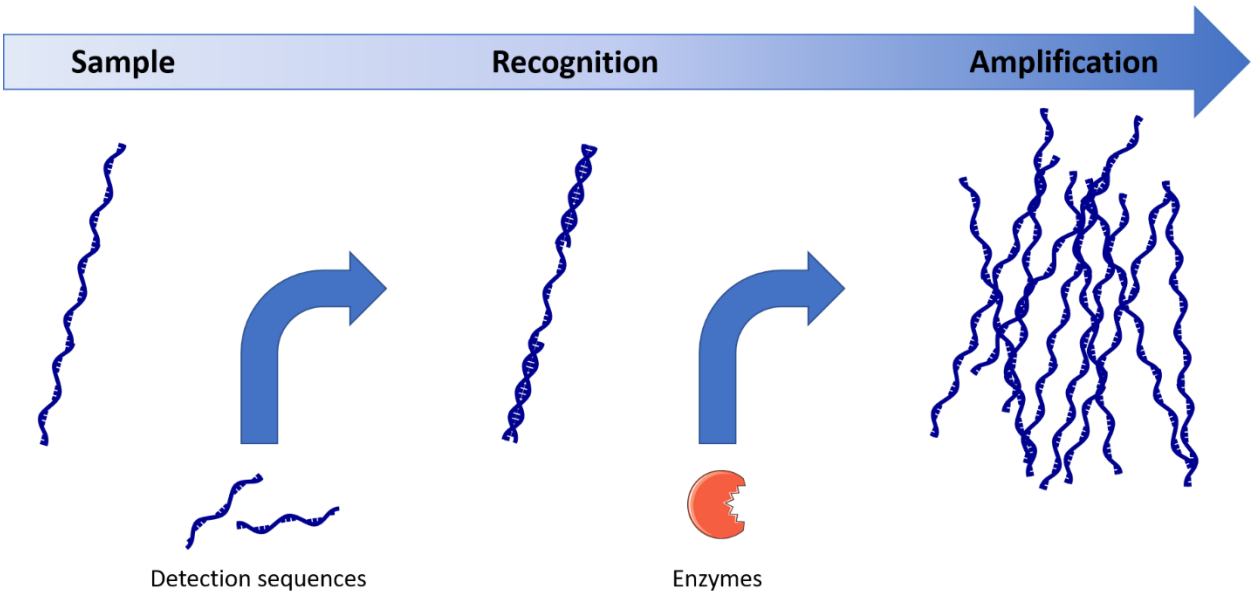

Figure 2. Overview of the general enzymatic nucleic acid test workflow. Detection sequences are added to the sample, and bind with the target sequence if present. Enzymes are also added to the reaction, and these are able to create copies of the target sequence.

numerous techniques to detect the now billions of copies of DNA, including gel electrophoresis, fluorescence, and colorimetry.[34-36]

The previously-mentioned NATs rely on one or more enzymes for amplification of the target sequence. Enzymatic NATs pose several challenges due to the delicate nature of enzymes. They require resource-intensive storage conditions and cold chain management, as well as labor-intensive sample preparation methods to ensure ideal reaction conditions.[1, 37, 38] Additionally, enzymes are typically the most expensive component in the reaction. These conditions preclude the use of such tests at the point-of-care, especially in low-resource settings. Therefore, non-enzymatic NATs have the potential to be especially valuable for point-of-care testing in the developing world, where infectious diseases such as schistosomiasis are endemic.

Currently, there is no known technique for creating copies of target DNA without the use of enzymes. Instead, non-enzymatic NATs utilize DNA hybridization events to amplify a target-induced signal, rather than the target itself. The most important tool in the toolbox of non-enzymatic NATs is toehold-mediated strand displacement (TMSD). This process is outlined in **Figure 3**, where 1, 2, 1', and 2'

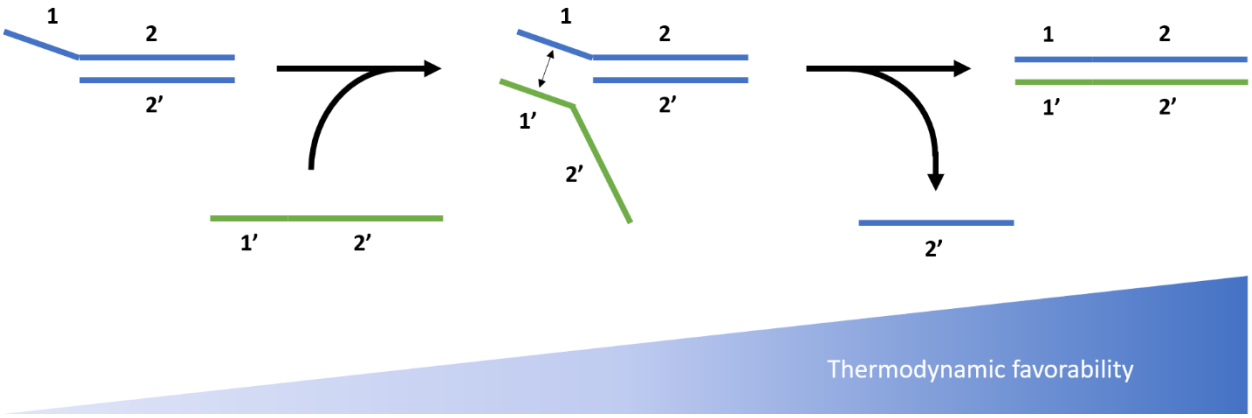

Figure 3. Overview of the toehold-mediated strand displacement (TMSD) reaction. The strand 1'-2' binds to the exposed toehold of the partially double-stranded structure. The unbound portion of 1'-2' then replaces the strand 2' via branch migration, removing the strand 2' completely.

are used to denote binding domains on the DNA strands. Domain 1 is complementary to 1', and 2 to 2'. In this example, the initial partially double-stranded structure has a single-stranded toehold (domain 1). This toehold allows for the incoming strand to bind, starting at the toehold and then migrating to occupy the sites previously occupied by the strand 2'. Once this process is complete, the strand 2' is no longer bound at all; it has been replaced by the strand 1'-2'. Thus, there are three steps in the TMSD reaction: toehold binding, branch migration, and release. The reaction is thermodynamically-driven; the final double-stranded DNA structure is thermodynamically favorable to the initial partially double-stranded structure. Through logical design of DNA circuits which contain double-stranded, partially double-stranded, and single-stranded structures, a variety of functionalities may be achieved, including non-enzymatic NATs.[39, 40]

Catalyzed hairpin assembly (CHA) has risen to prominence as a promising non-enzymatic NAT. CHA, which was first described by Yin and Pierce in 2008,[41] relies entirely on strand displacement reactions between a catalyst strand and a pair of DNA hairpins. Hairpins are single-stranded DNA structures with self-complementary regions that form a double-stranded stem region with a single-stranded loop region in between (H1 and H2 in **Figure 4**). These hairpins can coexist in a metastable state because their complementary regions are sequestered in the stem regions, preventing them from binding to one another. A catalyst sequence (C in **Figure 4**) is able to open one hairpin via TMSD, revealing a previously-occluded binding domain. The opened hairpin then interacts with the toehold of the second hairpin in a second TMSD

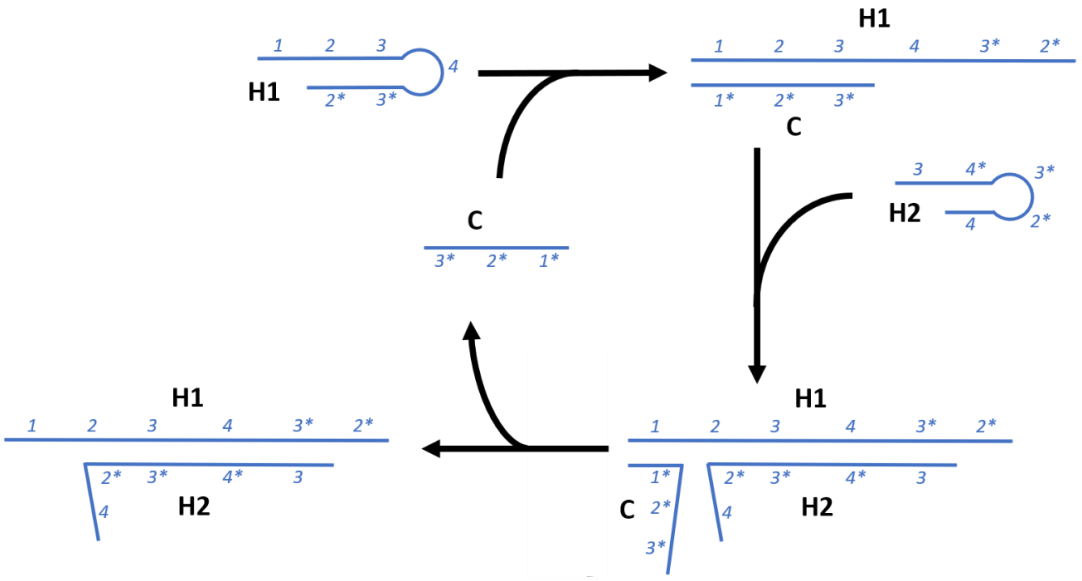

Figure 4. Reaction mechanism for a catalyzed hairpin assembly (CHA) reaction. The two hairpins H1 and H2 are stable unless the catalyst sequence C is present. The catalyst sequence facilitates a conformational change in H1, which in turn facilitates the binding of H2. H2 then displaces C so it may be recycled and catalyze the assembly of further hairpin pairs.

reaction, displacing the catalyst sequence for further assembly of subsequent hairpin pairs. This technique requires no advanced equipment or labor-intensive sample preparation, and has successfully detected target sequences at concentrations as low as 5 pM in several hours.[42] These features make CHA an attractive test for use at the point-of-care in detecting nucleic acid biomarkers of infectious disease.

Beyond just catalyzed hairpin assembly, many other closely-related techniques have been demonstrated which combine a basic DNA amplification circuit with another technique to improve performance. For example, Wei et. al. coupled CHA with hybridization chain reaction, a closely-related DNA amplification circuit, to increase the limit of detection.[43] Yin et. al. coupled hybridization chain reaction with the phenomenon of plasmon-enhanced fluorescence, in which the signal from fluorescent molecules is magnified by proximity to a nanoscale noble metal surface.[44] Tang et. al. combined CHA with a bio-barcode assay in which gold nanoparticles are bound via target DNA to magnetic beads.[45] These secondary probes are then chemically dissolved, liberating thousands of additional oligonucleotides from the surface of the nanoparticles for catalytic action in the CHA reaction. These techniques of course impose

their own challenges, such as increased reaction time, complexity, or cost, but demonstrate nonetheless the ability of DNA nanomachinery to create powerful diagnostic tools without the aid of enzymatic activity.

Roadblocks for non-enzymatic NATs.

Although non-enzymatic NATs such as CHA overcome some challenges (labor, cold chain, cost) associated with enzymatic NATs, enzymes are powerful molecules, and non-enzymatic NATs face their own challenges operating without enzymatic assistance. One such challenge is ubiquitous among all non-enzymatic NATs: circuit leakage. In the world of electronic circuits, leakage is used to describe the transfer of electrons across a boundary where there is not meant to be any transfer, such as the flow of current across a transistor in the "off" state. In DNA circuits, the term is used to describe an analogous problem in which signal amplification is observed in the absence of the catalyst sequence.[46, 47]

Several factors can contribute to leakage, including mis-formed or mis-synthesized hairpins, but the root of the problem is stochastic fluctuations in the hybridization state of circuit elements. DNA base-pairing is a chemical reaction and as such exists in an equilibrium state. Even when the equilibrium state is stable, there is always a chance that any individual DNA duplex may spontaneously "breathe", or temporarily unbind. When this process occurs in a CHA hairpin, the reactive segment in the stem region is revealed, a process normally only triggered by the presence of the catalyst sequence. The resulting non-specific amplification – that is, increase in signal not triggered by the target catalyst – is difficult to distinguish from legitimate amplification when there are low levels of target DNA present, and the magnitudes of target-specific and non-specific amplification are similar. Not only does this decrease the sensitivity of the test, it makes the testing of biological samples particularly difficult because the leakage rate is likely to vary from sample to sample due to varying reaction conditions. The rate of leakage is fundamentally determined by the chemical properties of the reaction solution, and is therefore affected by varying pH, salt concentrations, or other reaction inhibitors. If the exact reaction conditions are known, then a parallel no-target control reaction can be performed to determine the leakage. Different biological samples, however, are suspect to have different conditions, making the formation of a no-target control

impossible. Even as innovations in diagnostic DNA circuit techniques continue to advance the field, the phenomenon of circuit leakage remains a fundamental challenge.

Another roadblock facing DNA circuit NATs is sub-optimal sensitivity. Accurate and early diagnosis is required of any diagnostic test to prevent the spread of infectious disease, even in individuals with very low levels of pathogen. TMSD-driven DNA circuits are not typically capable of achieving sufficient signal amplification to detect sub-picomolar levels of nucleic acid target, which would be expected in samples from patients with low pathogen levels.[42, 44, 48] Contributing largely to this sub-optimal amplification are linear amplification dynamics; in CHA, a single catalyst sequence can bind to a single hairpin, catalyzing the formation of a single hairpin-hairpin complex before it is recycled to bind to another hairpin. If we consider a cycle of CHA to be the time required for one hairpin pair to assemble, then each target strand assembles one pair per cycle. In theory, this process would happen over and over until all hairpins have been opened, but in practice this is far from the case. The linearity of this reaction limits the amplification to many orders of magnitude lower than that of PCR, which exhibits exponential amplification.[46] Each thermal cycle of PCR allows polymerase to copy every target strand, doubling the overall number of targets sequences.

Recently, nonlinear DNA amplification circuits have been demonstrated using a number of strategies. The Ellington group recently described a cascading CHA reaction that utilized additional layers of hairpin pairs, each hairpin pair catalyzed by the assembly of the previous layer.[46] With increased amplification, however, came increased leakage. A single spuriously-opened hairpin could set off a cascade of subsequent hairpin assemblies, leading to an explosive increase in leakage compared to traditional CHA. Although 7000-fold amplification was demonstrated using cascaded CHA, extreme measures were taken to minimize leakage, including denaturing PAGE, native PAGE, and biotin-based purification. Another type of nonlinear DNA circuit, branched hybridization chain reaction, is similar in that additional pairs of hairpins are added which are triggered by the opening of the initial two hairpins.[49] In this case, the hairpins bind to each other to form a large, multi-branching structure. Other examples of nonlinear amplification include hyperbranched hybridization chain reaction and dendritic growth schemes facilitated by double-

stranded substrates and single-stranded assistants.[50, 51] These techniques are all prone to leakage just like traditional CHA; in this case, however, the downstream effect of spuriously-opened hairpins is much larger due to the exponential amplification schemes. This makes the reaction leakage twitchier and more difficult to predict, greatly complicating the testing of "dirty" biological samples with varying reaction conditions.

A roadblock faced by any diagnostic point-of-care test is the process of patient sample collection and purification. There are many types of samples which have been shown to contain clinically-relevant biomarkers, including blood, sputum, urine, tissue scrapings, tears, and feces.[52-57] Each of these sample types poses its own unique challenges involving collection and purification steps. The choice of which sample type to collect is influenced by the disease, equipment available, and type of diagnostic test. Blood and serum are perhaps the most common choice of sample type, as nucleic acids which escape the host cells can circulate freely in the blood. The collection and storage of blood, however, requires trained personnel and medical equipment, making the process difficult in low-resource settings. Additionally, cultural taboos sometimes discourage patients from seeking testing which includes a blood-draw.[58] After collection, NATs require sample purification steps to remove reaction inhibitors and create regular, buffered reaction conditions. These purification steps increase the cost and complexity associated with the test. Non-enzymatic NATs may gain some flexibility without needing to meet the strict conditions required for enzymes, but sample purification is still required to remove biological material which would contribute to background signal, or block signal entirely. A previous study which performed CHA on raw biological samples showed that the background fluorescence buried the relevant signal.[59] An ideal point-of-care test for use in low-resource settings involves both non-invasive sample collection and minimal processing/purification steps.

In summary, there are three primary roadblocks to the use of non-enzymatic NATs at the point-of-care. First, the signal caused by circuit leakage cannot be distinguished from legitimate signal without the use of a no-target control, complicating the application to biological samples. Second, linear amplification provides insufficient amplification for many applications, and nonlinear amplification shows promise but

is hindered by increased leakage. Third, sample collection and purification steps add complexity and cost which prevent widespread application of sensitive NATs at the point-of-care, or in low-resource settings.

Overcoming roadblock 1: separation of leakage signal from target signal.

Despite advances in DNA amplification circuits such as CHA, their reliance on reversible DNA hybridization reactions will always result in some level of non-specific amplification caused by leakage. A new type of DNA circuit that incorporates a built-in control to measure leakage in the same tube as target would be ideal for diagnostic applications. By specifically measuring the amplification arising from leakage alone, the target-induced amplification signal can be corrected to account for leakage. To accomplish this, we turn to left-handed DNA.

DNA is a chiral molecule, meaning that it is asymmetrical and has identical but opposite right-handed and left-handed forms. All naturally-occurring DNA is right-handed (D-DNA), but mirror image left-handed DNA (L-DNA) can be synthesized in a laboratory. L-DNA is identical in chemical composition, and has been shown to exhibit identical solubility, thermodynamic properties, and binding properties as its

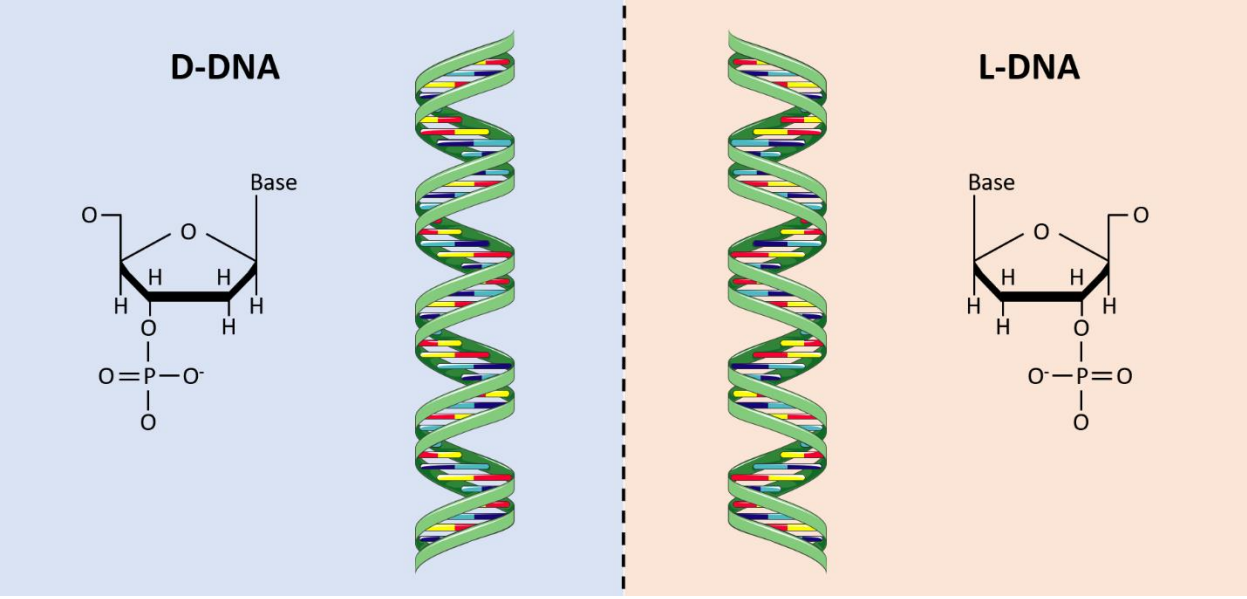

Figure 5. Right-handed D-DNA and left-handed L-DNA are chiral enantiomers. Each individual nucleotide is either right-handed or left-handed; the resulting spiral of double-stranded DNA is also right-or left-handed, depending on the chirality of the nucleotides.

right-handed enantiomer.[60-62] L-DNA is resistant to enzymatic degradation and, importantly, does not cross-hybridize with D-DNA whatsoever. These properties have led to the use of L-DNA in nuclease-resistant aptamers, microarray tags, biologically-inert cellular probes, and hybridization state sentinels in PCR.[63-66] These properties make L-DNA perfectly suited to serve as a parallel amplification circuit built in to a diagnostic test. Since it does not exist in nature, the L-DNA circuit theoretically will not be triggered specifically by any DNA present in a biological sample; the only observed amplification will therefore be caused by circuit leakage. With identical physical properties, we expect the leakage of the L-DNA circuit to match that of the D-DNA circuit. In this way, the L-DNA circuit would act as a no-target control built-in to the same reaction as the target signal.

Overcoming roadblock 2: increasing sensitivity via nonlinear amplification.

Numerous DNA amplification circuits have been previously described which utilize additional DNA elements to achieve nonlinear amplification, but in general they offer only modest increases in sensitivity due to a corresponding increase in leakage. Recently, an alternative DNA amplification scheme was described in which two so-called DNA "dumbbells" (U1 and U2 in **Figure 6**) with complementary sticky ends are able to bind to each other, forming a network of connected dumbbell units.[1] Each dumbbell has four sticky ends and is therefore capable of binding four complementary dumbbells. For example, dumbbell U1 can bind four U2 dumbbells, each of which is then able to bind another three U1 dumbbells, and so on. Unlike most DNA circuits in which the reactive domains are hidden in hairpin stems or other dsDNA structures, the DNA dumbbells undergo no changes in conformation to drive the reaction. Instead, the two dumbbells are kept separate and added one at a time to the immobilized target DNA, creating a chain of DNA linkages. Since each dumbbell can bind multiple of the next dumbbell, this scheme exhibits exponential amplification.

The authors who first demonstrated the exponential dumbbell amplification used magnetic beads to immobilize the target DNA, and sequentially incubated the beads with U1, removed U1 and washed beads, incubated with U2, removed U2 and washed beads, and repeated this process for many cycles. Each

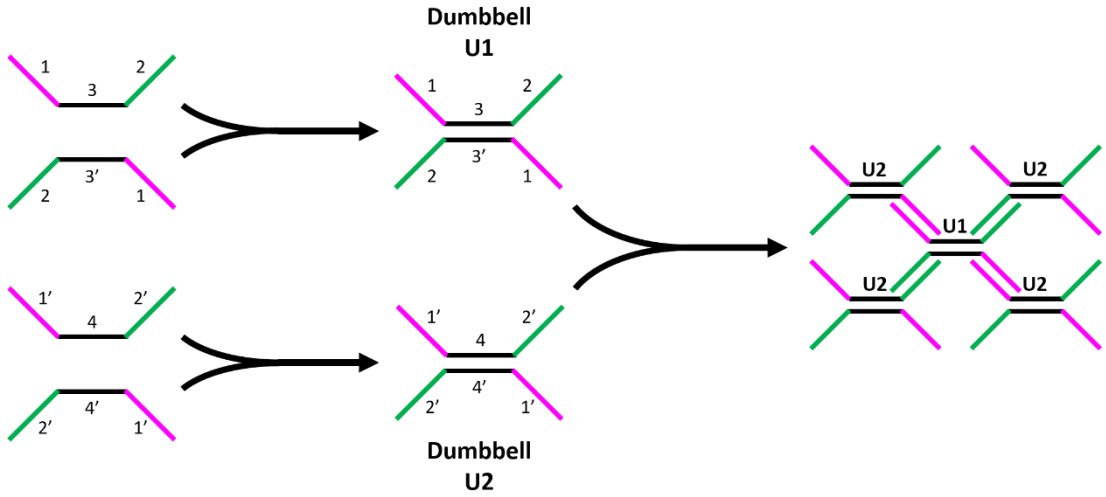

Figure 6. DNA dumbbell overview. Dumbbells U1 and U2 are partially double-stranded complexes composed of the sequences U1-a/U1-b and U2-a/U2-b, respectively. Each dumbbell has four binding domains for the opposite dumbbell, facilitating exponential growth.

dumbbell was modified with a terminal biotin so that a final incubation with avidin-labeled (biotin and avidin have a very strong affinity for each other) horseradish peroxidase bound a number of enzymes proportional to the number of dumbbells. These horseradish peroxidase enzymes then catalyzed a color change of tetramethylbenzidine substrate, which acted as a diagnostic readout of the test. This technique was reported to have a limit of detection of 5 copies/reaction, but required 35 cycles of dumbbell incubations and washes. Performance of this many pipetting steps is extremely labor-intensive, uses a high volume of reagents, and has a total reaction time of approximately 18 hours. Despite the excellent reported sensitivity, these drawbacks prohibit the use of this test at the point-of-care.

Our laboratory has previously developed techniques for automatic sample processing based on magnetic bead transport through pre-arrayed fluid chambers separated by surface tension valves.[67-69] By applying this type of sample processing to the dumbbell amplification reaction, the reaction can theoretically be automated to greatly reduce the amount of labor and opportunities for human error, as well as the total amount of required reagents. When the magnetic beads are transported across the surface tension valves, they travel in a small cluster formed by the presence of a magnetic field from a small exterior magnet.[70] This cluster of beads carries over trace amounts of liquid from the previous fluid chamber; in a

dumbbell DNA reaction where the two dumbbells are in separate fluid chambers, this would result in cross-contamination of the dumbbells. Anticipating that this, as well as non-specific adhesion of dumbbells to the beads, will cause a rising non-specific signal, identical L-DNA dumbbells can be added to act as a control. Much like previously described in the CHA reaction, identical L-DNA elements provide an orthogonal binding system that should exhibit amplification identical to the non-specific amplification of the target signal.

Overcoming roadblock 3: urine as a point-of-care sample for S. mansoni detection.

The presence of cell-free DNA (cf-DNA) in both serum and urine is well-documented, and this cf-DNA is a biomarker of growing interest for diagnostic purposes.[71-73] One study found that *S. mansoni* cf-DNA appeared in blood beginning just three days after infection, compared to the seven weeks before eggs appear in the feces.[74] The presence of cf-DNA in urine makes urine an ideal sample candidate for collection and testing in low-resource settings; its non-invasive nature circumvents the barriers to sample collection, such as trained personnel, equipment, cultural taboos, and patient age.

cf-DNA escapes cells as they decay and circulates freely in the blood; small fragments can then pass through the kidneys and into the urine. Enzymatic NATs which detect cf-DNA in urine have previously been developed for *Schistosoma mansoni*, *Mycobacterium tuberculosis*, *Plasmodium* species, and others.[75-78] *S. mansoni* is a particularly attractive target for urinary cf-DNA for several reasons. First, as previously mentioned, cf-DNA appears in the urine starting three days after infection, opening up accurate diagnostic results to the recently-infected. Second, schistosomes undergo a particularly high rate of parasite turnover, leading to a comparably large amount of cf-DNA liberated from dying parasite cells and released into the bloodstream.[71] Additionally, a 121-bp tandem repeat DNA sequence has been described which comprises approximately 12% of the *S. mansoni* genome, resulting in roughly 600,000 copies of the sequence per cell.[26, 79] Taken together, these qualities suggest that there are bountiful amounts of *S. mansoni* DNA available for testing in urine, and sooner after infection than other biomarkers such as eggs. Furthermore,

this DNA is evenly distributed in the urine, overcoming the problem of random sampling in feces which hampers test sensitivity.[80]

Taking note of the aforementioned features, others have used PCR to detect *S. mansoni* DNA in urine.[28, 81, 82] The drawbacks of enzymatic NATs such as PCR have previously been described; PCR detection of urinary cf-DNA comes with an additional challenge. Next-generation sequencing has revealed that the vast majority of DNA fragments found in urine range from 30-200 bases in length.[83] The distribution of these fragment sizes suggests that many of the available DNA fragments in urine are shorter than the 110-bp region amplified by the PCR assay. The non-enzymatic NATs previously described detect shorter DNA sequences (20-30 bases), suggesting that a much larger fraction of available fragments are relevant targets for these tests, compared to PCR.

Traditionally, the process for extracting DNA from urine involved either the use of organic solvents or commercial kits, making the process undesirably hazardous or expensive. A simpler and less expensive method, known as the salting out and resin method, was developed in 2010 for extracting *S. mansoni* DNA from urine.[84] Even this method, however, requires several hours and multiple centrifugation steps, which is not always realistic for use at the point-of-care. Magnetic bead-based extraction methods offer a quick and easy alternative; previously-developed magnetic bead methods have shown low-resource-compatible extraction of urinary DNA.[85, 86] DNA is bound via surface-functionalized magnetic beads and extracted from the sample via an external magnetic field. The beads can be transported through any number of pre-arrayed fluid chambers to replace manual pipetting steps. This presents an easier and faster method of urinary cf-DNA extraction which is easily interfaced with downstream processing steps. Combined with powerful non-enzymatic diagnostic strategies, all the pieces are in place for a low-resource, point-of-care diagnostic test detecting *S. mansoni* DNA in urine samples.

1.3 Thesis Goals and Overview

Throughout this dissertation, I work to overcome each of the previously-described obstacles to the use of non-enzymatic NATs at the point-of-care. In Chapter 2, I investigate the effects of different

fluorescent-labeling strategies on DNA hybridization. One of the crucial components of this work is measuring the signals from both D-DNA and L-DNA elements. To distinguish these two signals, different fluorescent labels can be attached to the end of the sequences. A huge variety of fluorophores and quenchers are widely available for modification during oligonucleotide synthesis, with distinct fluorescent signatures. In this chapter I examine many different fluorescent designs and their effects on DNA hybridization, with the ultimate goal of informing the design of parallel D-DNA and L-DNA structures which will exhibit identical behavior, despite having different modifications for fluorescent detection. As a model reaction to demonstrate the effects of fluorescent label design strategies, I use a type of PCR in which optical measurements from labeled L-DNA is used to signal switching between heating and cooling.

In Chapter 3, I develop a dual-chirality CHA reaction which uses parallel D-DNA and L-DNA circuits to measure both target signal and circuit leakage. The reaction characteristics are compared both with and without the inclusion of L-DNA to determine whether the addition of a second, orthogonal DNA circuit affects performance. The dual-chirality design is tested in a variety of leakage-affecting sample conditions to evaluate whether L-DNA amplification is a consistent measure of D-DNA leakage. While only CHA is studied here, this novel dual-chirality design should be applicable to other types of DNA circuits as well.

In Chapter 4, I use a dumbbell DNA amplification scheme to investigate whether exponential amplification, similar to that seen in PCR, can be achieved in a non-enzymatic NAT. To reduce the amount of hands-on time and reagents required, as well as the number of opportunities for human error, I develop an automated microfluidic system controlled by a Raspberry Pi microcomputer to carry out the amplification reaction. Real-time fluorescence measurements are used to measure signal amplification. As in Chapter 3, parallel L-DNA elements are included to measure the non-specific amplification and eliminate the need for a no-target control. These features are intended to make this test feasible at the point-of-care for detection of *S. mansoni* DNA. In this vein, I investigate the limit of detection of the reaction, and the performance when applied to the detection of *S. mansoni* DNA.

Perhaps the most significant innovation of this work is the use of enantiomeric L-DNA as a built-in control reaction for non-enzymatic NATs. Although L-DNA, once relatively unknown, is becoming more utilized in recent years, no one as of yet has applied it for this purpose. Non-enzymatic NATs reliance on reversible DNA hybridization means some level of leakage will always be expected, and have to be accounted for with no-target controls. A dual-chirality design removes the need for a second parallel reaction, and opens the door to testing biological samples which may cause irregular leakage profiles. Another innovation of this work is the quantification of fluorescent labeling strategies effect on DNA hybridization. These effects are often overlooked, because in a single-chirality design there is no second signal, and therefore no second set of hybridization characteristics to measure up against. The third innovation of this work is the cyclical transport of magnetic beads to perform the dumbbell DNA amplification reaction. Previous studies have shown one-directional transport of beads through several processing solutions, but never before have they been moved back and forth between two solutions to grow a network of DNA attached to the bead surface. This presents a completely new type of magnetic bead-based reaction, which can be applied to other types of sample processing steps as well. Finally, the elimination of schistosomiasis requires widespread and accurate diagnostic testing, and infection rates are highest in low-resource settings without easy access to a laboratory. The application of non-enzymatic NAT for detection of *S. mansoni* is novel, and represents a large step toward a low-resource point-of-care test for schistosomiasis.

Chapter 2

2. FLUOROPHORE-QUENCHER INTERACTIONS EFFECT ON HYBRIDIZATION CHARACTERISTICS OF COMPLEMENTARY OLIGONUCLEOTIDES

Adapted from "Fluorophore-quencher interactions effect on hybridization characteristics of complementary oligonucleotides." *Analytical Methods* 11.22 (2019) with permission from The Royal Society of Chemistry.

2.1 Introduction

Optical detection of nucleic acids allows for highly specific and sensitive detection of a variety of targets.[87-90] Due to the variety of applications, including genomic analysis, detection of analytes, and amplification monitoring during PCR, many different nucleic acid fluorescent biosensor formats have been engineered.[91, 92] One such format is the use of an intercalating dye, which binds to the major or minor groove of double-stranded DNA (dsDNA) to produce a fluorescent signal.[93] A major downside of intercalating dyes, however, is that the fluorescence is not sequence-specific; any dsDNA can provide a binding site for the dye. For sequence-specific detection of nucleic acid hybridization, many formats rely on the modulation of fluorescence from a fluorophore via proximity to a quenching molecule.[94-96] In order to monitor hybridization of a specific oligonucleotide, the nucleic acids of interest are often covalently modified to contain terminal fluorophores and quenchers. Binding events are revealed by either bringing the donor and acceptor fluorophores together and permitting energy transfer, or separating them to cease energy transfer.

Quencher molecules reduce fluorescence via fluorescence resonance energy transfer (FRET), a process in which fluorescent energy from the donor molecule is transferred to the acceptor molecule.[89, 95] FRET is most effective when the donor and acceptor molecules are within a radius of 2-10 nm. In terms of nucleic acid fluorescent labels, a quenched fluorescent signal indicates that the two labeled strands are annealed. Quenching can also occur through direct contact when the donor and acceptor are very close, diminishing the fluorescence of both molecules and instead releasing energy primarily as heat.[95] This type

of quenching is known as contact-mediated quenching or contact quenching. Both contact-mediated and FRET-mediated quenching may occur with a variety of quenching molecules, including dyes such as Dabcyl and Black Hole Quencher, other particles such as gold nanoparticles and carbon nanotubes, and even single nucleotides.[95, 97, 98]

The use of fluorophore/quencher pairs presents a convenient and powerful method to simultaneously monitor the hybridization of both right-handed and left-handed DNA. Chiral molecules, a category that DNA falls under, are found in one of two enantiomeric conformations, often denoted as the right-handed and left-handed forms. Perhaps the most attention is given to chirality in the pharmaceutical industry, where drug administration authorities often require enantiomerically pure drug synthesis.[99] Additionally, enantiomers play an important role in organic synthesis and materials components.[100] Left-handed DNA (L-DNA) is the enantiomer of naturally-occurring right-handed DNA (D-DNA), and was first reported in 1984.[101] L-DNA exhibits identical solubility, duplex stability, and selectivity as its right-handed counterpart, but does not hybridize with D-DNA whatsoever and is resistant to enzymatic degradation.[61, 102] These properties have led to the utilization of L-DNA in molecular beacons and DNA microarrays with enhanced specificity, as well as therapeutic aptamers with enhanced stability.[61, 65, 103-105] For applications where an optical readout is desired, L-DNA may be fluorescently-labeled with fluorophores and quenchers much the same as D-DNA. Previous studies have shown, however, that these modifications can affect the thermodynamic properties of the DNA duplex.[106-108] To aid in the development of dual-chirality diagnostics which utilize both chiral forms of DNA, we must first study the effects of different labeling strategies on DNA, with the ultimate goal of designing fluorescent labels for D-DNA and L-DNA which allow them to be differentiated without differentially affecting their hybridization behavior.

As a model reaction system which utilizes both D-DNA and L-DNA, we turn to adaptive PCR to study the effects of different fluorescent labeling strategies. adaptive PCR is a method of performing PCR in which the hybridization state of fluorescently-labeled L-DNA is optically monitored, and used as a sentinel for the hybridization state of unlabeled D-DNA in the same reaction.[66] Thermal cycling of the reaction mixture is therefore controlled based on the optical signal, rather than temperature measurements,

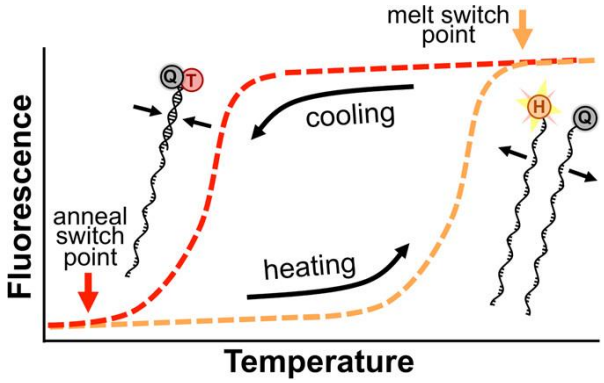

Figure 7. Outline of the process for controlling thermal cycling in adaptive PCR. The melting of the L-DNA target-analogs (labeled with grey "Q" in diagram) produces an optical signal that indicates the melt switch point. The annealing of the L-DNA primer-analogs (labeled with red "T" in diagram) to the complementary target-analogs produces a signal indicative of the cooling switch point. Figure adapted with permission from Adams et. al., *Analytical Chemistry*, 2017.

as shown in **Figure 7**. During heating, the signal from L-DNA target-analogs indicates when all the DNA has melted, as the target is longer and has the highest melt temperature. During cooling, the signal from the L-DNA primer-analogs indicates when the primers have annealed and polymerase is able to extend them into full length targets. The underlying assumption is that the observed hybridization state of fluorescently-labeled L-DNA accurately reflects that of the D-DNA in the reaction. By observing the performance of adaptive PCR using different fluorescent design strategies, we are able to evaluate the effect of these design strategies on hybridization behavior.

2.2 Materials and Methods

Oligonucleotides.

Analysis of DNA hybridization temperature was performed using primers from an established PCR detection protocol for malarial parasite *Plasmodium falciparum*.[69] Primers and the complementary portion of target DNA were purchased from Integrated DNA Technologies (Skokie, IL). Identical left-handed oligonucleotides were purchased from Biomers.net (Ulm, Germany). A complete list of oligonucleotide sequences is given in **Table 1**. For studies using fluorescently-labeled oligonucleotides, sequences were

Table 1. Oligonucleotide sequences used in Chapter 2.

	Description	**5' mod**	**3' mod**	**Sequence (5' – 3')**
Hybridization experiments	Primer			ACATGGCTATGACGGGTAACG
	Target			CGTTACCCGTCATAGCCATGT
	Fluorescent primer-analog	fluorophore		ACATGGCTATGACGGGTAACG
	Target-analog 0-base offset		BHQ-2	CGTTACCCGTCATAGCCATGT
	Target-analog 5-base offset		BHQ-2	CGTTACCCGTCATAGCCATGTTAGGT
	Target-analog 10-base offset		BHQ-2	CGTTACCCGTCATAGCCATGTTAGGT CAATA
	Target-analog Guanine quench			CGTTACCCGTCATAGCCATGTG
PCR experiments	Forward primer			TGGTAAATGTGCTCATGTGTTT
	Reverse primer			AGTTTCGGATGTTACAAAACTATAGT
	Target			TGGTAAATGTGCTCATGTGTTTAAACTT ATTTTTAAAGAGATTAAGGATAATATTT TTATTTATATTTTAAGTATTATTTATTTA AGTGTATGTGTAATGAATACAATTTTTG CTAAAAGAACTTTAAACAAAATTGGTA ACTATAGTTTTGTAACATCCGAAACT
	Hydrolysis probe	Texas Red	IBRQ	GTAATGAA(T)(A)(C)(A)A(T)T(T)TTGCT
	L-DNA primer-analog	FAM		TGGTAAATGTGCTCATGTGTTT
	L-DNA target-analog 0 offset		BHQ-2	AAACACATGAGCACATTTACCA
	L-DNA target-analog 10 offset		BHQ-2	AAACACATGAGCACATTTACCAAGACA AGAAC
	L-DNA target-analog guanine quench			AAACACATGAGCACATTTACCAG

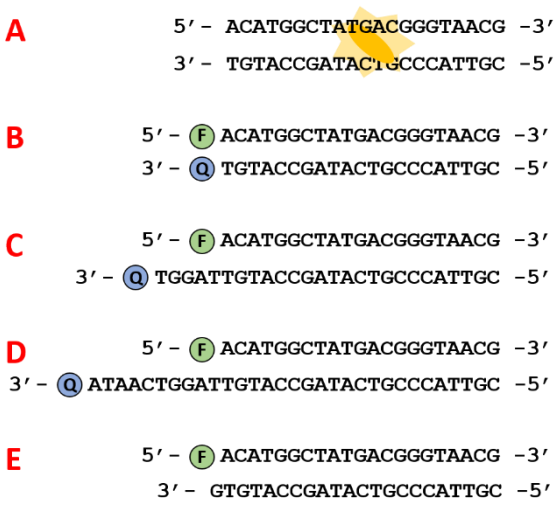

Figure 8. Fluorescence designs for detecting DNA hybridization. **A.** Unlabeled DNA is measured with SYTO 82 intercalating dye. **B, C, D.** Quenching with BHQ-2 offset from the fluorophore by 0, 5, and 10 bases, respectively. **E.** Guanine quenching.

purchased with Black Hole Quencher 2 (BHQ-2) covalently attached to the 3' end of the target strand, and fluorophores attached to the 5' end of the primer strand. Fluorophores tested include FAM (ex/em 495/520 nm), HEX (ex/em 535/556 nm), Texas Red (ex/em 596/615 nm), ROX (ex/em 575/602 nm), ATTO Rho101 (ex/em 586/610 nm), and Cy5 (ex/em 649/666 nm). Versions of the quencher-modified target strand were also ordered with the quencher offset by an extra 5 or 10 bases on the 3' end. The extra bases to create this offset were taken from the neighboring *P. falciparum* genetic code. Tests with guanine-quenching replaced the 3' BHQ-2 with a single guanine base. These different fluorescence designs are shown in **Figure 8**.

PCR experiments were performed using previously described *P. falciparum* target DNA, corresponding primers, and hydrolysis probe.[109] L-DNA oligonucleotides with identical sequence as the forward primers were purchased from Biomers.net with 5' FAM fluorophores. Complementary oligonucleotides were purchased with 3' BHQ-2 with no offset, 3' BHQ-2 with a 10-base offset, and a 3' guanine. These sequences are listed in full in **Table 1**. The hydrolysis probe, used to generate signal as the target DNA was amplified, utilized a 5' Texas Red and a 3'Iowa Black RQ quencher (IBRQ). Bases in parenthesis indicate locked nucleic acid bases, which have enhanced affinities for their complementary bases compared to normal nucleotides.

Annealing temperature experiments.

Annealing curves (also called melt curves, depending on if temperature increasing or decreasing) were obtained using a Qiagen Rotor-Gene Q. Samples were 25 µL in volume and contained both fluorophore-labeled DNA and quencher-labeled reverse complement at final concentrations of 100 nM in 1X VersaTaq PCR buffer. The samples were raised to an initial temperature of 90 °C and allowed to reach thermal equilibrium. The temperature was then lowered at a rate of 1 °C/minute to a final temperature of 50 °C. Fluorescence was measured at each temperature, and this data was used to extrapolate the annealing temperature. A full explanation of this process can be found in **Appendix 1**.

Annealing temperatures were calculated for each of the 24 possible fluorescent designs (6 different fluorophores and 4 different quenching designs), and each sample was tested in triplicate to determine a mean and 95% confidence interval. Additionally, unmodified oligonucleotides were analyzed using SYTO 82 intercalating dye at a concentration of 10 µM. This dye has been previously shown to have less of an impact on DNA hybridization than other dyes, shifting the annealing temperature less than 0.4 °C at 10 µM.[110] Quenching efficiencies were also calculated by comparing samples containing the quencher-labeled strand to identical samples without any quencher. A two-sample t-test was used to determine whether the quenching method affected quenching efficiency.

Effect of P:T ratio on annealing temperature.

Once more using the Qiagen Rotor-Gene Q, annealing curves were created for samples with primer-to-target ratios, or P:T ratios, of 23:1, 11:1, 5:1, and 1:1. Regardless of P:T ratio, a total DNA (P+T) concentration of 120 nM was maintained. The different P:T ratios represent different stages of PCR in which different amounts of primer have been converted to target by polymerase. Each sample was tested in triplicate, and two-way analysis of variance (ANOVA) was used to determine the significance of the results.

Comparison of D-DNA and L-DNA hybridization in adaptive PCR setting.

An adaptive PCR machine was used to thermally cycle D-DNA and L-DNA at rates of approximately 1 °C/second for heating and 0.5 °C/second for cooling. These rates are much more rapid than those seen in the Rotor-Gene instrument, and indicative of the thermal cycling observed in adaptive PCR. The two chiral forms of DNA were labeled with fluorescently distinct fluorophores so that their respective signals could be differentiated. The adaptive PCR instrument collected fluorescence data as a function of time, rather than temperature, so annealing timepoints were analyzed rather than annealing temperatures. Samples were thermally cycled between 50 and 90 °C, based on readings from an inserted thermocouple (Omega, 5TC-TT-K-36-36). As the samples heated and cooled, fluorescence was measured in 0.67 second intervals for both fluorescent channels. Several different fluorescent labels were tested for both D-DNA and L-DNA, as well as several different P:T ratios. For each set of reaction conditions, three identical samples were analyzed for three heating/cooling cycles each. Fluorescence data was imported into Matlab to plot the derivative with respect to time, and this data was used to calculate the annealing timepoints for both D-DNA and L-DNA.

Effect of L-DNA fluorescent design on PCR efficiency.

A Roche LightCycler 96 was used to perform PCR in a 96-well plate with a heat gradient applied across the plate during the annealing phase of the reaction. The annealing temperatures tested (individual columns of the 96-well plate) were 55.0, 57.6, 60.3, and 62.9 °C. The samples were cycled between the annealing temperatures, which varied, and the melt temperature 95 °C, and held at each temperature for 10 seconds. A total of 50 cycles were performed, and each reaction condition was tested in triplicate. The LinRegPCR software package was used to analyze the amplification curves and determine reaction efficiency for each annealing temperature.

Adaptive PCR was performed using previously described methods (i.e., switching between heating and cooling is based not on temperature, but on the fluorescence of the L-DNA analogs).[109] The L-DNA primer-analogs were labeled with 5' FAM and included in the sample at a concentration equal to that of the

D-DNA primers. Two different designs were used for the complementary quenching strand L-DNA: 3' BHQ-2 with a 0-base offset and with a 10-base offset (**Figure 8**, designs B and D). Adaptive PCR was performed for 40 cycles for each design, and tested in triplicate. PCR reaction efficiency was calculated for each sample using the LinRegPCR software package (available at https://www.medischebiologie.nl/files/). Samples were baseline corrected for fluorescence and then windowed based on the linear portion of the log increase of fluorescence to calculate the efficiency.[111]

2.3 Results and Discussion

L-DNA versus D-DNA annealing analysis.

L-DNA has previously been shown to exhibit identical hybridization properties as natural D-DNA.[61, 66, 102] This key assumption was verified by performing side-by-side annealing analyses on both right- and left-handed DNA with BHQ-2 quenching with no offset (**Figure 8**, design B). The selectivity of sequence binding occurs during the annealing phase of PCR because strands of varying lengths bind at distinct temperatures during cooling, affecting the temperature at which polymerase can efficiently extend primers to create new target copies. Too high of an annealing temperature and primers will not bind; too low and binding will be non-specific. Therefore, we focused primarily on the annealing events. Analysis of the annealing curves for identical D-DNA and L-DNA sequences labeled with Texas Red revealed annealing temperatures of 70.1 ± 0.1 and 70.2 ± 0.1 °C (mean ± 1 standard deviation of three trials), respectively, reinforcing the assumption that D-DNA and L-DNA exhibit identical annealing behavior.

Annealing temperatures of each fluorophore-quencher pair

The annealing temperatures calculated for each of the six fluorophores in each of the four described quenching schemes are shown in **Figure 9**. Only D-DNA was used here; the behavior of L-DNA is assumed to be equal, based on our previous results. In all cases, regardless of the fluorescence design, the presence of fluorescent labels raised the observed annealing temperature compared to that of unmodified DNA

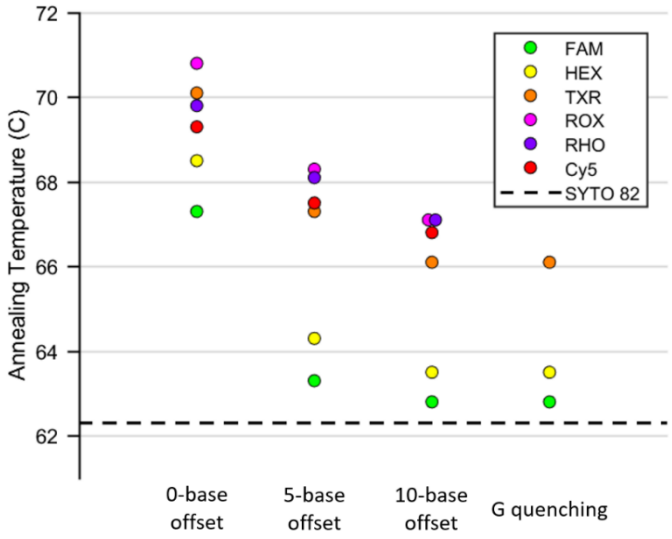

Figure 9. Plot of annealing temperatures for oligos labeled with each fluorophore and quenched by BHQ-2 with 0, 5, and 10-base offsets, as well as quenched by guanine with no offset. The horizontal dashed line depicts the annealing temperature of unmodified DNA measured with SYTO 82 intercalating dye.

measured with SYTO 82 intercalating dye. The quenching efficiency of BHQ-2 (shown in **Table 2**), or the fraction of maximum fluorescent signal which is lost when quenched, was found to be >89% for each fluorophore and each offset distance. The efficiency dropped slightly as the offset distance increased and the effect of contact-mediated quenching decreased, but this difference was not found to be statistically significant ($p > 0.05$).

The observed increase in annealing temperature was largest for designs quenching with BHQ-2 with 0-base offset, where it ranged from 4.0-7.5 °C depending on the fluorophore. Offsetting the BHQ-2 by 5 bases resulted in a smaller increase in annealing temperature for all fluorophores, and a 10-base offset lowered that increase even further. It appears that as the distance between fluorophore and quencher grows and the quenching mechanism shifts from contact-mediated quenching to FRET quenching, the stabilizing effect on the DNA duplex decreases. Guanine quenching showed almost identical annealing temperatures as 10-base offset BHQ-2 quenching, although it only quenched sufficiently to make out an annealing curve for FAM, HEX, and Texas Red. The similarity of results between 10-base offset BHQ-2 quenching and

Table 2. Quenching efficiencies for each fluorophore-quencher pair.

	0-base offset	5-base offset	10-base offset	guanine
FAM	94.1	91.2	89.9	49.0
HEX	96.5	92.6	90.7	57.9
Texas Red	99.3	98.4	98.5	12.2
ROX	98.9	98.5	98.1	12.3
ATTO Rho101	98.3	97.8	97.7	14.1
Cy5	99.6	98.8	97.1	10.4

guanine quenching suggests that the quencher molecule has minimal effect on duplex stability when separated from the fluorophore by 10 bases. Separating the fluorophore and quencher by a distance of 5 bases likely decreases but does not eliminate the contact between the two. The existing protocol for adaptive PCR utilizes quenchers with no offset; these results suggest not only that the fluorescently-labeled L-DNA will anneal earlier than their unlabeled right-handed analogs in the cooling phase of PCR, but also that the difference depends on the fluorophore/quencher pair used.

Effect of primer-template ratio on hybridization behavior.

Based on mathematical modeling of hybridization kinetics, which is described in full in **Appendix 2**, we do not expect a difference in the ratio of primers to templates (P:T ratio) to cause a difference in the observed hybridization behavior between D-DNA and L-DNA, provided the rate of cooling is not too rapid. However, we sought to experimentally prove this hypothesis. We first studied the effect of P:T ratio on annealing temperature by measuring the annealing temperature of samples containing FAM-labeled primers and BHQ-2-labeled targets at P:T ratios of 23:1, 11:1, 5:1, and 1:1. For each ratio, two total concentrations of DNA were examined. The observed annealing temperatures are shown in **Table 3** for each ratio (rows) and total DNA concentration (columns). Two-way ANOVA was employed to determine how much each variable, total concentration and P:T ratio, contributed to the variance. Analysis revealed that the variation

Table 3. Annealing temperatures for different P:T ratios and total concentrations.

P:T ratio	120 nM	240 nM
23:1	66.0 ± 0.06	66.8 ± 0.71
11:1	65.9 ± 0.17	66.9 ± 0.00
5:1	65.9 ± 0.12	66.8 ± 0.10
1:1	66.1 ± 0.10	66.9 ± 0.10

in annealing temperature was primarily dependent on the total concentration of DNA. Doubling the concentration from 120 nM to 240 nM caused an increase in annealing temperature for all oligonucleotides at a significance level $p < 0.001$. Even if all else is equal, L-DNA at a different overall concentration than D-DNA will anneal at a different temperature. To account for this moving forward, D-DNA and L-DNA concentrations are always held equal. The effect of P:T ratio on annealing temperature was not statistically significant ($F=0.44$, $F_{crit}=3.24$), indicating that this ratio does not affect the annealing temperature.

Having now demonstrated that annealing temperature is not affected by the ratio of primers to targets, we next sought to determine whether there was a difference in the observed hybridization of D-DNA and L-DNA in the comparably rapid cooling of adaptive PCR. Thus far, annealing analyses have been performed at the slow rate of 1 °C per minute; adaptive PCR cools 30X as fast. We predict that the hybridization kinetics of D-DNA and L-DNA will be unaffected by P:T ratio *if and only if* the rate of cooling is sufficiently slow. We performed thermal cycling of samples containing D-DNA and L-DNA labeled with different fluorophores, and used fluorescence measurements to determine the annealing time stamp. Since there are no temperature measurements in adaptive PCR, fluorescence was measured as a function of time instead of temperature. A difference in annealing time stamps is therefore indicative of a

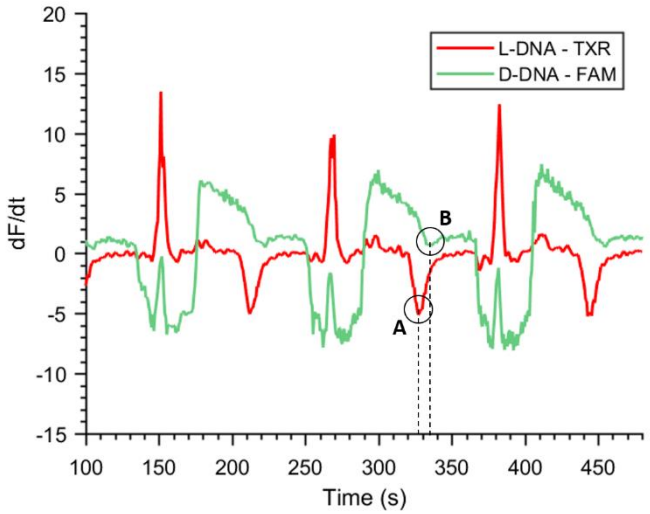

Figure 10. Example dual-waveform for adaptive PCR thermal cycling of D-DNA and L-DNA. Fluorescence is measured as a function of time, and used to generate the dF/dt curve. The local minima of these curves during the cooling phases correspond to the annealing points (circled, A, B). The time in between the two annealing points is the annealing lag. The difference in baseline dF/dt is due to FAM's temperature sensitivity.

difference in hybridization kinetics. **Figure 10** shows an example waveform for FAM-labeled D-DNA and Texas Red-labeled L-DNA, both in the contact-mediated quenching format, with the annealing points circled for the second thermal cycle. Similar to the Rotor-Gene annealing curves, the annealing point is taken as the lowest point of the dF/dt curve, when fluorescence-quenching is increasing most rapidly. We found that FAM exhibited non-zero baseline dF/dt values; this is due to the temperature sensitivity of the fluorophore. A complete evaluation of the temperature sensitivity is shown in **Figure 11**.

There are two possible factors that would cause a difference in annealing time stamps for D-DNA and L-DNA: different fluorescent labels and different P:T ratios. Having already quantified the effects of fluorescent labeling strategy on annealing temperature, this can be accounted for with a simple conversion. The cooling rate of adaptive PCR is known, as is the difference in annealing temperature caused by different fluorescent labeling strategies. The expected difference in annealing time stamps can therefore be predicted with the equation $\Delta T = \frac{dT}{dt} * \Delta t$, where T and t represent temperature and time, respectively. The cooling rate of adaptive PCR was measured to be 0.49 °C, so a difference in annealing temperature of 1 °C would result in a difference of annealing time stamps of 1 / 0.49 = 2.04 seconds. With this in mind, we

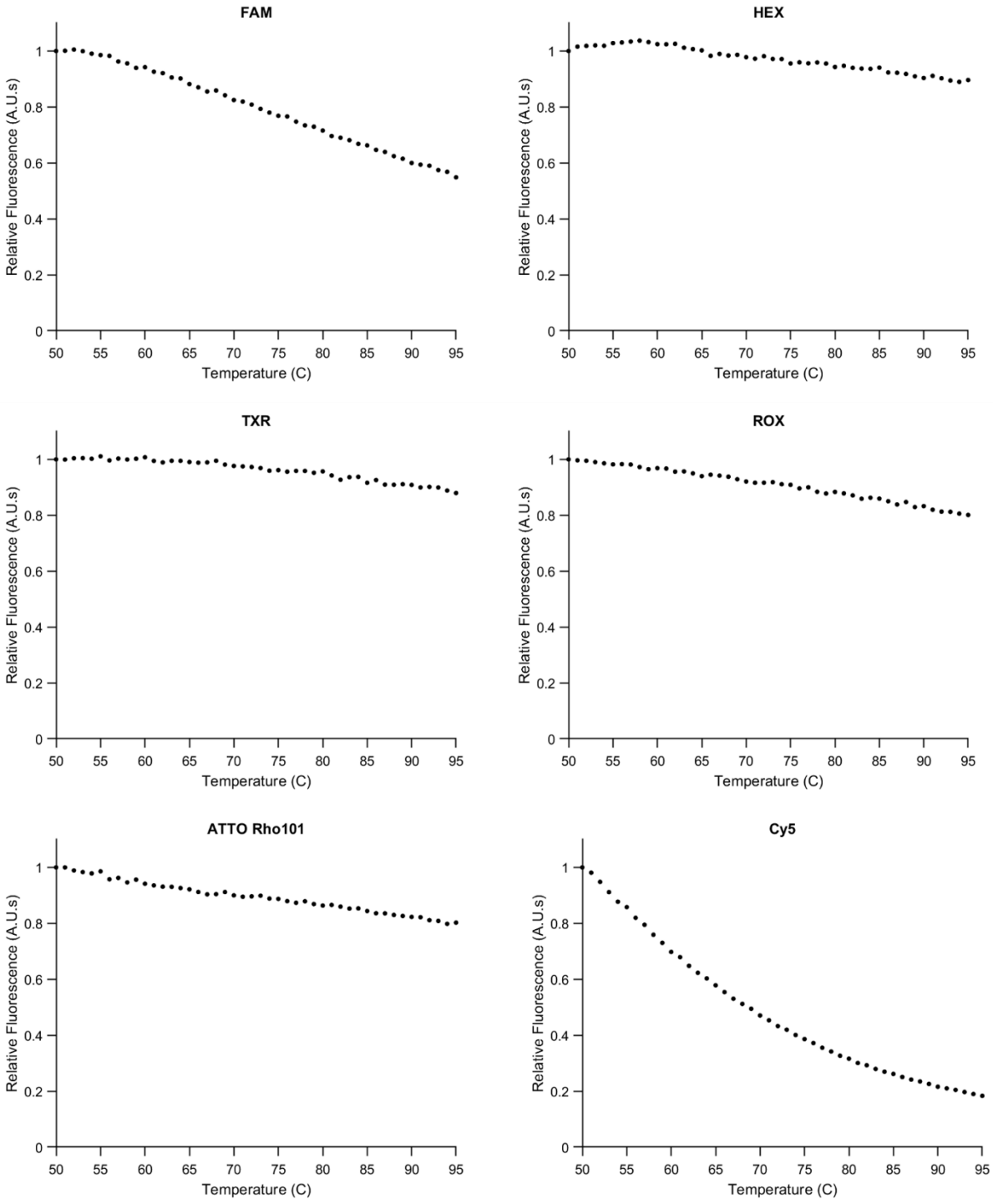

Figure 11. The effect of temperature on observed fluorescence for the six fluorophores used in this study. Fluorescence values are normalized on a scale of 0-1 using their signals at 50 °C. Most fluorophores are thermally stable, with the exceptions of FAM and Cy5.

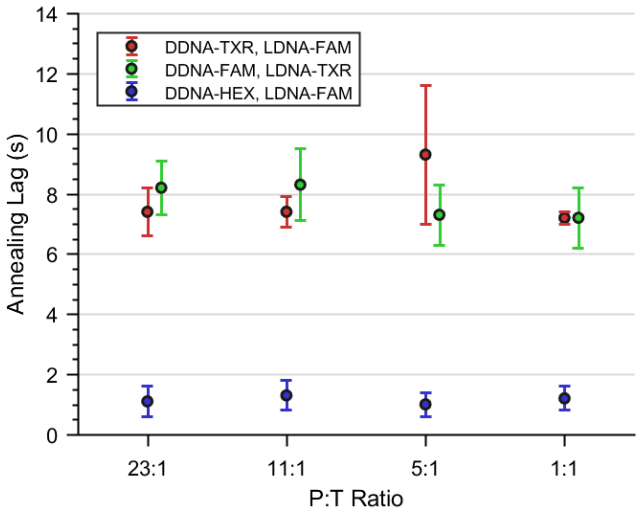

Figure 12. Differences in annealing time stamps during adaptive PCR thermal cycling are observed as one DNA "lagging." Trials with FAM and Texas Red-labeled DNA exhibited a lag time of about 7.7 seconds. This was reduced to 1.1 second when using FAM and HEX-labeled DNA. Error bars depict the mean ± one standard deviation of three replicate trials.

measured the difference in annealing time stamps for D-DNA and L-DNA at different P:T ratios to determine whether there were differences beyond those caused by the different fluorescent labeling strategies.

The observed differences in annealing times are shown in **Figure 12**. The annealing of FAM-labeled DNA lagged behind that of Texas Red-labeled DNA by approximately 7.7 seconds. The measured annealing temperatures of FAM and Texas Red-labeled DNA under these conditions was 65.9 and 69.3 °C, respectively. These values are slightly lower than those in **Figure 9** because the DNA is at a lower concentration. That difference of 3.4 °C corresponds to a predicted lag of 6.9 seconds, which matches quite closely with the observed lag of 7.7 seconds. Moreover, one-way ANOVA confirmed that the P:T ratio had no significant effect on the difference between annealing time stamps. It seems that the difference in annealing times during adaptive PCR can be predicted based entirely on the annealing temperatures of the D-DNA and L-DNA, and is independent of P:T ratio. To test this hypothesis, we replaced Texas Red with HEX. The annealing temperatures of FAM and HEX-labeled DNA under these conditions were found to be only 0.8 °C apart; the difference in annealing times between the two should therefore be much smaller

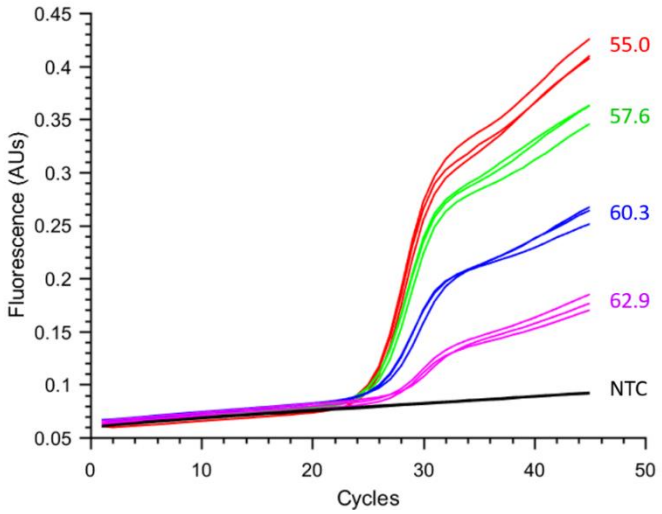

Figure 13. PCR amplification curves for a range of annealing temperatures (listed right). All samples, except those labeled NTC, contained equal amounts of target DNA. The no-target controls (NTC) all overlapped regardless of annealing temperature. Each reaction condition was tested in triplicate, and all three curves are shown.

than when FAM and Texas Red were used. Indeed, the results (**Figure 12**, blue) show that FAM-labeled DNA lagged by 1.2 ± 0.4 seconds on average. Based on these results, we concluded that the cooling rate for our adaptive PCR system is slow enough that the kinetic effects of different P:T ratios are negligible, and the different fluorescent labels are the only factor causing a difference in hybridization behavior between D-DNA and L-DNA.

Effect of annealing temperature on PCR efficiency

The previous results show that L-DNA which is fluorescently labeled exhibits a higher annealing temperature than unlabeled D-DNA. Therefore, during the cooling phase of adaptive PCR, the D-DNA annealing will lag behind the observed annealing of the L-DNA. Assuming the annealing temperature of the D-DNA is the correct temperature switch point, then the actual switch point based on L-DNA fluorescent signal is likely too high. To examine the effect of switching at too high of a temperature, we performed traditional PCR on identical samples using a range of different annealing temperatures. The resulting amplification curves are shown in **Figure 13**; as the annealing temperature increased, PCR efficiency decreased. Efficiency can be estimated based on the slope of the rapidly-increasing portion of

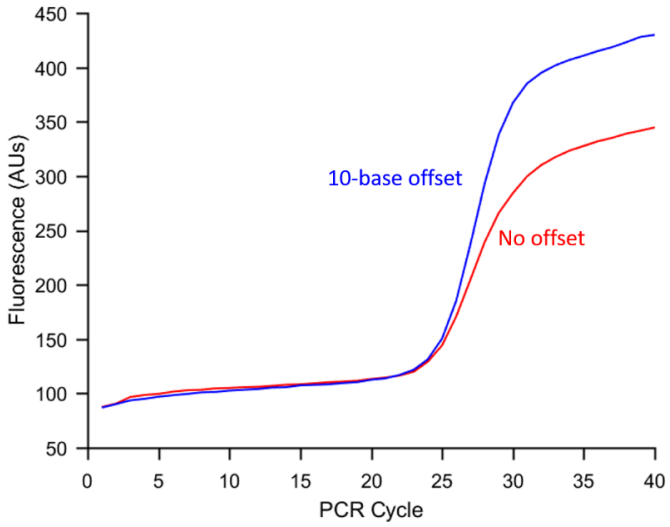

Figure 14. Mean amplification curve (n = 3) for adaptive PCR with 0-base offset FAM quenching (red) and 10-base offset FAM quenching (blue). Separating the fluorophore from the quencher increased amplification efficiency by approximately 15%.

the curve, before it tapers off due to reagent consumption. Based on these results, as well as the conclusion that P:T ratio does not affect hybridization behavior during adaptive PCR, we hypothesize that adaptive PCR efficiency is maximized if the annealing temperatures of identical D-DNA and L-DNA sequences match each other as closely as possible.

To test this hypothesis, we performed adaptive PCR using three different fluorescence designs for the L-DNA. Since the D-DNA in PCR cannot be fluorescently modified, we chose the fluorescence designs which produced the smallest change in annealing temperature (see **Figure 9**): FAM with a 10-base offset from the BHQ-2 and FAM with guanine-quenching. As a comparison, we also used FAM with no offset, as this resulted in an annealing temperature approximately 4 °C higher. We quickly discovered that guanine-quenching is not effective for left-handed guanine (data not shown), so this was not a valid design for the L-DNA. The adaptive PCR amplification curves for the other two designs are shown in **Figure 14**. The mean amplification efficiency for 0-base offset and 10-base offset quenching were 75.0 ± 7.9% and 90.4 ± 9.9%, respectively. As a reference, traditional PCR was also performed using a Rotor-Gene as previously described,[109] and the efficiency was 66.8 ± 19.8%. Statistical analysis using a one-tailed t-test assuming unequal variance showed that the 10-base offset design led to a statistically significant increase in efficiency

compared to the 0-base offset design ($p = 0.04$). The low efficiency of the reaction can be attributed to its original use in single nucleotide polymorphism (SNP) detection, which greatly limits the choice of primer sequences. This makes the reaction an excellent candidate to study the effect of fluorescent labels on amplification efficiency, although we still expect to see the same trends in other more efficient reactions.

2.4 Conclusions

We have shown that nucleic acids which have been covalently modified with fluorescent end-labels do not exhibit the same hybridization characteristics as identical unmodified nucleic acids. Contact-mediated quenching, in which the fluorophore and quencher are in physical contact, caused the largest shift in annealing temperature from that of unmodified DNA. Preventing the interaction between fluorophore and quencher, whether it be by distancing them from each other or by replacing the quencher molecule with a guanine, led to a much smaller effect. FAM showed the smallest shift in annealing temperature out of the six fluorophores tested, making it the ideal choice for matching the behavior of unlabeled DNA. It is worth noting that the extent of this stabilizing effect caused by fluorescent labels is likely sequence-specific; we expect the general trends observed here, however, to remain true regardless of sequence. These findings can be used to guide fluorescent design strategies for oligonucleotides. As an example, we applied this strategy to hybridization-controlled adaptive PCR and were able to significantly increase reaction efficiency by selecting the fluorescence design which minimized the effect on annealing temperature.

Previous work regarding adaptive PCR has demonstrated high-efficiency amplification despite utilizing L-DNA which is quenched with no offset.[66] While this may seem contradictory with the findings presented here, each reaction required its own optimization of the parameters controlling the switch between heating and cooling. In this way, an imperfect L-DNA design was worked around by adjusting the instrument settings. The findings presented here offer guidelines which should eliminate the need to individually optimize each reaction, as done in the past, because the L-DNA hybridization will mirror that of the D-DNA in the reaction. This example highlights the importance of selecting an appropriate fluorescence quenching design for nucleic acid optical signals.

Chapter 3

3. ADDITION OF MIRROR-IMAGE L-DNA ELEMENTS TO DNA AMPLIFICATION CIRCUITS TO DISTINGUISH LEAKAGE FROM TARGET SIGNAL

Adapted from "Addition of mirror-image L-DNA elements to DNA amplification circuits to distinguish leakage from target signal." *Biosensors and Bioelectronics* 188 (2021) with permission from Elsevier.

3.1 Introduction

DNA is emerging as the framework of choice for nanoscale biological computing, due to its low cost, potential for customization, and the predictable nature of Watson-Crick base pairing. Using toehold-mediated strand displacement – a simple reaction in which an input strand triggers the release of a separate output strand – as a building block, DNA nanomachines ranging from logic circuits to molecular motors are at the forefront of biological computing.[112-114] One of the most promising applications of DNA nanomachinery is in signal amplification; a variety of different circuits have been employed to amplify the signal generated by the presence of target nucleic acids.[42, 45, 59, 115] The most successful nucleic acid amplification tests, such as polymerase chain reaction, amplify a target sequence by up to one billion-fold, but require enzymes and thermal cycling to achieve this. DNA circuits circumvent these requirements, relying only upon hybridization events between nucleic acid circuit components. In this way, DNA amplification circuits present a path toward simpler, lower-resource diagnostic tests.

One of the simplest and most researched diagnostic DNA circuits, catalyzed hairpin assembly (CHA) relies on a pair of hairpin structures to amplify a target-induced signal.[41, 42, 116, 117] In this approach, single-stranded DNA molecules with self-complementary regions are designed to auto-hybridize to form a double-stranded "stem" region (H1 and H2 in **Figure 15**). The key to signal amplification lies in the thermodynamic energy stored in these hairpins; H1 and H2 are designed to have complementary regions which are initially blocked via self-hybridization in the stem regions, preventing them from interacting. The

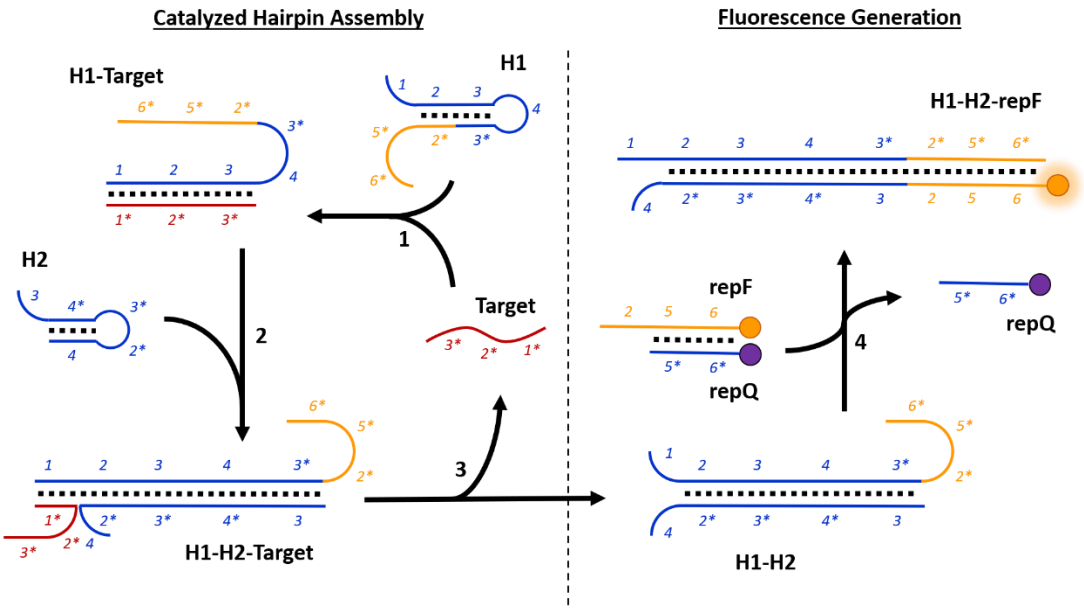

Figure 15. Overview of the catalyzed hairpin assembly reaction mechanism. In dual-chirality CHA, only the D-DNA circuit undergoes this reaction pathway. **1.** The target sequence binds to hairpin H1 at the toehold domain 1, causing a conformational change and revealing the toehold domain 3*. **2.** H2 binds to the H1-target complex, partially displacing the target sequence. **3.** The loosely bound target can detach and bind to other hairpins to initiate further hairpin assembly. **4.** Once opened, the exposed domain 2* in H1 acts as a toehold to bind the strand repF from the fluorescent probe. This separates the fluorophore from the quencher on repQ, causing an increase in fluorescent signal.

presence of a target sequence, however, catalyzes a conformational change in hairpin H1, revealing its previously-blocked domain to initiate binding with hairpin H2. Hairpins H1 and H2 then form a stable complex which is only loosely associated with the target sequence. This loosely bound target is prone to separate from the H1-H2 complex and catalyze additional hairpin interactions.

Although DNA amplification circuits such as CHA offer promising results in diagnostic applications, they are subject to a rising non-specific signal known as leakage.[42] **Figure 16** shows two possible leakage pathways for a CHA circuit, although others are possible as well. Like any chemical reaction, DNA hybridization state is defined by a chemical equilibrium which lies somewhere between completely hybridized and completely unhybridized.[118, 119] Even when double-stranded DNA is hybridized, it can temporarily "breathe," revealing previously-bound bases and allowing for unintended reactions with other components. The exact amount of leakage depends on kinetic properties of the DNA components, as well as reaction conditions such as temperature and ionic concentrations.[120, 121] Additionally, hairpins which

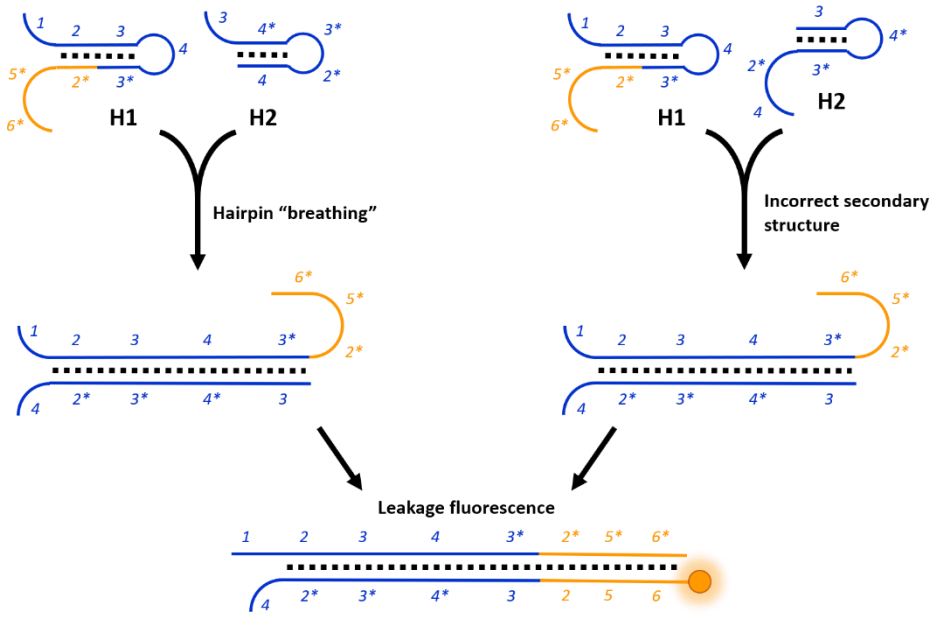

Figure 16. Two possible leakage pathways for the CHA circuit. In dual-chirality CHA, both the D-DNA and the L-DNA circuits undergo these processes. **Left:** The complementary domains of hairpins H1 and H2 are blocked in the stem regions, but the hairpins may briefly reveal these blocked domains while "breathing". **Right:** While less likely, it is also possible for the hairpins to assume forms other than the desired structure, revealing binding domains which would otherwise be blocked. Both of these pathways result in the assembly of H1 and H2, and the generation of leakage signal.

are mis-folded or mis-synthesized may have an incorrect structure which facilitates unintended interaction with other circuit components. Circuit leakage results in a background signal that decreases the signal-to-noise ratio, negatively impacting the limit of detection in diagnostic applications of DNA amplification circuits. In response to these challenges, one approach is to minimize leakage as much as possible. CHA leakage has been reduced by up to two orders of magnitude using techniques such as single-base mismatches, padding binding domains, and ensuring maximum oligonucleotide purity.[46, 47] Leakage-reduction techniques such as these represent the dominant approach thus far to address the challenges posed by circuit leakage. Importantly, however, a completely leakless CHA reaction has yet to be demonstrated using any combination of these methodologies.

A second approach to overcoming the challenges posed by leakage is to use separate but otherwise-identical samples with no added target as no-target controls. Any amplification observed in these controls must therefore be due to leakage, and can be used as a comparator for the signal from target-containing

samples. This approach does not reduce leakage, but instead measures it directly with the assumption that the leakage will remain constant across reactions. Diagnostic applications of CHA have predominantly used this method, preparing buffered samples and adding purified target to create "positive" samples.[122-125] This method requires the performance of additional parallel reactions, increasing the time and reagent requirements. Additionally, not all types of samples can be replicated in the form of a no-target control. If testing for a target sequence in urine samples, for example, a version of that same urine sample without target cannot be fabricated. Similarly, leakage variation resulting from differences in reaction temperature between samples is not accounted for in traditional CHA reactions. An ideal no-target control would exist in the same reaction as the amplification circuit, and thus be exposed to identical reaction conditions. Currently, to the best of our knowledge, this ideal control has not been created in any DNA amplification circuit. With this in mind, we demonstrate here a novel type of dual-chirality CHA circuit which achieves this goal using left-handed DNA to measure leakage in the same reaction.

DNA is a chiral molecule; only the right-handed form (D-DNA) is found in living systems. The first left-handed nucleosides were synthesized in the 1960s,[126] but they have only recently become commercially available due to advances in synthetic methodologies.[62] While there are other conformations of right-handed DNA, such as the Z-form in which the double helix forms a left-handed spiral, these are only different folding structures of the same right-handed nucleosides. Left-handed DNA (L-DNA), on the other hand, comprises left-handed nucleosides with functional groups occupying different locations around the chiral center. Under normal physiological conditions, L-DNA naturally forms a left-handed spiral in the same way that D-DNA naturally forms a right-handed one. L-DNA exhibits identical solubility, hybridization kinetics, and duplex thermal stability compared to D-DNA, but does not hybridize with its right-handed counterpart.[60-62] This has led to the use of L-DNA in microbiology for nuclease-resistant aptamers, universal microarrays, hybridization sensors for PCR, and drug delivery complexes.[61, 127-129] The identical physical properties of L-DNA make it the perfect candidate to measure reaction leakage in DNA circuits such as CHA. An identical circuit composed entirely of mirror-image L-DNA should not, in theory, be triggered by any nucleic acids found in the sample. Therefore, any signal amplification observed in the

L-circuit can be attributed to intrinsic circuit leakage. Additionally, since D-DNA and L-DNA do not cross react, the two circuits can coexist in the same reaction, subjecting them to identical leakage-determining reaction conditions. In this report, we examine the hypothesis that D-DNA and L-DNA circuits can be combined in a single reaction to create a novel dual-chirality CHA circuit in which the L-DNA signal reports leakage and the D-DNA signal reports target-induced amplification plus leakage.

3.2 Materials and Methods

Oligonucleotides.

The oligonucleotide sequences in this work were adapted from a previous publication on CHA by Li *et. al*.[42] These sequences are listed in **Table 4**, with distinct binding domains separated by underscores (e.g., H1 has domains 1, 2, 3, 4, 3*, 2*, 5*, 6*). D-DNA was purchased from Integrated DNA Technologies (Skokie, IL) and purified with standard desalting. All oligonucleotides with fluorescent labels were purified with high performance liquid chromatography (HPLC). Although unlabeled, H1 was PAGE-purified due to its long length of 67 base-pairs. All L-DNA was purchased from Biomers.net (Ulm, Germany) and purified using HPLC. Oligonucleotide stock solutions were diluted to 100 μM in TE buffer, and subsequent aliquots at lower concentrations were stored in TNaK buffer (20 mM Tris, pH 7.5; 140 mM NaCl; 5 mM KCl). Absorbance measurements at 260 nm were taken using a Thermo Scientific NanoDrop 1000. These measurements, along with molar extinction coefficients provided by the manufacturer, were used to calculate the concentration of each DNA aliquot. Agarose gel electrophoresis was performed using 3% agarose solution in 0.5X TBE buffer. The DNA circuit elements were combined and incubated at 37 °C for 2 hours, then loaded into the gel and ran at 75V for 45 minutes.

Fluorescent probe preparation.

The fluorescent probe consists of two complementary oligonucleotides; in keeping with the nomenclature established by Li *et. al*,[42] these are referred to as repF and repQ (illustrated in **Figure 15**).

Table 4. Oligonucleotide sequences used in Chapter 3.

Name	5' mod	3' mod	Sequence (5' – 3')
H1			GTCAGTGA_GCTAGGTT_AGATGTCG_ CCATGTAGA_CGACATCT_AACCTAGC_ CCTTGTCA_TAGAGCAC
H2			AGATGTCG_TCTACACATGG_CGACATCT_ AACCTAGC_CCATGTGTAGA
repF	FAM / HEX		CGA_GTGCTCTA_TGACAAGG_GCTAGGTT
repQ		BHQ-2	C_CCTTGTCA_TAGAGCAC_TCG
target			CGACATCT_AACCTAGC_TCACTGAC
pf84			ACATGGCTATGACGGGTAACG
pf84 transducer			CGACATCT_AACCTAGC_TCACTGAC_ CGTTACCCGTCATAGCCATGT_ GTCAGTGA_GCTA

RepF has a 5' fluorophore and is longer than repQ, resulting in a single-stranded toehold region on its 3' end. RepQ has a 3' quencher which quenches the fluorescence of repF when the two are hybridized. These two oligos were mixed at a repF:repQ molar ratio of 4:5 to ensure complete quenching. Concentrations of fluorescent probe refer to the concentration of repF; 200 nM fluorescent probe indicates a mixture containing 200 nM repF and 250 nM repQ. Fluorescence calibration curves for both the right- and left-handed repF oligos were created by measuring the fluorescence of serial dilutions in a Qiagen Rotor-Gene Q PCR instrument. The gain settings were adjusted such that equal concentrations of FAM-labeled D-DNA repF and HEX-labeled L-DNA repF yielded identical fluorescent intensities. These gain settings were then used for subsequent CHA studies.

Catalyzed hairpin assembly.

Before performing a CHA reaction, the reaction components H1, H2, and fluorescent probe were each individually refolded to ensure proper secondary structures. This was accomplished by heating each reagent to 90 °C and then slowly cooling to room temperature at a rate of approximately 3 °C per minute. Once at room temperature, H1, H2, and the fluorescent probe were mixed at equal ratios and incubated for 30 minutes at room temperature. This was done to allow for mis-folded or mis-synthesized hairpins to interact prior to the start of target-induced amplification [46]. In cases where the transducer hairpin was used, this was also refolded and added to the H1-H2-probe mixture. After 30 minutes, the H1-H2-probe mixture was added to the sample for final reaction concentrations of 200 nM each. The sample was then immediately placed in the Qiagen Rotor-Gene Q, where it was held at a constant 37 °C for amplification. We chose 37 ° as this is the temperature at which this circuit was originally designed to operate.[42] Sample fluorescence was measured once the temperature reached 37 °C, and again every 60 seconds to obtain fluorescence vs time data.

For dual-chirality CHA reactions containing both D-DNA and L-DNA, the hairpins were independently refolded as previously described. Then both the right- and left-handed H1, H2, and probe were combined and incubated for 30 minutes at room temperature. Experiments involving the addition of

urine used pooled urine obtained from twenty disease-negative patients at Vanderbilt University Molecular Infectious Disease Laboratory. An IRB exemption for the use of these samples was granted by the Vanderbilt University Institutional Review Board.

L-DNA circuit performance investigation

A series of experiments were performed to quantitatively compare the D-DNA and L-DNA reaction components. Melt analyses were performed using melt curves made with a Qiagen Rotor-Gene Q. Samples containing 200 nM fluorescent probe in TNaK buffer were raised to 90 °C and allowed to reach thermal equilibrium. The temperature was then decreased to 30 °C at a rate of 0.05 °/s, and fluorescence was read at each whole degree interval. A detailed description of the analysis to calculate the melt temperature can be found in **Appendix 1**. Melt curves for hairpins H1 and H2 were performed with the intercalating dye SYTO 82, since these hairpins were unlabeled. SYTO 82 was chosen because it has been shown to have a minimal effect on the melt temperature of double-stranded oligonucleotides.[110] The labeling efficiency of the fluorescent probe oligonucleotides were estimated by comparing DNA concentration, determined using absorbance at 260 nm, to the fluorescent label concentration, determined using absorbance at a wavelength specific to the label (FAM, HEX, or BHQ-2). The ratio of DNA concentration to label concentration gives an approximation of labeling efficiency.

3.3 Results and Discussion

CHA circuit construction.

The components for the CHA circuit used in this work are adapted from a previous publication describing a simple, modular CHA circuit that utilized a double-stranded fluorescent probe to generate an

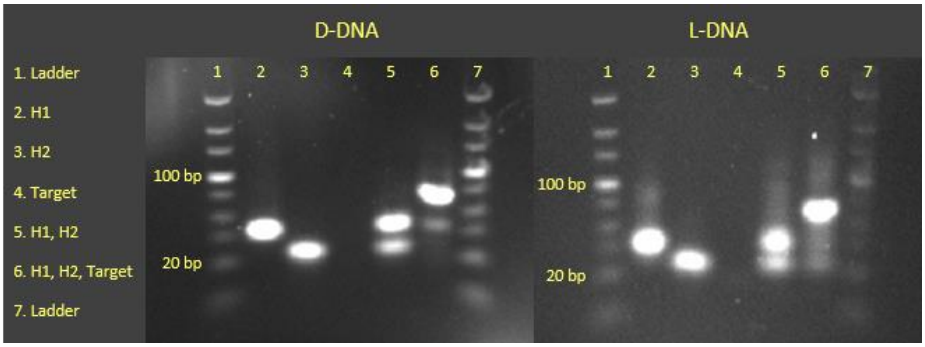

Figure 17. Gel electrophoresis results for both chiral forms of the CHA circuit.

optical signal.[42] The circuit consists of hairpins H1 and H2, as well as the fluorescent probe which generates signal proportional to the number of opened hairpins (shown in **Figure 15**). FAM (ex/em 495/520 nm) and Black Hole Quencher 2 were selected as the fluorophore and quencher molecules, respectively, for the fluorescent probe. We next constructed a mirror-image L-DNA circuit using identical sequences composed of left-handed nucleosides. The only other design change from that of the D-DNA circuit was the choice of a distinct fluorophore; the L-DNA probe was conjugated with HEX (ex/em 535/556 nm) rather than the FAM used for the D-DNA so that the signals from each circuit could be distinguished. These two fluorophores were chosen based on the results of previous studies which found FAM and HEX to have nearly identical effects on duplex stability.[130]

First, gel electrophoresis was performed on both the D-DNA and L-DNA reaction components H1, H2, and target, as well as combinations H1+H2 and H1+H2+target. The resulting gel image is shown in **Figure 17**. Hairpins H1 and H2 each form stable bands, showing that there are no other multi-hairpin complexes being formed. Furthermore, H1 and H2 together do not assemble, instead remaining as two distinct bands (lane 5). The target strand on its own (lane 4) is not visible, likely due to its short length of just 24 bases. When the target is added to H1 and H2, however, assembly of the two hairpins into a larger complex is evident (lane 6). Overall, the D-DNA and L-DNA results look identical, although there are two

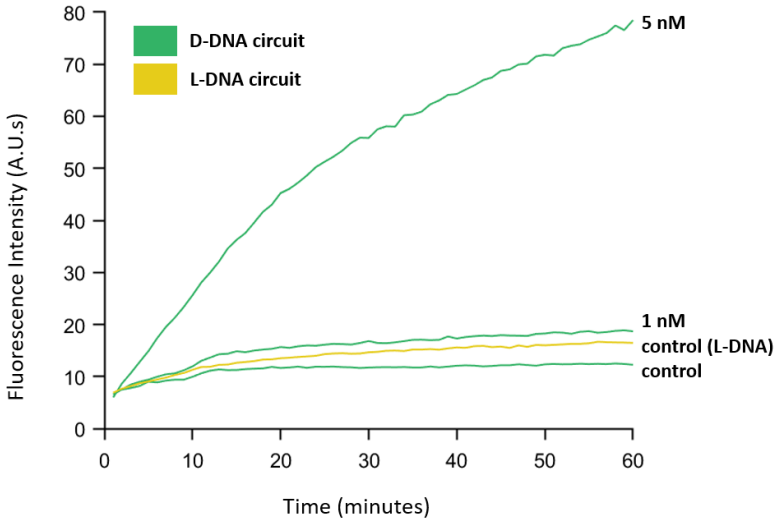

Figure 18. Plot of fluorescence intensity versus time for CHA reactions. D-DNA reactions with 0, 1, and 5 nM target DNA are shown in green (FAM fluorophore), and an L-DNA reaction is shown in yellow (HEX fluorophore).

small differences: The L-DNA bands are streakier, and the L-DNA hairpins do not assemble as completely in the presence of target, leaving un-assembled H1 and H2. Both of these findings could be explained by a lower L-DNA oligo purity, causing less well-defined bands and resulting in incorrect hairpins that don't assemble in the presence of target.

We next introduced the fluorescent probes to monitor amplification in real-time; the reaction components were combined and brought to 37 °C for amplification, as specified by the original authors.[42] As hairpins H1 and H2 assembled, the fluorescent reporter strand repF was separated from the quencher strand repQ (see **Figure 15**) and the fluorescent signal increased. By measuring the fluorescence generated by the probe over time, we observed signal amplification caused by the hairpin chain reaction, shown in **Figure 18**. In order to quantitatively compare results among tests, the change in fluorescence intensity after 60 minutes, hereafter called amplification, was used as a standard measurement. 60 minutes was chosen as the endpoint in order to balance maximizing signal amplification while minimizing total reaction time. The fluorescent signal approaches a plateau as time progresses, and amplification after 60 minutes is minimal (data not shown).

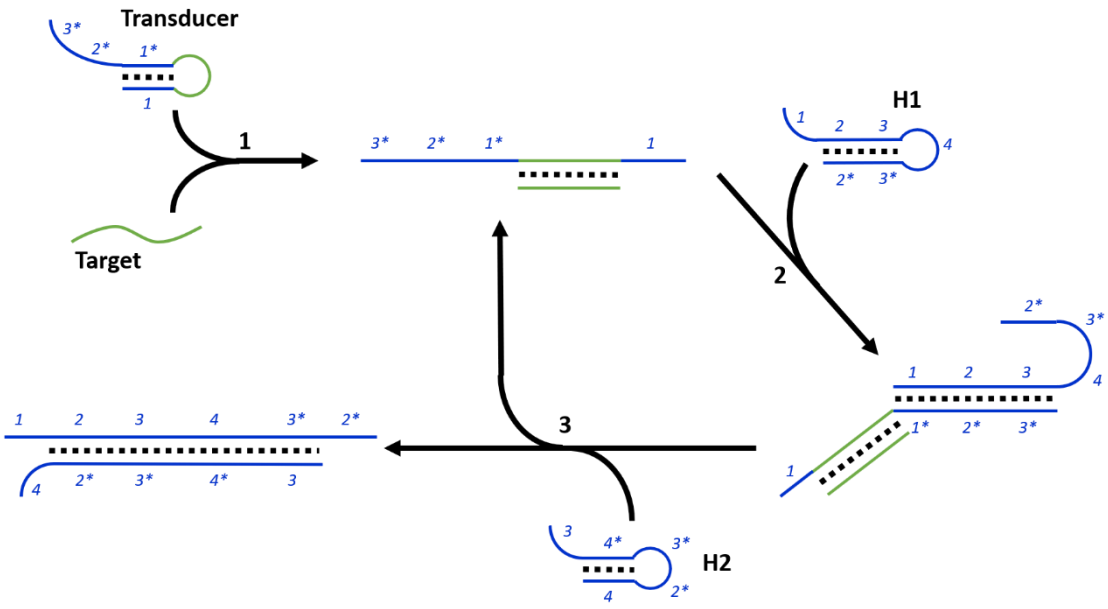

Figure 19. Overview of CHA detection of target via a transducer hairpin. The transducer hairpin changes conformation in the presence of the target (step 1), revealing the CHA circuit catalyst sequence. This, in turn, reveals the toehold for H1 to bind (step 2) and form a transducer-target-H1 complex. The binding of H2 to this complex (step 3) displaces the transducer-target complex.

Adapting a single-chirality CHA circuit to a diagnostic biomarker

The target sequence used in this work is purely synthetic – that is to say, it was not selected from the genome of any known pathogen, but instead designed as a tool for use in optimizing hairpin stability and investigating reaction kinetics. For diagnostic applications searching for a different target sequence, it would be convenient not to require a full redesign of the hairpins to maintain the proper circuit behavior. A simpler alternative to a full redesign is the incorporation of a third hairpin which, in the presence of the new target sequence, changes conformation to reveal the original target sequence for the DNA circuit. This hairpin, hereafter called a transducer hairpin, is complementary to the new target in the loop region, and contains the original catalyst sequence in the stem region. The toehold domain which initiates the opening of hairpin H1 is locked in the stem, so that only once the transducer hairpin has opened can it catalyze the hairpin assembly reaction (shown in **Figure 19**).

To evaluate the feasibility of the transducer hairpin concept, we selected as a new target the pf84 sequence from an established PCR protocol for detection of *Plasmodium falciparum* parasites.[109]

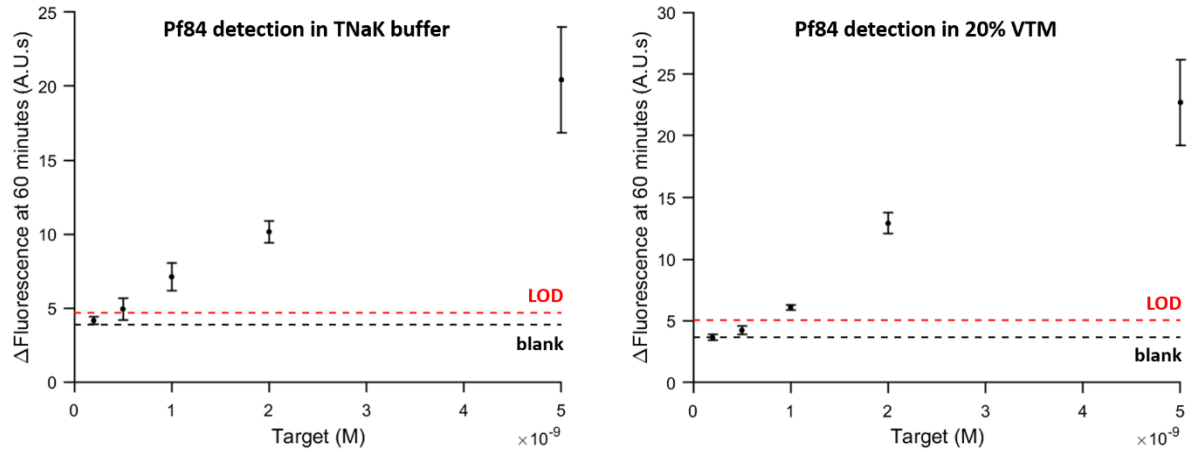

Figure 20. CHA limit of detection studies for detection of pf84 using the transducer hairpin. Tests were performed both in TNaK buffer (left) and in viral transport media at a final concentration of 20% by volume (right). The average amplification for no-target controls is depicted as a dashed black line, and the limit of detection threshold as a red dashed line. Error bars represent the mean ± one standard deviation of three replicate trials.

Importantly, any DNA sequence of approximately the same length could be used here; we chose the pf84 sequence as an analog for any biological target of interest. We next designed the transducer hairpin to contain the pf84 reverse complement in the loop region, and the original catalyst sequence (1* 2* 3* in **Figure 15**) in the stem. The number of bases forming the double-stranded stem was fewer than the number of bases which bind the target, ensuring the conformational change in the transducer is energetically favorable in the presence of pf84 target. The online tool Mfold was used to predict the secondary structures of theoretical hairpin designs; using this we ensured that the desired structure was energetically favorable.

We evaluated the performance of the transducer hairpin by performing CHA (using the D-DNA circuit) with varying amounts of pf84 spiked into solution. The results, shown in **Figure 20**, show that the transducer hairpin is successful in triggering CHA amplification proportional to the amount of pf84 in solution. An approximate limit of detection was obtained by setting a threshold equal to $\mu_0 + 3\sigma_0$, where μ_0 and σ_0 are the mean and standard deviation of the no-target controls, respectively. These tests were then repeated in 20% by volume viral transport media (VTM), a common storage solution for oral or nasal patient samples. The performance of the transducer circuit was very similar in VTM (**Figure 20**, right), with a limit of detection of approximately 0.75 nM for both sample types.

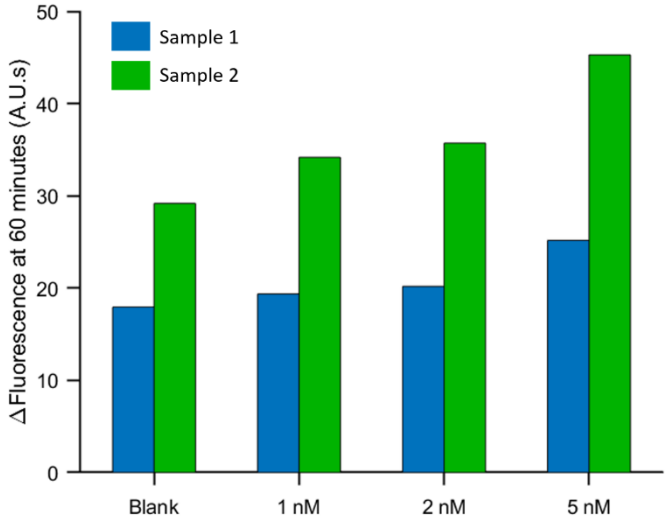

Figure 21. CHA amplification values for pf84 detection in samples containing 20% saliva by volume.

We next investigated the performance of the circuit in detecting pf84 target in a biological medium. Two separate saliva samples were collected several hours apart, and used immediately after collection to prepare CHA samples with 20% saliva by volume. The results in **Figure 21** show that amplification increased along with increasing target concentration, but the signal difference between samples is large. For example, the no-target control amplification in sample 2 is greater than the 5 nM target amplification in sample 1. To interpret these amplification values, the no-target controls are required as a reference. In most diagnostic settings, it is impossible to fabricate this identical no-target control. This highlights the need for a built-in no-target control, which we aim to achieve with a parallel L-DNA circuit in the same reaction.

Combining D-DNA and L-DNA circuits.

The validity of dual-chirality is based on three assumptions: **1)** D-DNA amplification is unaffected by the presence of L-DNA, **2)** L-DNA amplification is unaffected by the presence of D-DNA, and **3)** D-DNA and L-DNA circuit leakages are equal. The existing literature on L-DNA suggests that conditions 1 and 2 should be true, but we designed a simple experiment to confirm this. Both DNA circuits were tested in separate reactions using samples containing 2 nM target D-DNA (**Figure 22**, left bars). The same test

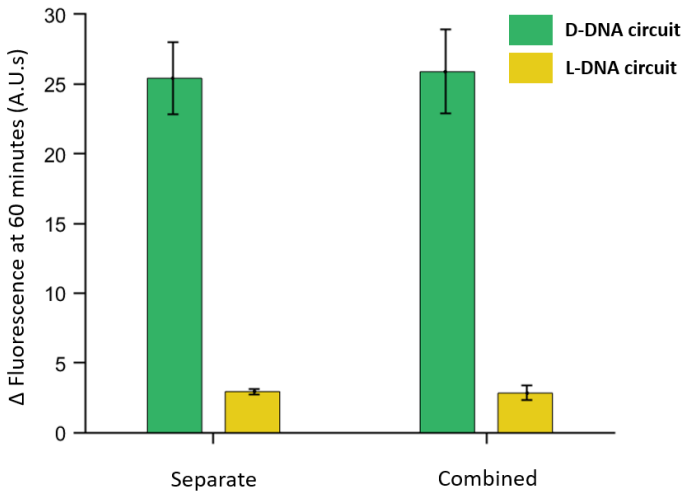

Figure 22. CHA amplification values for D-DNA and L-DNA circuits, both in separate reactions (left) and combined in one reaction (right). D-DNA target was included at 2 nM. Data bars and error bars depict the mean ± one standard deviation for three replicate trials.

was then performed with both circuits together in one reaction (**Figure 22**, right bars). The different fluorophores used in the two circuits allowed for their respective signals to be distinguished. For both circuits, the observed amplification values were not significantly different whether they were in separate reactions or combined into one, based on two-tailed t-tests ($P>>0.05$ for both D-DNA and L-DNA). In other words, both DNA circuits in the dual-chirality CHA reaction behave independently of one another, satisfying the first and second assumptions laid out above.

Matching circuit leakages.

The third underlying assumption for a dual-chirality CHA design is that the leakages of both circuits must match. When the concentrations of D-DNA and L-DNA components were equal, the leakage of the L-DNA circuit was slightly greater than that of the D-DNA circuit (**Figure 18**, compare 'control' and 'control L'). We first examined whether there were differences in the duplex stability of the circuit elements for the right-handed versus left-handed circuits. Melt curves were created by heating the reagents to 90 °C, slowly cooling to room temperature while monitoring fluorescence, and plotting the derivative with respect to time of the fluorescent signal. The results, shown in **Figure 23**, suggest that the thermodynamic

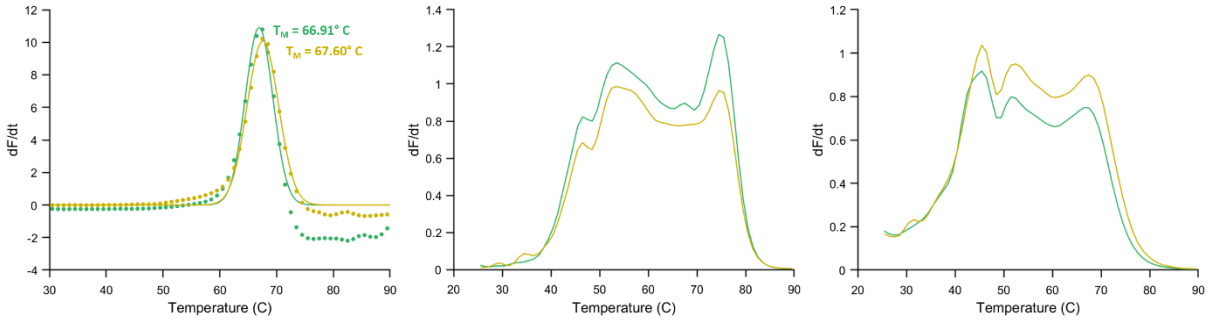

Figure 23. Melt curves for the fluorescent probe (left), hairpin H1 (center), and hairpin H2 (right). Data for D-DNA and L-DNA elements is shown in green and yellow, respectively.

properties of the different chiral forms are extremely similar, and likely not the cause of the observed difference in leakage. The melt temperatures of the fluorescent probes were within 0.6 °C of each other, and the hybridization behavior of the hairpins appear virtually identical.

We next investigated whether there were differences in the fluorescent properties of the probes for the two CHA circuits. The fluorescent signal response of repF was measured for both the FAM-labeled D-DNA strand and the HEX-labeled L-DNA strand. **Figure 24** shows the results; the two versions of repF with their respective fluorophore labels exhibit nearly identical signal responses to varying concentration. Now confident that the fluorescence generated by the fluorophores of our probes was identical, we examined the quenching efficiency of the repQ strands. Keeping the amount of repF constant throughout, repF and repQ were combined at different molar ratios and the resulting fluorescent signals were measured for both the D-DNA and L-DNA probes. As shown in **Figure 24**, as the amount of repQ increases, the fluorescent signal from repF becomes more and more quenched, and fluorescence decreases. The quenching efficiency of repQ was not significantly different between chiral forms (two-tailed t-test, α=0.05). These results assure us that the observed difference in leakage rates between the two circuits is not due to differences in the fluorescent DNA end-labels.

Having now investigated both the thermodynamic and fluorescent properties of our CHA circuit elements, and having found no explanation for the difference in circuit leakage between D-DNA and L-DNA, we formed a new hypothesis. The chemical methods of synthesizing and purifying L-nucleosides are quite different from those for D-nucleosides,[62, 131, 132] and we hypothesized that these differences result in a

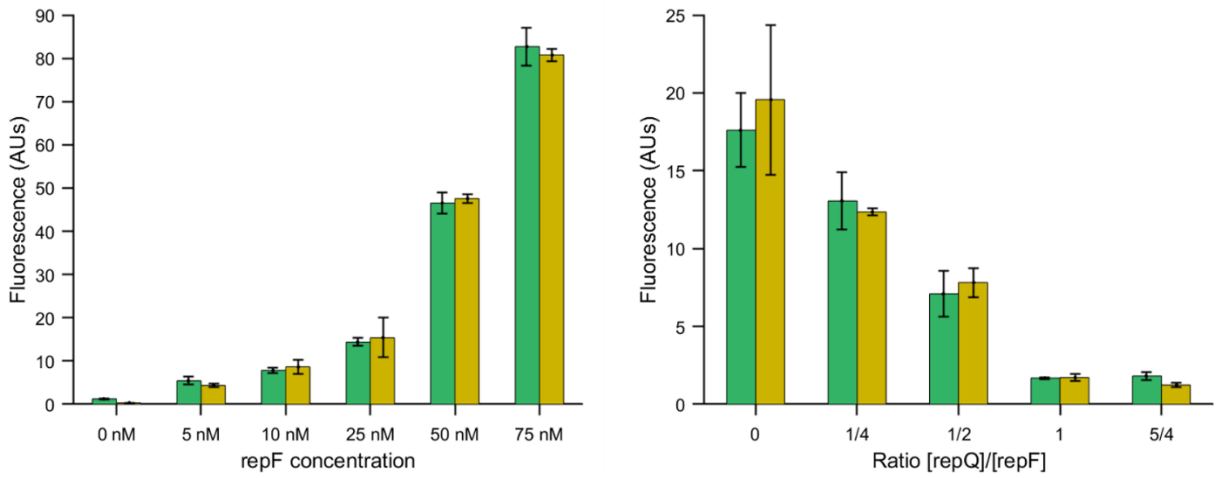

Figure 24. Left: fluorescent signal versus repF concentration for FAM-labeled D-DNA (green) and HEX-labeled L-DNA (yellow). Right: fluorescent signal versus repQ:repF ratio. Data bars and error bars depict the mean ± one standard deviation for three replicate trials.

final L-DNA product with a different purity than that of D-DNA. Our gel electrophoresis results shown in **Figure 17** also suggest that the L-DNA purity may be sub-optimal. This is consistent with a previous report that found an L-DNA CHA circuit does not perform the same as an identical D-DNA circuit; those authors also attributed the difference in performance to unequal purities between the two forms arising from the different synthesis methodologies.[133] Since matching the circuit leakages is a condition that we must satisfy, we next set out to decrease the L-DNA leakage to a level matching that of the D-DNA circuit.

While there are many factors affecting circuit leakage, such as salt concentrations, temperature, and more, changing any of these would affect both circuits since they are contained in the same reaction and subject to the same reaction conditions. Therefore, we sought to match the two circuit leakages by changing the concentration of L-DNA hairpins. Maintaining the 1:1 hairpin ratio of the D-DNA circuit, decreasing amounts of hairpins were used to observe L-DNA leakage. These results are shown in **Figure 25**, with a dashed line showing the D-DNA leakage as a comparator. The L-DNA leakage using 100 nM hairpins was not significantly different than that of the D-DNA circuit with 200 nM hairpins, based on a two-tailed t-test ($P>>0.05$). To ensure that the leakages of the two circuits remain equal, these hairpin concentrations (100 nM L-DNA hairpins, 200 nM D-DNA hairpins, and 200 nM both fluorescent probes) were used for all subsequent CHA experiments.

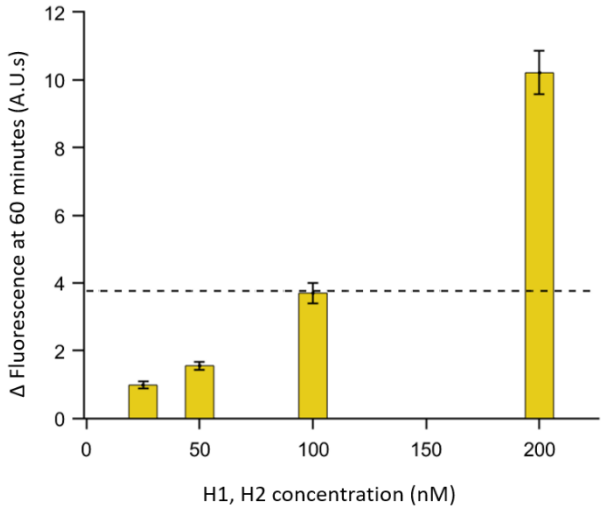

Figure 25. L-DNA circuit leakage versus concentration of hairpins H1 and H2. The level of D-DNA leakage is depicted as a dashed line for reference. Probe concentration = 200 nM, data bars and error bars depict the mean ± one standard deviation for three replicate trials.

Dual-chirality CHA limit of detection.

Now that the three assumptions of dual-chirality CHA have been validated, we sought to evaluate whether the addition of the L-DNA circuit affected the limit of detection. Dual-chirality CHA was performed using target DNA concentrations ranging from 50 pM to 5 nM, including no-target controls. The amplification results are shown in full in **Table 5**. We first analyzed the data as if this were traditional CHA without any L-DNA signal. The commonly employed formula $\mu_0 + 3\sigma_0$ was used to calculate a limit of detection,[134, 135] where μ_0 and σ_0 are the mean and standard deviation of the parallel no-target control amplification values, respectively. Using the D-DNA amplification values for the no-target controls, this yielded a limit of detection fluorescence value of 3.83 arbitrary units. Based on that value, two out of six 100 pM samples and one out of six 50 pM samples were correctly identified, as well as all higher concentration samples. We next converted this limit of detection to a target DNA concentration. A linear line was fit to the amplification vs target concentration data using linear regression; the intersection of this line with the limit of detection fluorescence value (3.83) yielded a limit of detection of approximately 92 pM.

Table 5. Amplification values for dual-chirality CHA limit of detection studies.

		Amplification Values (A.U.s)					
Target Concentration		1	2	3	4	5	6
0	D-DNA	3.26	2.74	3.33	3.10	2.68	3.08
	L-DNA	3.04	3.08	2.98	3.17	2.92	2.93
50 pM	D-DNA	3.79	3.66	3.53	3.76	3.68	3.90
	L-DNA	3.27	3.76	3.21	3.08	2.99	2.96
100 pM	D-DNA	3.77	3.95	3.74	3.96	3.38	3.63
	L-DNA	3.20	2.99	3.06	3.01	2.84	2.98
500 pM	D-DNA	6.72	7.00	7.04	6.72	6.39	6.21
	L-DNA	3.06	3.01	3.32	3.31	2.79	2.68
1 nM	D-DNA	10.2	11.0	11.0	11.4	11.6	13.8
	L-DNA	3.04	3.09	3.07	3.22	2.96	2.55
5 nM	D-DNA	40.6	42.3	41.5	43.9	43.4	43.1
	L-DNA	3.68	2.79	2.77	2.96	2.85	2.76

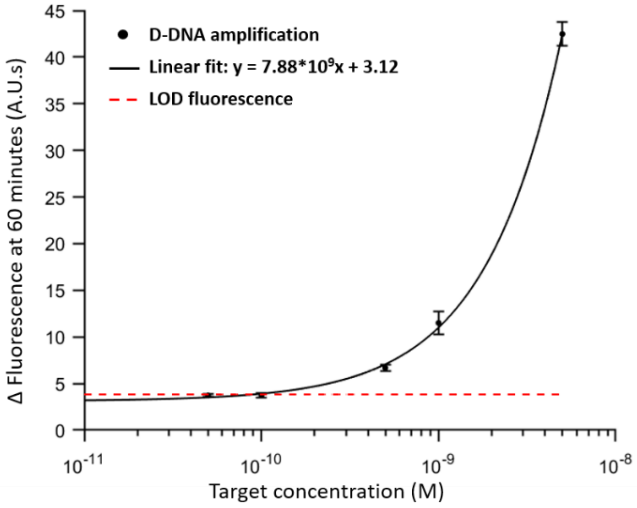

Figure 26. Semi-log plot of D-DNA amplification values from dual-chirality CHA limit of detection studies, as well as a linear line-of-best-fit (curved due to logarithmic x-axis). L-DNA amplification values were used to calculate the limit of detection fluorescence value, depicted as a dashed red line.

We then re-analyzed the data from **Table 5**, this time using the L-DNA data to determine a limit of detection. This method of analysis is unique to dual-chirality CHA; it utilizes both D-DNA and L-DNA signals and does not require the preparation of any no-target control samples. Once again, the formula $\mu_0 + 3\sigma_0$ was used, but this time μ_0 and σ_0 were the mean and standard deviation of the L-DNA amplifications. Using this method, a limit of detection fluorescence value of 3.76 arbitrary units was calculated, which allowed for accurate detection of three out of six 100 pM samples and three out of six 50 pM samples, as well as all higher concentrations. Using the same linear fitting technique as before (shown in **Figure 26**), a target concentration of 81 pM was calculated as the limit of detection for the dual-chirality CHA circuit.

Dual-chirality CHA performance in varying reaction conditions.

Thus far, we have demonstrated successful dual-chirality CHA in simple samples with nothing but buffer and the DNA circuit components. Diagnostic applications of DNA circuits involve using patient samples, and factors such as background DNA, salt concentration, and the presence of biological proteins may cause variable leakage rates. This principle was demonstrated when detecting pf84 in saliva samples. To evaluate the robustness of dual-chirality CHA for diagnostic applications, we performed a series of tests

using a panel of different sample types. Specifically, we sought to demonstrate that the L-DNA circuit accurately matches the leakage of the D-DNA circuit, even in samples with significantly different leakage rates. The panel of samples was designed to represent different leakage-affecting factors which may be found in biological samples. The first sample type contained single-stranded salmon sperm DNA (Sigma-Aldrich, prod #7656) at a concentration of 10 ng/µL. This presents a diverse assortment of random non-target binding domains which may interact with the DNA circuit components. The second sample type included bovine serum albumin at a concentration of 20 µg/µL, to represent sample protein interference. Another sample type included magnesium chloride at 100 mM, due to its well-known interactions with both the DNA backbone and nucleotide functional groups.[136-138] One set of samples were run at a constant temperature of 47 °C, ten degrees higher than usual. Finally, we tested samples containing pooled urine at a concentration of 20% by volume.

The results for each of these sample types are shown in **Figure 27**, including the buffer-only samples as a comparison. For each sample type, dual-chirality CHA was performed on samples with and without target DNA. A target DNA concentration of 2 nM was chosen to show a clear difference between target-positive and target-negative sample signals. The D-DNA and L-DNA signals from samples with target DNA are shown in solid green and yellow, respectively. The signals from the samples without target are shown with white diagonal stripes. Regardless of whether the leakage increased ($MgCl_2$, 47 °C), decreased (BSA), or stayed the same (ssDNA), the L-DNA amplification matched the D-DNA leakage (two-tailed t-test, $P>>0.05$). The one exception to this was with raw urine samples, which caused much higher D-DNA leakage than the observed L-DNA amplification. We hypothesized that this is due to nuclease activity present in urine, which we and others have previously reported,[85] that preferentially degrades right-handed nucleic acids and does not degrade L-DNA. In fact, L-DNA has recently been used specifically to develop a nuclease-resistant CHA circuit.[133] To test this theory, we heated the urine to 75 °C for ten minutes prior to use to deactivate the nucleases. Dual-chirality CHA with this heat-treated urine

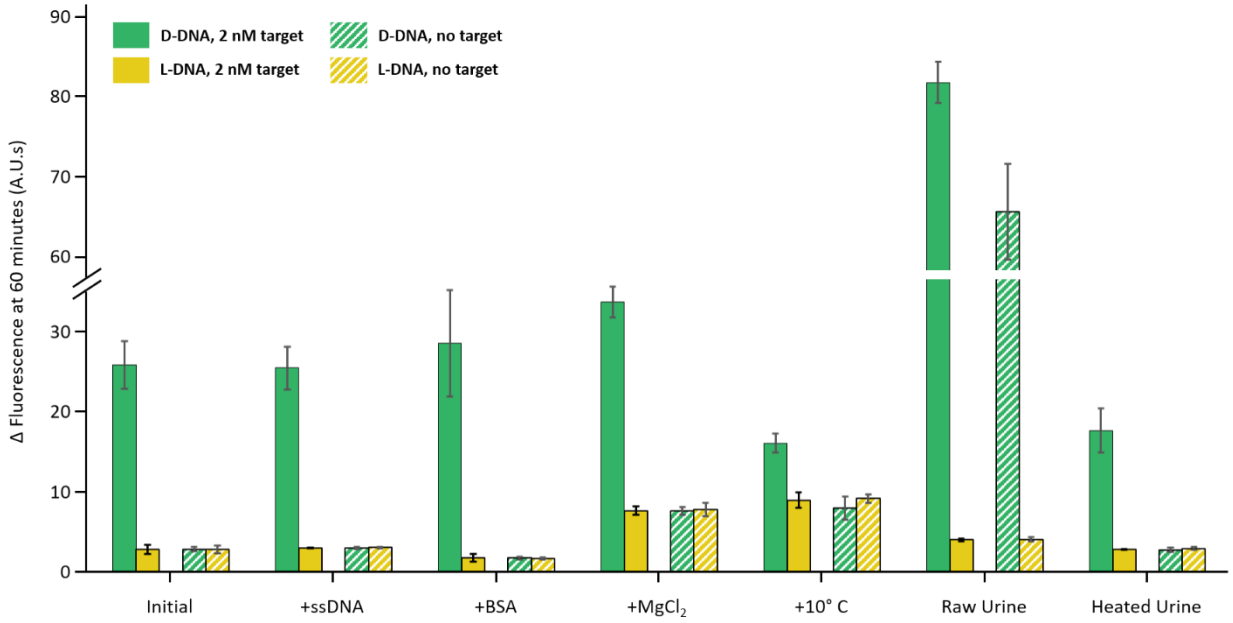

Figure 27. Dual-chirality CHA results for samples with different additives. TNaK buffer was used for the initial reaction conditions. Additives include, from left to right: none (initial conditions), 10 ng/µL salmon sperm ssDNA, 20 g/L bovine serum albumin, 100 mM $MgCl_2$, +10 degrees reaction temperature (47 °C), 20% raw urine, and 20% heat-treated urine. D-DNA and L-DNA signals for samples containing 2 nM target DNA are shown in solid green and yellow, respectively. D-DNA and L-DNA signals for identical no-target controls are shown with white diagonal hashes. Error bars depict the mean value ± one standard deviation for three replicate trials.

showed L-DNA amplification which once again perfectly matched the D-DNA leakage. These results show that L-DNA is an accurate measure of D-DNA circuit leakage across a wide range of sample conditions.

3.4 Conclusions

This work highlights the utility of L-DNA as a leakage control in DNA circuits and lays the foundation for future innovations in dual-chirality circuits. The identical physical properties of L-DNA make it uniquely well-positioned to act as a sentinel of D-DNA circuit behavior. One important caveat, and the major drawback of this work, is that the current synthesis methods for L-DNA result in end-products with different purities than that of otherwise-identical D-DNA sequences. We have circumvented this issue by altering the concentration of L-DNA, but this is neither elegant nor convenient for future applications. Future work should further explore whether a similar problem presents in other types of DNA circuits, and

methods to produce L-DNA hairpins which exhibit truly identical behavior as their mirror-image counterparts.

We have demonstrated a successful application of the dual-chirality design principle for a catalyzed hairpin assembly reaction, where the signal amplification arising from leakage can be distinguished from that of target-induced amplification. Although this particular DNA circuit is not sensitive enough to detect most clinically relevant levels of pathogenic nucleic acids, that shortcoming can be attributed to the intrinsic capabilities of the chosen CHA circuit, rather than the addition of L-DNA circuit elements. In fact, we found dual-chirality CHA to have a comparable, if not slightly improved, limit of detection compared to the same single-chirality CHA circuit. The dual-chirality approach is not unique to catalyzed hairpin assembly circuits, and as newer non-enzymatic DNA circuit designs are developed with higher sensitivity, implementing the dual-chirality design in these circuits will provide a means to further reduce false positives in more clinically relevant target-detection applications.

Chapter 4

4. DEVELOPMENT OF AN AUTOMATED, NON-ENZYMATIC NUCLEIC ACID AMPLIFICATION TEST

This work is adapted from a manuscript which has been submitted and is currently under review at *Micromachines*, under the title "Development of an automated, non-enzymatic nucleic acid amplification test."

4.1 Introduction

Nucleic acids are among the most important biomarkers of disease, and a large variety of diagnostic nucleic acid tests (NATs) have been developed to detect their presence in diagnostic settings, including polymerase chain reaction (PCR), loop-mediated isothermal amplification (LAMP), rolling circle amplification, and others.[30-33] Although very powerful, these tests rely on the use of enzymes, which poses several challenges for use at the point-of-care or in low-resource settings. For example, enzymes are typically the most expensive reagent in a NAT, and they require robust low-temperature storage conditions and labor-intensive sample preparation methods to achieve high sensitivity.[1, 37, 38]

In response to these challenges, non-enzymatic NATs have been developed which amplify a target-induced signal using only thermodynamically-driven DNA hybridization reactions. Examples include hybridization chain reaction, entropy-driven catalysis, and catalyzed hairpin assembly.[48, 116, 139, 140] These tests overcome the obstacles posed by enzymes, but typically have sub-optimal sensitivity due to their poor amplification. There have been several interesting demonstrations of non-enzymatic NATs that achieve increased sensitivity via exponential growth, including cascaded catalyzed hairpin assembly,[46] branched or hyperbranched hybridization chain reaction,[49, 50] and dendritic amplification,[51] but perhaps the most promising is the recent demonstration of a dumbbell DNA amplification scheme.[1] Each DNA dumbbell, shown in **Figure 28**, has four binding domains which bind the opposite dumbbell. The original authors

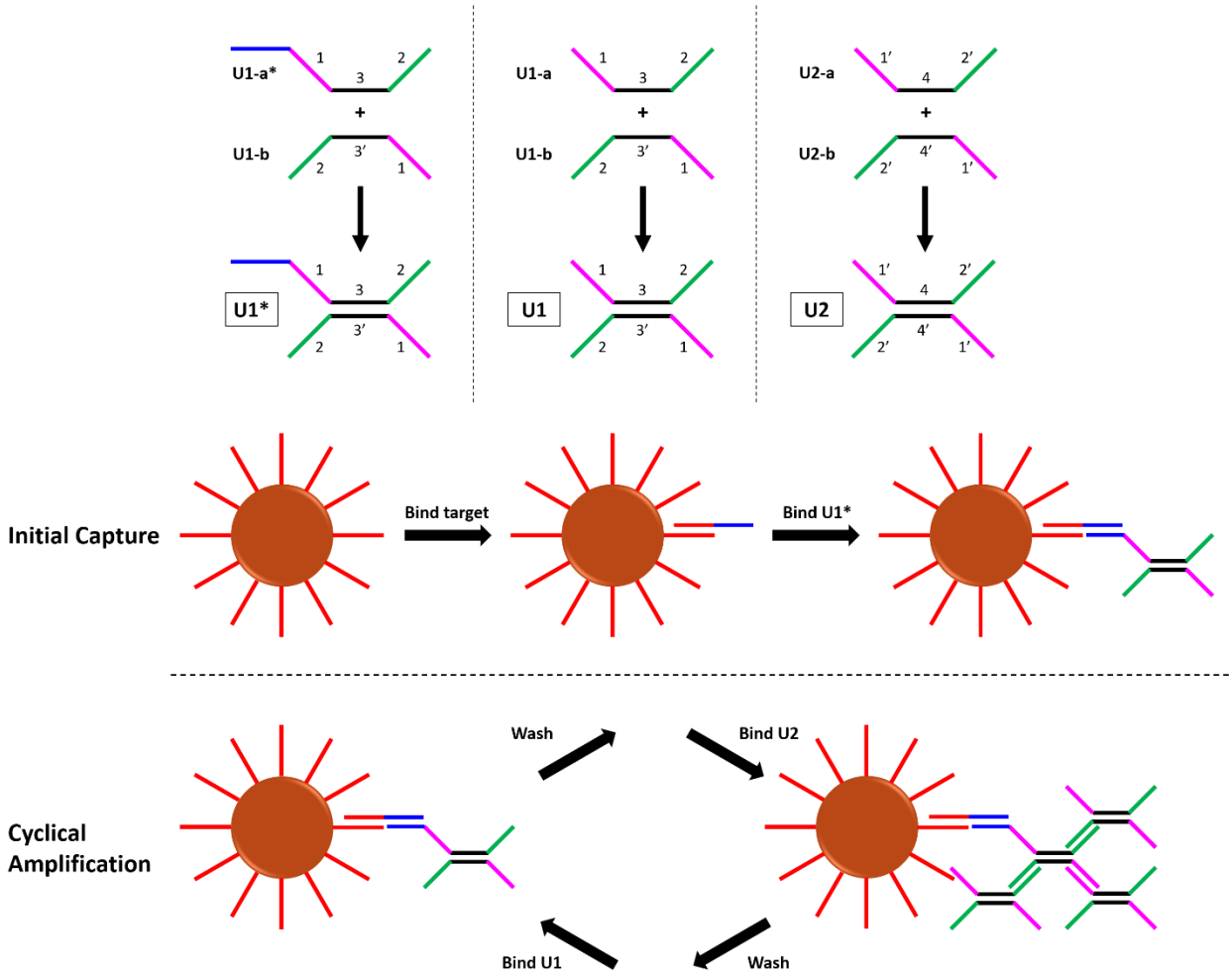

Figure 28. Overview of the dumbbell amplification assay. **Top:** The DNA dumbbells used in this study. Complementary binding domains are denoted as 1, 1' [1]. **Bottom:** Binding steps in the dumbbell amplification assay. After binding target and U1*, the beads cycle between incubations of U1 and U2, with intermediate wash steps.

performed the amplification assay by capturing target DNA on magnetic beads and sequentially incubating the beads with U1, then U2, then U1, and so on. This process is outlined in **Figure 28**. Over the course of 35 dumbbell incubations, a limit of detection of 5 copies/reaction was reported; this far surpasses limits of detection typical of other non-enzymatic NATs.

A serious drawback of this work which was not discussed is the amount of time, labor, and reagents required. The two dumbbells cannot be combined in solution, or they will bind to one another, rather than accumulate on the beads. Instead, they must be added to the beads one at a time, with wash steps in between each incubation. To perform 35 successive dumbbell incubations, as well as the initial target capture step,

approximately 18 hours were required. Over the course of those 18 hours, several pipetting steps were required every 30 minutes, each one a new opportunity for human error. These challenges are exacerbated by the lack of an internal negative control; a second parallel reaction was required to measure non-specific amplification, doubling the total amount of labor, time, and reagents required. It is hard to imagine a laboratory technician who would agree to perform this test on a regular basis, and even harder to imagine one who would do so without errors or variations in technique. If the difficulties of performing this assay can be alleviated, it would have all the qualities of a powerful NAT appropriate for use in low-resource settings.

Previous works have pioneered the use of pre-arrayed reaction cassettes as a simplified and effective method of magnetic sample processing.[67, 68, 86] In this approach, different solutions are loaded into microfluidic tubing and separated by air gaps. The surface tension of these solutions maintains the integrity of the air gaps, and sealing the ends of the tubing immobilizes the contents. Magnetic beads are then transported through the different solutions via movement of an external magnet. Inspired by these methods, we designed an automated reaction processor to perform the dumbbell amplification assay without the need for repeated human pipetting steps. After the initial target capture step, the magnetic beads are loaded into a reaction cassette along with each dumbbell, and automatic movement of the tubing relative to a stationary magnetic field performs all the steps previously performed manually. Fluorescent labels on the dumbbells create a real-time optical readout that can be measured throughout the reaction.

To eliminate the need for a second control reaction, left-handed dumbbells with their own distinct fluorescent labels are included as a built-in negative control. Left-handed DNA (L-DNA) is the chiral enantiomer of right-handed DNA (D-DNA). Although only D-DNA is found in nature, advancements in chemical synthesis techniques have enabled the commercial production of synthetic L-DNA. L-DNA is identical in chemical composition, and exhibits identical solubility, thermodynamic properties, and binding behavior as its right-handed counterpart.[60-62] Having previously demonstrated the utility of L-DNA as a built-in control for non-enzymatic DNA circuits,[140] we use them here as a measure of non-specific amplification in the dumbbell amplification assay.

4.2 Materials and Methods

Oligonucleotides.

All D-DNA sequences were purchased from Integrated DNA Technologies (Skokie, IL), and all L-DNA sequences from Biomers.net (Ulm, Germany). Dumbbells were modified with 5' FAM for D-DNA, and 5' Texas Red for L-DNA. Each fluorescently-labeled oligonucleotide was HPLC-purified. A complete list of sequences is given in **Table 6**, with distinct binding domains separated by underscores. Oligonucleotides were suspended in TE buffer at a concentration of 100 μM and stored at -20 °C for long-term storage. For short-term use, subsequent aliquots were created at 4 μM each in 2X SSC buffer. There were stored at 4 °C.

The dumbbell sequences were adapted from a previous work by Xu et. al (first 7 sequences in **Table 6**).[1] Sequences original to this work (last 5 sequences in **Table 6**) are those designed to detect *S. mansoni* DNA, as well as 'U1-a* tag' and 'U1* removal', which were designed for a toehold-mediated strand displacement (TMSD) system to remove DNA from magnetic beads for endpoint detection.

Design of the autoPiLOT reaction processor.

The automated Pi-powered looping oligonucleotide transporter (autoPiLOT) is an automated reaction processing device controlled by a Raspberry Pi B 3+ microcomputer. The Pi is connected via USB to two Arduino Unos, a sensor Arduino and a motor Arduino. Both Arduinos are also connected to a common button that, when pressed by the user, activates different segments of their onboard code. A circuit diagram is shown in **Figure 29**. The master code for the Raspberry Pi, as well as the onboard code for both Arduinos, are available upon request.

Two QRD1114 infrared sensors/emitters are connected to the sensor Arduino for detection of liquid/air interfaces. A stepper motor (Applied Motion Products STR4) is connected to the motor Arduino, which turns gears controlling the movement of the microfluidic tubing. Fluorinated ethylene propylene

Table 6. Oligonucleotide sequences used in Chapter 4.

Name	5' mod	3' mod	Sequence (5' – 3')
U1-a	FAM/TXR		CTAGCTCATACATC_ATCCTATCTATCCAGAC_ TCTCACACGTACTC
U1-a*			TCGCTCTTACAAGGCA_CTAGCTCATACATC_ ATCCTATCTATCCAGAC_TCTCACACGTACTC
U1-b	FAM/TXR		CTAGCTCATACATC_GTCTGGATAGATAGGAT_ TCTCACACGTACTC
U2-a	FAM/TXR		GATGTATGAGCTAG_GAGATGCAATCGACTGT_ GAGTACGTGTGAGA
U2-b	FAM/TXR		GATGTATGAGCTAG_ACAGTCGATTGCATCTC_ GAGTACGTGTGAGA
Capture	Biotin		TTTTTTTTTT_CTCATTCACCTACG
Target			TGCCTTGTAAGAGCGA_CGTAGGTGAATGAG
U1-a* tag			GTCAGTGA_TCGCTCTTACAAGGCA_ CTAGCTCATACATC_ATCCTATCTATCCAGAC_ TCTCACACGTACTC
U1* removal			TGCCTTGTAAGAGCGA_TCACTGAC
S. mansoni capture	Biotin		TTTTTTTTTT_ATATTAACGCCCACG
S. mansoni target			GATTATTTGCGAGAG_CGTGGGCGTTAATAT
S. mansoni U1-a*			CTCTCGCAAATAATC_CTAGCTCATACATC_ ATCCTATCTATCCAGAC_TCTCACACGTACTC

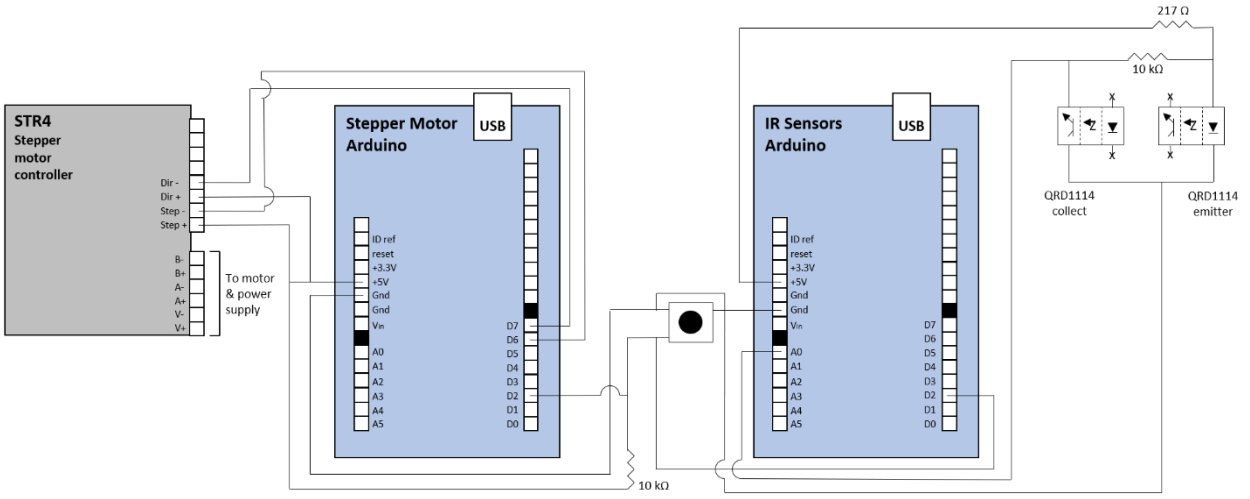

Figure 29. Circuit diagram for the autoPiLOT device. Both Arduinos are connected via USB to the Raspberry Pi B 3+. The button in the center is used at the start of the run to initiate specific portions of the onboard Arduino code.

(FEP) tubing – also commonly called PTFE tubing – with 1/8" outer-diameter and 3/32" inner-diameter (McMaster-Carr, 9369T24) was used to house the reaction contents. 5/8" x 5/8" x 1/4" neodymium magnets (K&J Magnetics Inc, BAA4) were used to control the magnetic beads. A Qiagen ESElog fluorometer was used for fluorescence measurements. Housing for the tubing, magnets, and fluorometer was 3D-printed, and the 3D drawing is also available upon request.

Gel electrophoresis studies.

A series of experiments were conducted using agarose gel electrophoresis to investigate whether the predicted DNA hybridization events were taking place. Gels contained 3% agarose in 0.5X TBE buffer, and were stained with 1X GelRed nucleic acid stain. An ultra-low range DNA ladder (ThermoFisher, 10597012) was included in each gel at a concentration of 2 ng/µL. Gels were run at 60V for approximately 1 hour, then imaged using a Bio-Rad Gel Doc EZ Imager.

Dumbbell formation.

To form the double-stranded dumbbell structures, the two oligonucleotides (for example, U1-a and U1-b form dumbbell U1) were combined at equal molar ratios to the desired final concentration and then

heated with the following thermal profile: 95 °C for 5 minutes, followed by 50 °C for 10 minutes, followed by 37 °C for 10 minutes. The dumbbells were then stored at room temperature until use. For experiments using both D-DNA and L-DNA dumbbells, both D-DNA and L-DNA were combined in the same tube. For example, D-DNA U1-a and U1-b were combined with L-DNA U1-a and U1-b in the same tube for a final solution of right- and left-handed U1.

Magnetic bead functionalization.

Dynabeads MyOne Streptavidin T1 magnetic beads (ThermoFisher, 65601) were functionalized with a biotinylated capture probe designed to bind the DNA target of interest. First, the beads were washed 3X using hybridization buffer (5X SSC buffer + 0.05% Tween 20). Each wash consists of magnetically separating the beads from solution and, while separated, removing the supernatant and adding fresh buffer. After washing, the beads were resuspended in the biotinylated capture probe at a ratio of 2.5 nanomoles DNA per mg beads, briefly vortexed, and incubated on a rotisserie for 20 minutes. The beads were then washed 3X with hybridization buffer and resuspended in blocking buffer (1X PBS + 16 µM free biotin + 0.05% Tween 20) and incubated on the rotisserie for 30 minutes. Experiments investigating other blocking methods used blocking buffers in which the free biotin was replaced with 2% BSA by volume, 200 µg/mL salmon sperm DNA, or removed altogether. The beads were then washed 3X with hybridization buffer and stored in stocking buffer (1X PBS + 0.05% Tween 20) at a final concentration of 1 mg/mL.

Dumbbell amplification reactions.

50 µg of functionalized magnetic beads were used in each reaction. The beads were washed 3X in hybridization buffer and resuspended in 100 µL of sample solution. The solution was vortexed to disperse the beads throughout and incubated on a rotating rotisserie for 30 minutes. 10 µL of U1* at 1 µM was then added, and the beads incubated for another 30 minutes on the rotisserie. The beads were then washed 3X in hybridization buffer, and resuspended in 75 µL hybridization buffer. At this point the functionalized

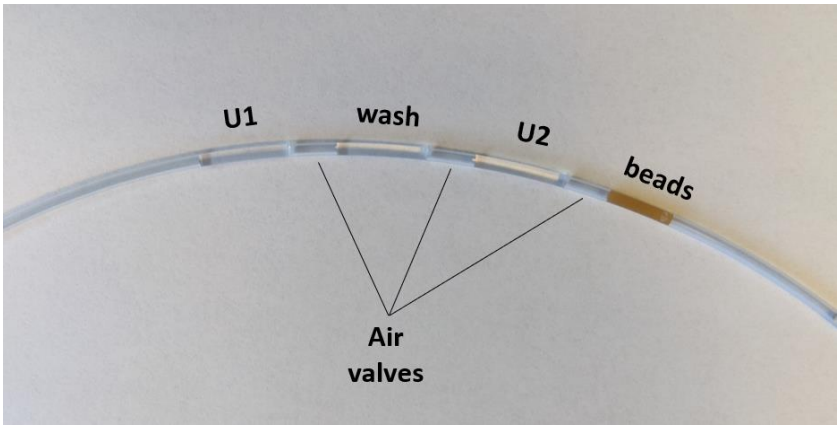

Figure 30. Picture of a pre-arrayed reaction cassette for use in the autoPiLOT reaction processor.

beads have bound target, which has in turn bound the first dumbbell U1*. Incubations in dumbbells U1 and U2 were performed using the autoPiLOT reaction processor.

The microfluidic FEP tubing was loaded with the following fluid chambers, each separated by a small air gap approximately 1 cm in length: 100 µL U1 at 250 nM, 100 µL hybridization buffer, 100 µL U2 at 250 nM, 100 µL magnetic bead solution. To load a fluid chamber into the tubing, the liquid was simply pipetted directly into the tube with the pipette tip flush against the opening. The tubing was then gently tipped to move the fluid chamber further along, clearing room for the next solution to be inserted. After the four fluid chambers were loaded in the tubing, both ends were sealed with Cha-seal tube sealing compound (cat #510). The loaded tube (shown in **Figure 30**) was run on the autoPiLOT to move the magnetic beads back and forth between the two dumbbell solutions, reading fluorescence on the beads in the wash chamber after every other dumbbell incubation.

4.3 Results

Validation of DNA hybridization events.

Each dumbbell consists of two partially-complementary oligonucleotides; **Figure 31** shows a full breakdown of each dumbbell and its components. Briefly, dumbbells U1 and U2 consist of U1-a, U1-b, U2-a, and U2-b, where a and b are used to denote the two strands in each dumbbell. U1* is a modified version of U1 with an extra binding domain on the 5’ end of U1-a to bind to the target DNA. U1* serves as

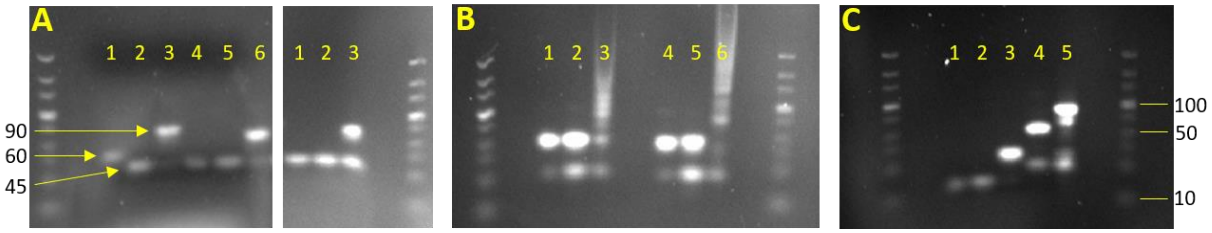

Figure 31. Gel electrophoresis results for D-DNA dumbbell binding studies. **A.** Gel 1, lanes 1-3: U1-a*, U1-b, and U1*. Gel 1, lanes 4-6: U1-a, U1-b, and U1. Gel 2, lanes 1-3: U2-a, U2-b, and U2. **B.** Lanes 1-3: U1, U2, and U1+U2. Lanes 4-6 show the same, but with 5' FAM fluorescent labels. **C.** Lane 1: capture probe. Lane 2: target. Lane 3: capture+target. Lane 4: U1*. Lane 5: capture+target+U1*.

the bridge between the target DNA and the network of dumbbells that forms during the amplification assay. Gel electrophoresis was used to validate that the individual dumbbell strands bind to form dumbbells as predicted.

For each of the three dumbbells, the respective single-stranded components were combined at equal molar ratios and visualized on a gel to confirm hybridization into double-stranded dumbbells; these results are shown in **Figure 31A**. With the exception of U1-a*, which is 60 bases, all of the single-stranded components are 45 bases long. These can be seen as the lower bands on the gel. For dumbbells U1 and U1* (**Figure 31A**, left lanes 3 and 6), the lower band disappears when the two single-stranded components are combined and a new band is formed corresponding to 90 bases, showing that the two strands have hybridized to form the double-stranded dumbbell. The formation of dumbbell U2 appears incomplete, as there is still a prominent band at 45 bases indicative of remaining single-stranded DNA (**Figure 31A**, right lane 3). Even when different ratios of U2-a and U2-b were used, this extra band persisted (data not shown). The prominent band at 90 bases, however, is evidence that the dumbbell U2 is still forming, even if not quite as efficiently as U1 and U1*.

Next, the binding of the dumbbells to each other was examined. **Figure 31B** shows that once combined, the dumbbells form products of varying size. Distinct bands corresponding to complexes of 2, 3, and 4 dumbbells can be seen; the bands resulting from even larger complexes blend together to form a smear on the gel. This test was duplicated using FAM-labeled DNA to examine whether the presence of fluorescent labels had any apparent effect on dumbbell binding. The results (**Figure 31B**, right) show that

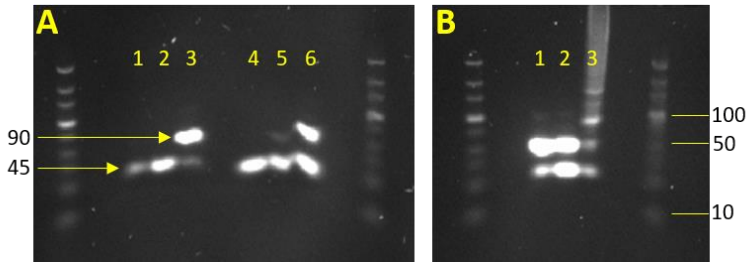

Figure 32. Gel electrophoresis for L-DNA dumbbell binding studies. **A.** Lanes 1-3: U1-a, U1-b, U1. Lanes 4-6: U2-a, U2-b, U2. **B.** Lanes 1-3 show U1, U2, and U1+U2. All L-DNA is labeled with 5' Texas Red.

the FAM-labeled dumbbells hybridized in a similar fashion as the unlabeled; if anything, the distribution of product sizes appears to skew larger than those of the unlabeled dumbbells, as indicated by the brightness of the DNA smear in the upper region. These findings validate three key assumptions moving forward: 1) the dumbbells form as expected from their single-stranded components, 2) the dumbbells bind to each other as expected to form large dumbbell complexes, and 3) attaching fluorescent labels to these dumbbells does not inhibit their affinity for one another.

Now satisfied that the D-DNA dumbbells bind as expected, the previous experiments were repeated using left-handed DNA. The L-DNA sequences are completely identical, the only differences are the chirality of the nucleotide bases and the replacement of FAM with Texas Red. As expected, the results (**Figure 32**) show that the L-DNA dumbbells exhibit the same behavior as the D-DNA; the dumbbells assemble from their single-stranded components and bind to each other to form large dumbbell networks.

Validation of target capture by magnetic beads.

There are two other key DNA binding steps in the dumbbell DNA amplification assay which were not examined in the previous gel experiments: the binding of target DNA to the capture probe-functionalized beads, and the binding of U1* to the target. Both of these binding events were also examined via gel electrophoresis. The results, shown in **Figure 31C**, show that the capture and target strands (lanes 1 and 2) hybridize to form a capture-target complex (lane 3). The addition of U1* (lane 4) then creates a capture-target-U1* complex (lane 5). This suggests that the magnetic beads which have been modified with capture probe will capture the target DNA out of solution, and subsequently bind the modified dumbbell

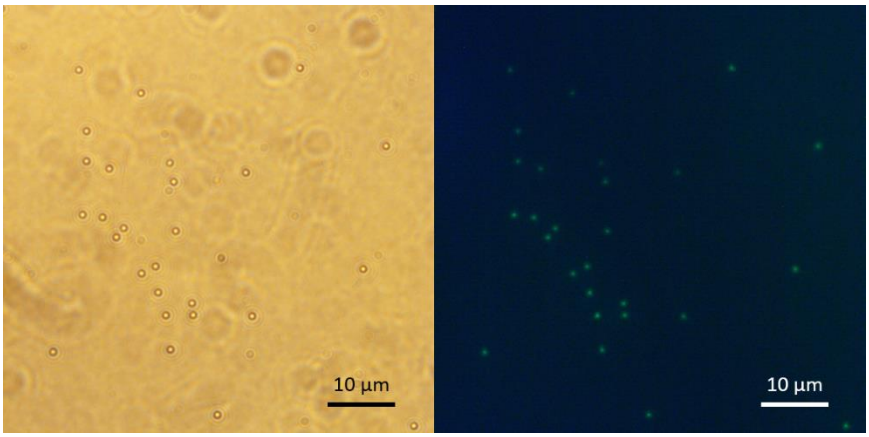

Figure 33. 50X magnification images of magnetic beads which have been incubated in target, followed by FAM-labeled U1*. Left and right images are brightfield and fluorescence images, respectively. The small 1 µM dots are the magnetic beads, visible in both images. The larger, blurry circles in the brightfield image are aberrations caused by dust on the lens.

U1*. The presence of U1* provides a starting point for cyclical dumbbell amplification. Microscopy was also used to confirm that the fluorescently-labeled U1* was indeed attached to the magnetic beads. **Figure 33** shows beads which have been incubated in target DNA, followed by the FAM-labeled U1*, using brightfield imaging and fluorescence imaging. The fluorescence image shows that FAM (in green) has attached to the beads, which confirms that the binding steps shown in **Figure 31C** also occur when bound to the surface of magnetic beads.

Automation using the autoPiLOT reaction processor.

The automated Pi-powered looping oligonucleotide transporter (autoPiLOT) is shown in **Figure 34**. The housing was 3D-printed to hold the magnets, IR sensors, fluorometer, and microfluidic tubing. Not pictured is the Raspberry Pi microcomputer and Arduinos which control the device. The low cost and portability of these components make this device easily transportable and independent of a laptop or other computer for operation. The microfluidic tubing is held between the gears, which are controlled by a stepper motor. Rotation of the gears therefore moves the microfluidic tubing which contains the various reaction fluids, as previously described.[141, 142]

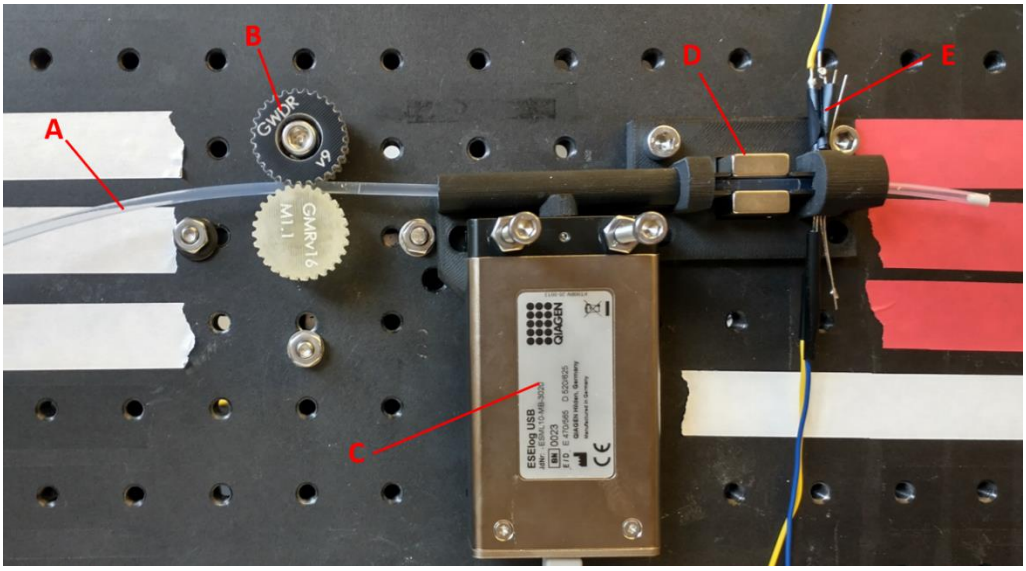

Figure 34. Photograph of the autoPiLOT reaction processor. Microfluidic polymer tubing (A) contains the reaction solutions. Two gears (B) controlled by a stepper motor move the tubing. A fluorometer (C) measures the fluorescence on the beads inside a light-tight chamber. Two neodynium magnets (D) hold the magnetic beads in their field. An IR sensor/receiver pair (E) detects the liquid/air interfaces in the tubing.

To account for variations in air gap size or fluid volume during the preparation of the reaction cassette, a pair of infrared sensor/receivers was interfaced with the system to detect the locations of the liquid/air interfaces in the tubing. Before performing the cyclical amplification reaction, a "reconnaissance run" is performed which detects changes in IR transmittance as the tubing moves from one end to the other. These changes in transmission indicate a change from liquid to air, and the locations and sizes of each fluid chamber are mapped using this information. Because it uses these measurements to guide the movement of the tubing, the autoPiLOT reaction is adaptable to variations in the pre-loaded reaction cassettes.

The movement of the magnetic beads between chambers is a result of the stationary magnetic field holding the beads as the tubing is moved by the gears. Tween 20 decreases the surface tension of the fluid chambers, which allows the beads to break through the interface. Several different concentrations of Tween were tested to see if they impacted the binding of the dumbbells to one another, and the results (shown in **Figure 35**) show that none inhibited binding. Since dumbbell binding appeared equally efficient for all tested buffer conditions, 0.05% Tween in 5X SSC buffer was used in accordance with the protocol for the original dumbbell assay.[1]

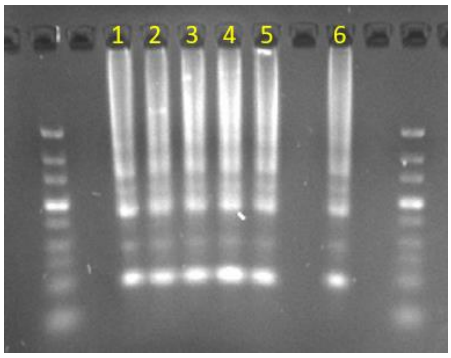

Figure 35. Gel electrophoresis results showing U1+U2 in several buffer conditions. Lanes 1-2: 2X and 5X SSC buffer. Lanes 3-5: 5X SSC with 0.1, 0.05, and 0.025% Tween 20, respectively. Lanes 6 has been vortexed with added magnetic beads just prior to loading the gel.

The movement of the magnetic beads through the four reaction chambers (shown in **Figure 30**) is as follows: from their starting place in the beads chamber, they are carried into U2. Here the beads are mixed and then removed from the magnetic field (via a fast movement speed) and then incubated for 30 minutes. The beads are then recollected in the magnetic field and carried into the wash chamber, where they are dispersed across the length of the chamber. The wash chamber is moved across the optical path of the fluorometer for fluorescence readings, and then the beads are transported into U1. Again, they are mixed and incubated to bind dumbbells. The beads are then moved in the reverse direction to U2, and the cycle begins again. Fluorescence measurements are therefore collected after dumbbell incubations number 1, 3, 5, etc.

Fluorescence measurements reflect the amount of DNA on the beads.

One of the features that makes PCR a gold standard NAT is the quantitative information gained by real-time fluorescence measurements. Fluorescence is read during each thermal cycle to create fluorescence vs cycle data, and this data can be used to estimate the starting amount of target DNA. To achieve real-time fluorescence measurements in the autoPiLOT assay, fluorescence was measured directly on the surface of the beads. Capture probe-functionalized magnetic beads were incubated with varying amounts of FAM-labeled target DNA, shown in black in **Figure 36**. The resulting fluorescence curve demonstrates that the autoPiLOT fluorescence readings are directly proportional to the amount of DNA attached to the beads.

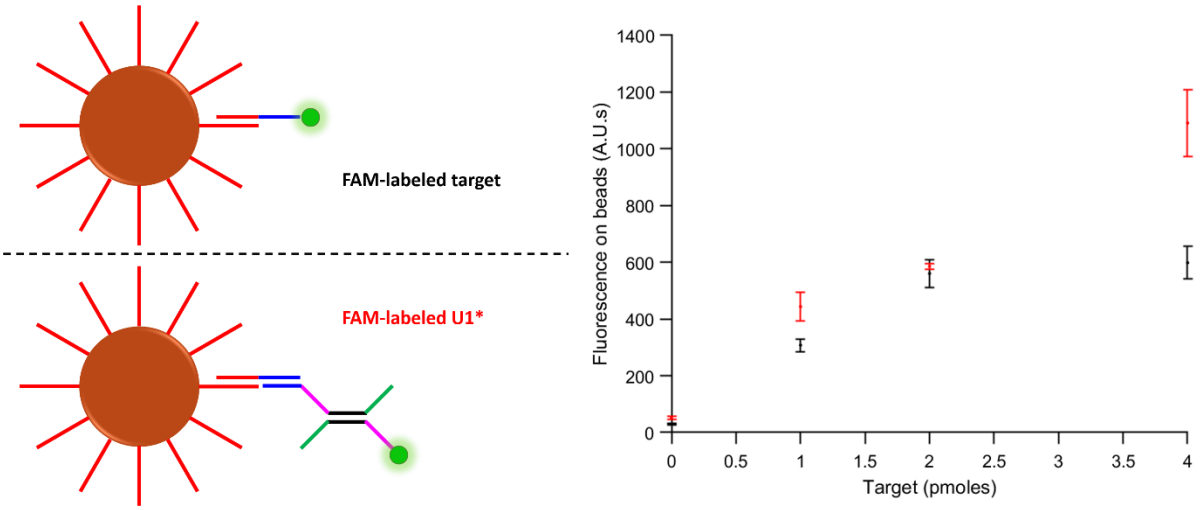

Figure 36. Fluorescence measurements directly on magnetic beads confirm target (upper left panel) and subsequent U1* binding (lower left panel). Beads incubated in varying amounts of FAM-labeled target were measured (in black), and these results were compared to beads incubated in equal amounts of unlabeled target, followed by FAM-labeled U1* (in red). The mean of three trials ± one standard deviation is shown.

Next, the same experiment was performed using unlabeled target DNA and followed by incubating with FAM-labeled U1*. Just as each target had one FAM fluorophore in the previous design, each target should bind one FAM-labeled U1* in this design. The results (**Figure 36**, red points) show that the two fluorescence curves match up very well at lower concentrations of target DNA. The U1* fluorescence tapers off at higher concentrations compared to that of the target. One possible explanation for this discrepancy is that when the beads already have a large amount of their surfaces covered in target DNA, there is a crowding effect that hinders the binding of the larger U1* structures. If true, this would suggest that the amplification observed in the autoPiLOT assay will also taper off as the bead surfaces become too overcrowded.

Performance of parallel L-DNA dumbbells.

The amplification behavior of L-DNA control dumbbells was measured to validate that it was an accurate measure of the non-specific amplification of the D-DNA dumbbells. The fluorometer in the autoPiLOT reaction processor has two fluorescent channels, one that detects FAM on the D-DNA and one that detects TXR on the L-DNA. The first step was to ensure that the intensities of these two channels were adjusted such that D-DNA dumbbells produced a signal equal to that of L-DNA dumbbells. The gain of the

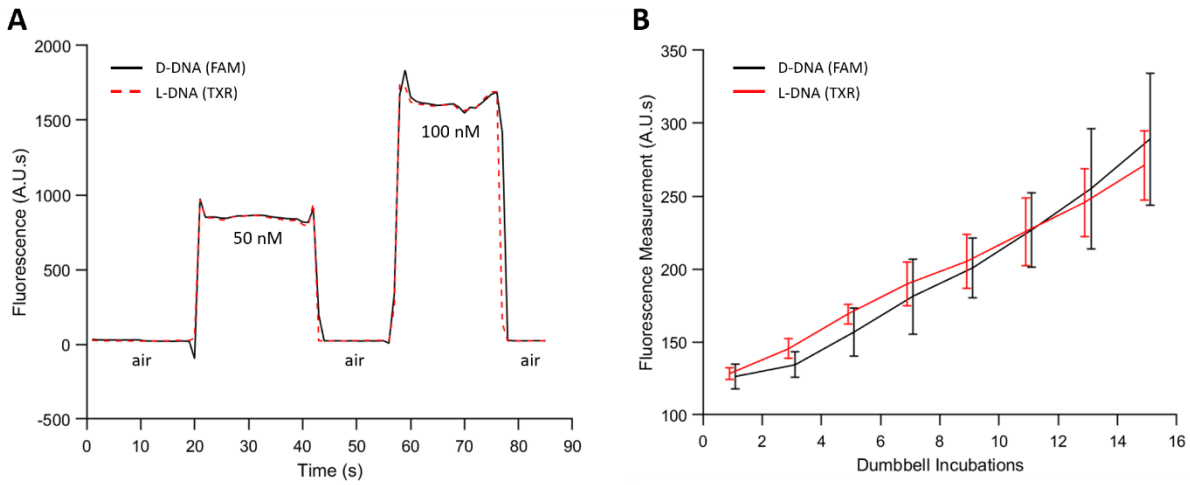

Figure 37. Matching D-DNA and L-DNA fluorescent signals in the autoPiLOT. **A.** Reaction chambers containing D-DNA and L-DNA dumbbells at 50 and 100 nM were passed through the optical path of the autoPiLOT fluorometer. **B.** No-target control reactions performed on the autoPiLOT measuring both D-DNA (black) and L-DNA (red) fluorescence. The mean of three trials ± one standard deviation is shown.

TXR channel was adjusted until the fluorescent signal was equal across multiple dumbbell concentrations (see **Figure 37A**). Moving forward, the magnitudes of fluorescent measurements are assumed to be directly comparable between D-DNA and L-DNA; matching measurements indicate matching amounts of dumbbells.

Next, negative control reactions were performed using the autoPiLOT. No target was bound by the beads, so only non-specific amplification was observed. The fluorescent measurements for both D-DNA and L-DNA dumbbells over the course of 15 dumbbell incubations are shown in **Figure 37B**. The amplification of both enantiomers is virtually identical, with no statistically-significant difference found for the readings at any point during the assay. These findings confirm the hypothesis that the amplification of the left-handed dumbbells matches the non-specific amplification of the right-handed dumbbells.

Finally, autoPiLOT amplification was compared between samples with and without L-DNA dumbbells included. Samples contained $3*10^{11}$ copies of target to ensure that amplification was high, and any differences in performance caused by the presence of the L-DNA would be exaggerated. Over the course of 15 dumbbell incubations, the D-DNA amplification (shown in **Figure 38**) appears identical regardless of whether or not L-DNA dumbbells have been included. The parallel L-DNA dumbbells have

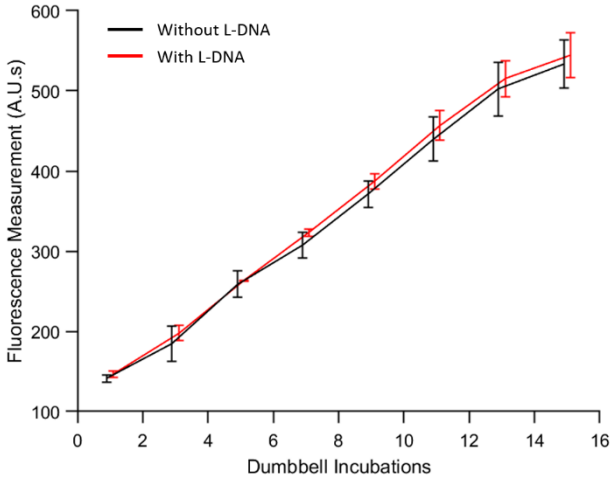

Figure 38. Comparison of D-DNA amplification with (red) and without (black) parallel L-DNA dumbbells included. The mean of three trials ± one standard deviation is shown.

now exhibited two key traits: they amplify at a rate equal to the non-specific amplification of the D-DNA dumbbells, and they do not impact the amplification of the D-DNA dumbbells. These findings demonstrate the utility of a dual-chirality design as a means to measure both target-induced amplification and non-specific amplification in a single reaction.

AutoPiLOT performance and limit of detection studies.

To determine the analytical limit of detection for the autoPiLOT reaction, serial dilutions of target DNA ranging from $3*10^{11}$ to $3*10^{5}$ copies per reaction were amplified for 15 cycles of 30-minute incubations. The D-DNA amplification curves for several of these target concentrations are shown in **Figure 39A**. The slopes of the amplification curves increase with increasing target DNA, resulting in increased fluorescent intensity, especially at later cycles. To interpret the results of a dual-chirality dumbbell amplification reaction, the signals from both the D-DNA and L-DNA dumbbells were compared. This eliminates the need to perform no-target control reactions. The change in fluorescent signal can be calculated by simply subtracting the first fluorescent measurement from each subsequent measurement; the ratio of change in D-DNA to change in L-DNA was used to compare the two signals. Let this ratio be called the signal ratio. The signal ratio changes with each new fluorescent measurement, but in general tends to

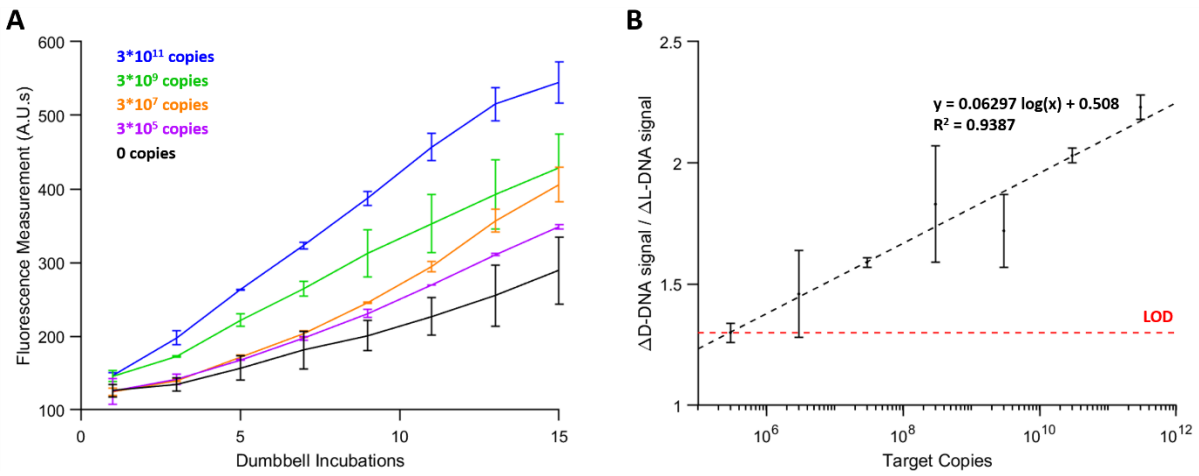

Figure 39. A. D-DNA amplification curves for autoPiLOT trials for a range of target copy numbers. **B.** Signal ratio, or the ratio of change in D-DNA signal to change in L-DNA signal after 15 dumbbell incubations, is plotted (black dots) as a function of target copy number. A logarithmic line-of-best-fit is overlaid as a black dashed line. The red dashed line represents the threshold signal ratio used to determine the limit of detection.

increase with additional incubations. **Figure 39B** shows the signal ratio after 15 dumbbell incubations as a function of target copy number. Diagnostically, to determine whether a given sample is positive, there must be a threshold signal ratio; an observed signal ratio greater than this threshold is interpreted as a positive result. A ratio of 1 may seem like a reasonable threshold, since D-DNA and L-DNA amplification are expected to be equal in the absence of target DNA. However, there is a certain level of expected noise that means a negative sample may still exceed a signal ratio of 1. To determine a threshold, three autoPiLOT reactions were performed on separate days, and the formula $\mu_0 + 3\sigma_0$ was used, where μ_0 and σ_0 represent the mean and standard deviation of the signal ratio. Using this calculation, a signal ratio of 1.30 was determined as the threshold to determine positive results. This value is plotted as a red dashed line in **Figure 39B**, and intersects with the linear line-of-best-fit at $3*10^5$ copies. Thus, the limit of detection of this reaction was determined to be approximately $3*10^5$ copies/reaction, or 5 fM.

Application of the autoPiLOT to detection of S. mansoni DNA.

The previous experiments have all used the originally-published development target sequence (see **Table 6**, target) to avoid implementing new DNA sequences while developing the autoPiLOT reaction

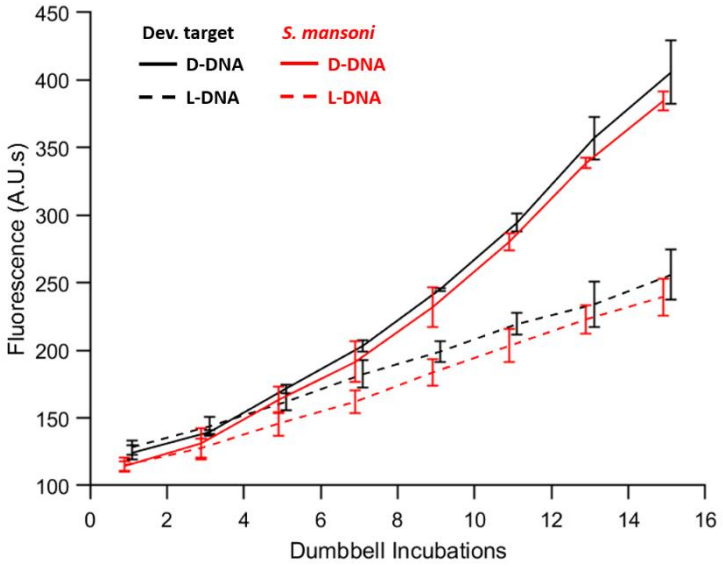

Figure 40. Comparison of autoPiLOT performance for detection of the development target sequence (black) and the S. mansoni target sequence (red). D-DNA signals are shown as solid lines, and L-DNA signals as dashed lines. The mean of three trials ± one standard deviation is shown.

platform. To apply this platform in a diagnostic setting, several DNA elements must be redesigned to integrate a new target sequence. As an example, DNA from the genome of *Schistosoma mansoni* was chosen as a new target. *S. mansoni* is the most widespread member of the family of parasitic flatworms which cause schistosomiasis, a leading neglected tropical disease responsible for the loss of 4.5 million disability-adjusted life years (DALYs).[3-5] The sequence selected as a target is part of a 121-bp tandem repeat sequence which comprises roughly 12% of the *S. mansoni* genome, and has previously been targeted with PCR assays.[26, 79, 84] Fortunately, the dumbbells U1 and U2 do not need to be redesigned to integrate a new target sequence; only the target-binding domain on U1-a* and the capture sequence need to be changed to bind the desired target.

New magnetic beads were functionalized using the *S. mansoni* capture probe, and the autoPiLOT assay was performed on samples containing $3*10^7$ copies of the *S. mansoni* target. The results are shown in **Figure 40** alongside the results for the original target sequence. The signal ratio after 15 cycles was calculated as 2.21 ± 0.09 for the original target and 2.18 ± 0.23 for the *S. mansoni* target. These results show virtually identical assay performance for both targets, suggesting that the autoPiLOT assay can be

applied to new targets without sacrificing performance. Although the limit of detection was not determined for the new target, the identical performance at a concentration of $3*10^7$ copies/reaction suggests that it would be comparable to previously-determined limit of $3*10^5$ copies/reaction.

4.4 Discussion

The dumbbell DNA amplification scheme has previously been shown to be a highly-sensitive, non-enzymatic method of detecting target DNA.[1] The largest obstacles to its use in diagnostic applications were the extremely high number of manual pipetting steps and amount of hands-on time required, and the need for an additional control reaction. The autoPiLOT platform has overcome these obstacles through automation of the reaction in a self-contained, microfluidic reaction cassette. The components are primarily 3D-printed parts and low-cost electronics, making the autoPiLOT a low-resource compatible diagnostic platform. Real-time fluorescence measurements were shown to reflect the amount of DNA which had accumulated on the magnetic beads. Signal amplification was approximately linear, and the slope increased with increasing amounts of target DNA in the sample. The autoPiLOT assay exhibited a limit of detection of 5 fM, and showed promising results when applied to the detection of *S. mansoni* DNA, demonstrating the potential for a sensitive, low-cost, point-of-care non-enzymatic NAT.

The autoPiLOT assay also demonstrates the utility of left-handed L-DNA as an internal control. Whereas a traditional assay format would require the performance of two parallel reactions, one with and one without target, for interpretation of results, the dual- chirality design used here discretely measured both specific and non-specific signals in the same reaction. In addition to saving time and reagents, this opens the door to testing “dirty” biological samples which may exhibit varying rates of non-specific amplification that cannot be accurately simulated with a parallel control reaction.

Despite the previously-demonstrated exponential amplification of the dumbbell amplification assay, the observed amplification of the autoPiLOT is approximately linear. This discrepancy is likely due to a combination of factors. When the beads are transported into a new chamber in the autoPiLOT, they are briefly mixed back and forth to disperse them across the length of the chamber. Despite this, the beads

quickly settle to the bottom of the tubing where they remain for most of the 30 minutes. Dumbbell binding efficiency would likely improve if the beads were homogenously dispersed throughout the chamber; the effective exposed surface area of the beads would be much larger. Another potential cause of decreased amplification is steric hinderance from the surrounding dumbbells. The more dumbbells are attached to the bead surface, the more chaotic and intertwined the growing network of dumbbells becomes. This would result in amplification which becomes less efficient the more dumbbells are bound; this behavior is suggested in the amplification curves shown in **Figure 39A**. At lower fluorescence values (in the 100-250 A.U. range), the amplification has some concavity indicative of exponential amplification. This is most visible for the $3*10^5$ and $3*10^7$ copy number curves. As the reaction progresses and more dumbbells attach to the beads, the curve becomes linear, and even begins to taper off at high enough values. Future work should focus on optimization of the autoPiLOT magnetic bead control strategies, in an effort to more efficiently bind dumbbells and achieve exponential amplification.

Future research should also work toward the implementation of a lower-cost fluorescence imaging system. The fluorometer used in the autoPiLOT is the only expensive component, with a price tag of several thousand dollars. Recently, smartphone-based fluorescence microscopes have grown in popularity and sophistication, bringing high quality digital cameras and multifunctionality to the point-of-care.[143, 144] It is estimated that approximately 80% of the world population uses smartphones, making a smartphone optical readout highly applicable, even in low-resource settings.[145]

An alternative strategy to avoid use of a costly fluorometer would be a colorimetric readout. The original demonstration of the dumbbell amplification assay utilized a colorimetric readout, in which dumbbells were labeled with biotin and avidin-labeled horseradish peroxidase (HRP) was added to the beads at the end of the end of the reaction.[1] Any dumbbells attached to the beads would bind the HRP, subsequently catalyzing a color change of tetramethylbenzidine. The drawback of this strategy is that it prohibits the use of two distinct readouts, one for D-DNA and one for L-DNA. The use of a dual-chirality design allowed for the monitoring of not only target signal, but also non-specific amplification in each

reaction. Switching to a colorimetric readout simplifies the autoPiLOT components, but sacrifices the innovative dual-chirality functionality.

Finally, the performance of the autoPiLOT diagnostic platform should be evaluated using real urine samples. The preliminary data presented here suggests that the autoPiLOT is an effective strategy to detect *S. mansoni* DNA, which has previously been detected in urine samples via PCR. The PCR limit of detection was reported to be 1.28 pg/mL;[84] given the highly-repeated nature of the target sequence in the genome, this corresponds to approximately 790,000 copies/mL of the target sequence. The autoPiLOT demonstrated a limit of detection of 3,000,000/mL target copies, nearly as sensitive as PCR. Furthermore, urine is an ideal sample type for magnetic bead nucleic acid extractions, as large volumes are easily obtained. These characteristics suggest that the autoPiLOT has the potential to be a highly-sensitive, low-resource, non-enzymatic NAT, and the first of its kind.

Chapter 5

5. CONCLUSIONS AND FUTURE DIRECTIONS

Summary of major findings.

The work in this dissertation has demonstrated the following fundamental advancements to non-enzymatic diagnostic methods: quantifying the effects of different fluorescent designs on DNA hybridization, the use of a dual-chirality design in CHA to simultaneously measure target-induced amplification and leakage amplification, and the development of an automated, self-contained reaction processor to perform highly sensitive non-enzymatic dumbbell amplification assays.

In Chapter 2, six different fluorophores and four different quenching schemes (24 total combinations) were used to study the effect of fluorescence design on DNA duplex stability. All 24 designs had a stabilizing effect on the DNA, manifesting as an increased annealing temperature. Even the guanine-quenching design, in which a single guanine base replaced the BHQ2, resulted in an increase in annealing temperature, which implies that the presence of a terminal fluorophore alone causes a stabilizing effect. Distancing the BHQ2 from the fluorophore by extending the 3' end of the quencher strand decreased the magnitude of the stabilizing effect, showing that there is also an interactive effect between the fluorophore and quencher. The fluorescence design which caused the smallest shift in annealing temperature was FAM with a 10-base offset from the BHQ2. This design was compared to one in which the FAM was not offset from the BHQ2 in adaptive PCR, where thermal cycling is directly controlled by the optical signal from fluorescently-labeled L-DNA. The 0-base offset FAM design resulted in a 15% increase in reaction efficiency, demonstrating the value of using an appropriate fluorescence design.

In Chapter 3, catalyzed hairpin assembly (CHA) was studied an example of a widely-used diagnostic DNA circuit. A parallel circuit made of identical L-DNA elements was implemented to act as a built-in measure of circuit leakage. A comparison of leakages between the two enantiomeric circuits with all components at equal concentrations revealed that the L-DNA leakage, although similar in behavior, was

larger in magnitude than that of the D-DNA. By simply using less L-DNA, however, the circuit exhibited identical leakage as the D-DNA circuit, even across a wide range of different reaction conditions. The addition of the L-DNA circuit allowed for a new method of data analysis that circumvents the requirement of additional no-target control reactions. This makes application of a dual-chirality CHA test to biological samples without additional purification steps much more feasible, compared to a single-chirality design that requires consistent leakage profiles across samples. Furthermore, the dual-chirality design was found to have a comparable limit of detection (81 pM) as the single-chirality design (92 pM).

In Chapter 4, a previously-described dumbbell DNA amplification scheme was studied as an example of a nonlinear, non-enzymatic NAT. Although this assay had exhibited a reported limit of detection of 5 copies/reaction, it required over 100 pipetting steps and 18 hours to perform. Two major innovations were shown: automating the reaction to greatly reduce the hands-on time and number of pipetting steps, and once again incorporating a dual-chirality design to act as a built-in no-target control. A reaction processor was built, called the autoPiLOT, which detected the pre-arrayed fluid chambers in a microfluidic reaction cassette and moved magnetic beads back and forth through these chambers to perform the dumbbell amplification assay without any human interaction. The autoPiLOT is controlled by a Raspberry Pi microcomputer and comprised of 3D-printed parts, making this device highly accessible. Furthermore, the code and 3D drawings are all available on Github, in an effort to make this technology as open-source as possible. Following the trend started in Chapter 3, the parallel L-DNA elements in the dumbbell amplification reaction were shown to accurately mirror the non-specific amplification of the D-DNA elements. The autoPiLOT platform was able to detect as little as 3000 copies/µL of the synthetic target sequence, 4 orders of magnitude more sensitive than the dual-chirality CHA circuit. As a pilot study for the application of this platform for detection of schistosomiasis, a new target sequence from the genome of *S. mansoni* was introduced. The assay performance appeared identical for this new target, which is to be expected given the re-programmability of nucleic acid detection schemes; the autoPiLOT reaction can be adjusted to detect new targets just as easily as gold standard NATs like PCR. PCR detection of *S. mansoni* DNA has previously demonstrated a limit of detection of 1.28 pg/mL of genomic DNA in urine. Taking

into account that the target sequence is a part of a highly-repeated tandem repeat sequence, this limit of detection corresponds to an estimated 790,000 copies of the target sequence per reaction, more than double the demonstrated limit of detection of the autoPiLOT.

Broader impact.

The single largest advancement in this work is the demonstration of a dual-chirality design for non-enzymatic nucleic acid tests. The unavoidable leakage that comes with non-enzymatic DNA amplification schemes means that every diagnostic test must have a means of deciding whether the observed increase in signal is due to the presence of target nucleic acids or leakage. In a laboratory setting, this is typically done by performing a parallel negative control reaction, and using that as a comparison to the sample. In a point-of-care setting where sample processing is not feasible, this is not possible. The dual-chirality design is the first of its kind, providing distinct measures of both leakage (L-DNA) and leakage + target-induced amplification (D-DNA). The dual-chirality design can be applied to any DNA test which relies only on DNA hybridization events, opening the door to the application of these tests to "dirty" biological samples. The most powerful test in the world does no good if half of the human race has no access to it; the ability to test unprocessed samples at the point of care greatly increases the accessibility of nucleic acid testing.

The development of an automated reaction processor is another key advancement in the diagnostic field. The precision required for working with magnetic beads – specifically, magnetic separation of the beads and removal of the supernatant – has made the development of automated magnetic bead processing machines difficult. By reversing the classical "stationary beads, mobile fluids" motif and utilizing a "stationary fluids, mobile beads" motif, the ease of automation greatly increased. The Haselton laboratory has previously demonstrated automated magnetic bead processing devices, but these were simple linear processing schemes. Beads were collected from a starting solution and carried in one direction through several solutions to a final resting location. The autoPiLOT has greatly improved on this design by demonstrating bi-directional movement of the beads, as well as adaptive detection of liquid-air interfaces. These findings also suggest that even more complex microfluidic architectures are possible, allowing for

more complex reaction procedures. The fundamental goal of diagnostic tests is to detect individual molecules of interest, which exist on a scale that we humans can scarcely imagine. As diagnostic tests continue to improve, it seems only logical that the amount of human interaction with the sample will decrease. The autoPiLOT may, in turn, inspire the creation of an even more powerful and less human-operated diagnostic test.

Low-resource areas without easy access to a laboratory are most in need of powerful non-enzymatic tests, which generally require fewer resources and sample processing steps than enzymatic tests. The autoPiLOT platform is ideal for use in these low-resource areas; it is simple to use and almost entirely hands off. Schistosomiasis is a particularly well-suited application, as previously discussed, because it can be detected in urine and it has a highly-repeated sequence which inflates the target copy number. There are many other infectious diseases endemic in low-resource settings, however, which are also suitable candidates for autoPiLOT detection. Diseases such as Dengue Fever, Chikungunya, and Zika Virus may present very similar symptoms, making the correct diagnosis difficult without laboratory testing. A laundry list of diseases of the developing world contains almost entirely infectious diseases: malaria, tuberculosis, HIV, a number of respiratory tract infections, and more, all caused by pathogens with their own unique and recognizable genomes. The autoPiLOT assay is easily customized to any of these, and even has the potential to be multiplexed if additional fluorescent dyes are utilized. The highly customizable nature of the DNA elements in non-enzymatic DNA amplification tests make virtually any infectious disease a feasible target.

Future directions.

First and foremost of the future directions for this work is the application of the autoPiLOT platform to detection of *S. mansoni* DNA fragments in urine samples. The work in this dissertation stopped short of extracting DNA from urine, but there are established protocols for the extraction of urinary DNA via magnetic beads. Preliminary results suggest that the autoPiLOT may detect *S. mansoni* DNA with a sensitivity approaching that of PCR, which would be a massive milestone for a non-enzymatic NAT. The current gold standard diagnostic for schistosomiasis is microscopy, due to its ease of performance at the

point-of-care. Based on the preliminary results shown here, the autoPiLOT offers a significant improvement over microscopy in terms of sensitivity. While microscopy relies on the presence of eggs in the feces, the autoPiLOT can detect cell-free DNA in the urine, which may be present even if there are no eggs to be found. The autoPiLOT limit of detection was comparable to that of PCR for schistosomiasis, although with the caveat that PCR was extracting from urine. Testing urine samples is a necessary step to better understand how this test compares to PCR. The plan laid out by the WHO for elimination of schistosomiasis requires widespread and accurate diagnostic testing in endemic areas. A point-of-care non-enzymatic NAT with sensitivity comparable to that of PCR is the ideal test to meet the WHO criteria for diagnostic testing.

Another possible avenue for future work is the development of a lower-cost fluorescence imaging platform to interface with the autoPiLOT. The fluorometer used to detect dumbbells on the magnetic beads is the only high-cost component of the device, and thus the only obstacle to the autoPiLOT being a truly low-cost device. One option would be to use a smartphone-based imaging system. Even in low-resource settings, smartphones with powerful CCD cameras are ubiquitous. Imaging platforms which leverage the capabilities of modern smartphone cameras, typically using a reversed camera lens and optical filters, have demonstrated low-cost fluorescence imaging capabilities. Even simpler would be the use of a sensitive photodiode, coupled with simple optical filters. The main challenge in simplifying the optical setup is to do so without sacrificing sensitivity. Replacing the current fluorometer with a lower-cost imaging system would remove the last obstacle to implementing the autoPiLOT in low-resource settings where powerful non-enzymatic tests are most needed.

One more possible focus of future work is a more thorough investigation of the L-DNA properties which cause unequal leakage rates in dual-chirality CHA. Although this problem was overcome in Chapter 3 by using less L-DNA, this solution does not address the root issue, which I hypothesize is related to the differences in synthesis methods between D-DNA and L-DNA. If the dual-chirality design is to be applied to other DNA circuits, especially more complex multi-layered ones than CHA, then the L-DNA components should be at equal concentrations as the D-DNA components. The L-DNA CHA circuit exhibited higher leakage and appeared streakier when visualized on a gel, which suggests that there is a higher fraction of

impure oligonucleotides. Additional purification steps may remove these impurities, leaving a final product equally pure as the mirror-image D-DNA. An even loftier goal is the advancement of L-DNA synthesis techniques to make the overall process as similar to that of D-DNA as possible.

APPENDIX

Appendix 1. Analysis of oligonucleotide melt temperature

Throughout this text, there are many instances in which the melt temperature (also referred to as annealing temperature) is calculated based on a melt curve. Melt curves are generated by heating a sample containing the DNA of interest to 90 °C, then cooling at a rate of 1 °C/minute to a final temperature of 30 °C and measuring fluorescence at each temperature. This is performed using a Qiagen Rotor-Gene Q PCR machine. In order to detect any meaningful fluorescent signal, there must be a fluorescent reporter of hybridization state in the sample. In the case of oligonucleotides with terminal fluorophores/quenchers, no additional components are required. For unmodified oligonucleotides, an intercalating dye must be included which binds to double-stranded DNA to generate fluorescence. Therefore, end-labeled oligos produce an increase in fluorescent signal when they separate and fluorescence is un-quenched, and unmodified oligos produce a decrease in fluorescent signal when they separate and the intercalating dye disassociates.

The fluorescent signal versus temperature data is then used to take the derivative with respect to temperature (shown in **Figure 41**, denoted as dF/dT), and this forms a curve with a peak value that corresponds to the temperature at which the DNA was hybridizing at the fastest rate. That temperature corresponds to the melt temperature. However, simply taking the temperature corresponding to the maximum dF/dT value limits the resolution of the calculated melt temperature, because fluorescence was only measured in one-degree intervals. To improve the quality of the calculated melt temperature, the dF/dT data is fit to a Gaussian curve using linear regression. The Gaussian equation is of the form given in **Equation 1.1**.

$$y = ae^{-\left(\frac{x-b}{c}\right)^2} \tag{1.1}$$

The Gaussian curve peak is determined based on all of the data points taken at one-degree intervals, but may fall between these temperature values in accordance with the best-fitting curve. The temperature

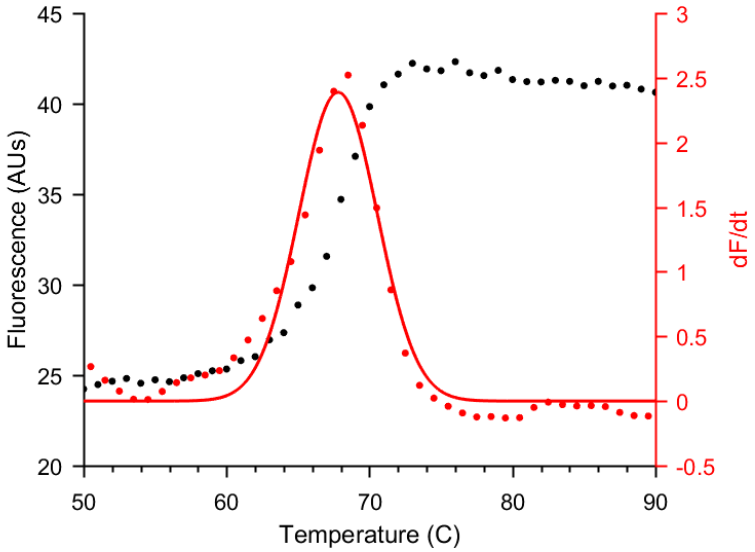

Figure 41. Example melt curve used to calculate the melt temperature of fluorescently-labeled DNA. The raw fluorescence data is shown as a function of temperature in black dots. This data is used to calculate the derivative dF/dT, shown in red dots. The dF/dT data is then fit to a Gaussian curve (red line), and the temperature of the peak is interpreted as the melt temperature.

value corresponding to the peak dF/dT value is the *b* constant in **Equation 1.1**. An example melt curve, with the Gaussian fit overlaid, is shown in **Figure 41**. In this example, the melt temperature is at 67.9 °C. In cases where fluorescence is decreasing, the Gaussian curve will be flipped over the x-axis; in this case the minimum value is calculated instead of the maximum value for an upright Gaussian curve.

Appendix 2. Modeling DNA hybridization kinetics during PCR

PCR alternates between heating and cooling phases to control hybridization of the reaction components. During the heating phase, the double-stranded DNA helices melt into single-stranded DNA. During the subsequent cooling phase, primer sequences bind to the complementary portion of the target sequence, reversibly forming primer-target complexes. This reaction is given by **Equation 2.1**, where *P*, *T*, and *C* represent primer, target, and primer-target complex, respectively.

$$P + T \leftrightarrow C \tag{2.1}$$

During adaptive PCR, the hybridization state of D-DNA is assumed to be identical to that of L-DNA. We have shown, as have others, that identical sequences of D-DNA and L-DNA have identical annealing temperatures. The rate at which the different DNA sequences bind and reach equilibrium, however, is based on the concentrations of reactants and products. This relationship is given by **Equation 2.2**, where square brackets are used to signify concentration in moles/L and k_1 and k_{-1} are the forward and reverse rate constants with units of $M^{-1}s^{-1}$ and s^{-1}, respectively.

$$\frac{d[C]}{dt} = k_1[P][T] - k_{-1}[C] \tag{2.2}$$

Since L-DNA is unaffected by polymerase, the concentrations of left-handed primers and targets do not change over the course of the reaction. Right-handed primers, however, are converted into targets via polymerase extension each cycle. Therefore, the value of $[P][T]$ for D-DNA changes each cycle. This suggests that the rate at which L-DNA primer-target complexes form tends to be different than the rate at which D-DNA primer-target complexes form. These equations, however, utilize rate constants which vary as a function of temperature; this explains why equilibrium state for a DNA duplex is double-stranded at 37 °C but single-stranded at 90 °C. If we assume that the reaction is at equilibrium at the peak PCR temperature when all DNA has melted, then as the temperature begins to drop, the equilibrium state begins to shift. This shift in equilibrium is a continuous function, but we can imagine it as a discrete function in which the temperature instantaneously drops a small interval and is held there for a small amount of time before dropping once more. Depending on the rate of cooling, the reaction may or may not have time to

reach equilibrium between each of these drops. The amount of time required to reach equilibrium after a perturbation in reaction conditions – such as a decrease in temperature – is known as the relaxation time[146] and is described by **Equation 2.3**.

$$1/\tau = k_1[\bar{P} + \bar{T}] + k_{-1} \quad (2.3)$$

Here τ refers to relaxation time and $[\bar{P}]$ and $[\bar{T}]$ refer to the equilibrium concentrations of primer and target, respectively. The value $[\bar{P} + \bar{T}]$ does not change from cycle-to-cycle for either D-DNA or L-DNA, because any decrease in primer concentration is accompanied by an equal increase in target concentration. Based on this, we expect that varying the primer-to-target ratio P:T will not result in a difference in hybridization behavior between D-DNA and L-DNA, provided the rate of cooling is slow enough that the reaction remains at chemical equilibrium throughout.

Appendix 3. A computational model for PCR

Computational models can be used as tools to guide experimental designs; countless "experiments" can be simulated in the blink of an eye on a computer microchip. Along these lines, a computational PCR model has the potential to shed light on the role of different parameters in the reaction. Before explaining how such a model was created, an overview of the underlying reactions occurring during PCR is required. The main characters in a PCR reaction are the double-stranded DNA, the forward and reverse primers, polymerase, and dNTPs, which are the building blocks of DNA. The reaction consists of two main phases: the melt phase and annealing phase. During the melt phase, all dsDNA dissociates, leaving only ssDNA. During the annealing phase, the forward and reverse primers bind to the sense and antisense strands of the target, respectively. Polymerase is then able to extend these primers into the full target complement by using the dNTPs as building blocks. Also possible during the annealing phase is that the two complementary target strands bind to each other. These chemical reactions are outlined below in **Equations 3.1 – 3.3**, where P_1 and P_2 are the forward and reverse primers, T_1 and T_2 are the sense and antisense strands of the target, and k values are the kinetic rate constants.

$$P_1 + T_1 \overset{k_1}{\leftrightarrow} PT_1 \tag{3.1}$$

$$P_2 + T_2 \overset{k_2}{\leftrightarrow} PT_2 \tag{3.2}$$

$$T_1 + T_2 \overset{k_3}{\leftrightarrow} TT \tag{3.3}$$

Based on these equations, differential equations describing the rate of association and dissociation between DNA elements can be written. The rate of change of each element is dependent on both the concentration its associated rate constant. Each of the three above reactions is reversible, with rates described by k_1, k_2, and k_3 in the forward direction, and k_{-1}, k_{-2}, and k_{-3} in the reverse direction. By summing the differential equations arising from all the pathways by which each DNA element may be gained or lost (for example, P_1 may be gained by the dissociation of PT_1 and also lost by binding to T_1 to form PT_1), **Equations 3.4 – 3.10** are obtained.

$$\frac{dP_1}{dt} = -k_1[P_1][T_1] + k_{-1}[PT_1] \tag{3.4}$$

$$\frac{dP_2}{dt} = -k_2[P_2][T_2] + k_{-2}[PT_2] \tag{3.5}$$

$$\frac{dT_1}{dt} = -k_1[P_1][T_1] + k_{-1}[PT_1] - k_3[T_1][T_2] + k_{-3}[TT] \tag{3.6}$$

$$\frac{dT_2}{dt} = -k_2[P_2][T_2] + k_{-2}[PT_2] - k_3[T_1][T_2] + k_{-3}[TT] \tag{3.7}$$

$$\frac{dPT_1}{dt} = k_1[P_1][T_1] - k_{-1}[PT_1] \tag{3.8}$$

$$\frac{dPT_2}{dt} = k_2[P_2][T_2] - k_{-2}[PT_2] \tag{3.9}$$

$$\frac{dTT}{dt} = k_3[T_1][T_2] - k_{-3}[TT] \tag{3.10}$$

Now armed with a system of differential equations describing behavior during the annealing phase, the ode15s function in Matlab was used to solve these equations analytically during each annealing phase of PCR. Several assumptions were made in the construction of this model: 1) there are sufficient dNTPs that they are never a rate-limiting factor, 2) polymerase has sufficient time to extend all available primers into targets, and 3) the temperatures in between the melting and annealing phases are not accounted for. The user input variables are concentration of target, concentration of each primer, each kinetic rate constant, length of the annealing phase, and number of cycles. As a demonstration of some of the uses of this model, several plots were created to show the predicted effect of changing different reaction parameters, shown in **Figure 42**. The commented Matlab code is also shown in the following pages.

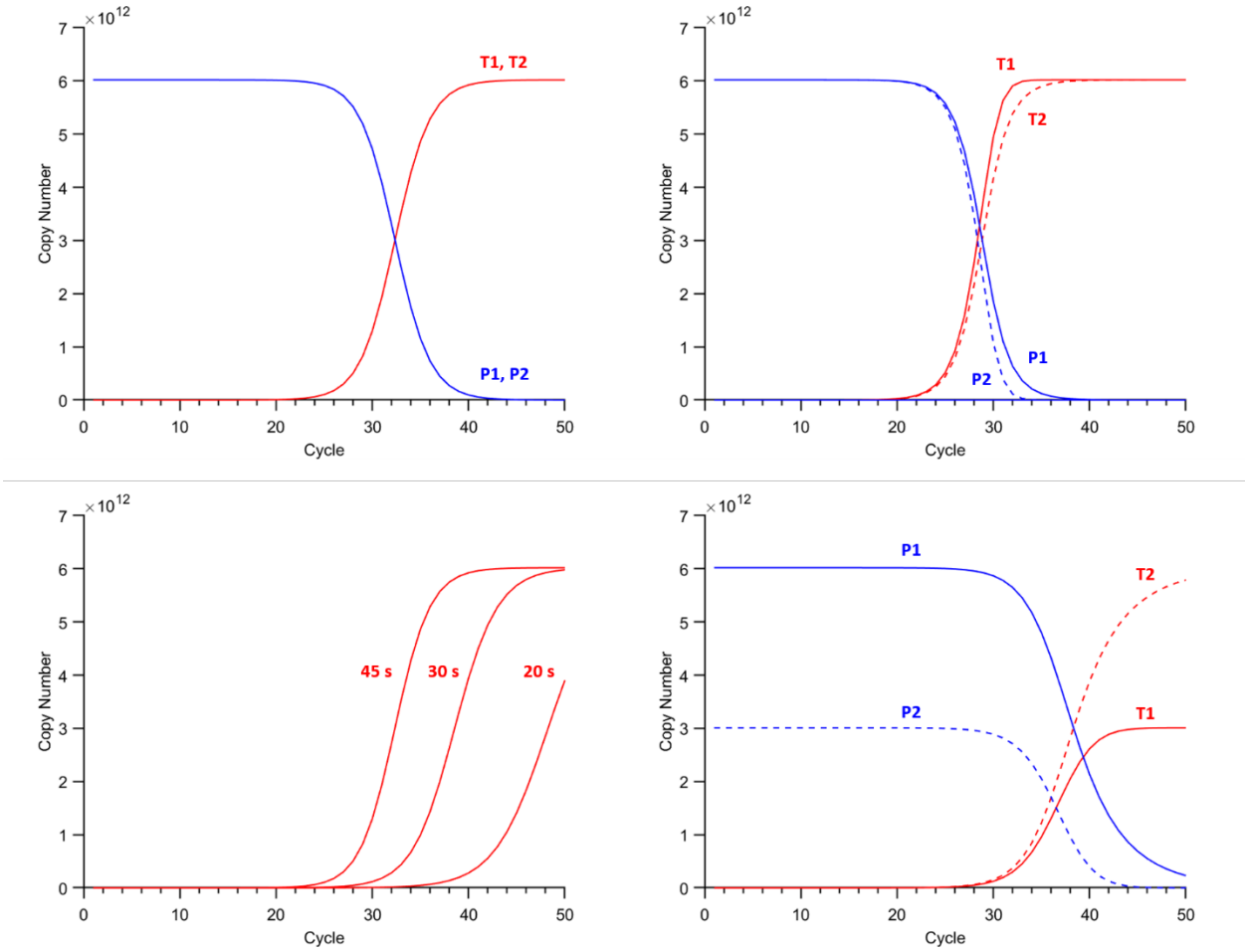

Figure 42. Graphs showing PCR simulations created using the Matlab model. **Top left:** 10^5 copies target, 400 nM each primer, 45 seconds annealing time. Both strands of target are shown in red (they are equal), and primers in blue. **Top right:** Identical conditions as top left, but with rate constants that reflect a higher affinity between P_2 and T_2 than for P_1 and T_1. **Bottom left:** Identical conditions as top left, but three different times are used for the length of the annealing phase. Target copies are shown in red for each condition. **Bottom right:** Identical conditions as top left, but with half the starting concentration of P_2. The sense and antisense strands of target are shown in red as solid and dashed lines, respectively. The two primers are shown in blue as solid and dashed lines.

Matlab code for PCR model.

```
%% Modeling PCR
%  2020-04-09
clear; clf; clc;

T = 1000;                % target copy numbers
numcycles = 50;          % number of PCR cycles
tanneal = 45;            % length of anneal phase (s)

k1 = 3*10^6;                     % units: M^-1 s^-1
k_1 = 10^-3;
k2 = 3*10^6;
k_2 = 10^-3;
k3 = 9*10^6;                     % these are different bc target duplex is
k_3 = 3*10^-3;                   % longer and thermodynamically more stable

k1 = k1*1000/(6.02*10^23);       % convert to copies/s
k_1 = k_1*1000/(6.02*10^23);
k2 = k2*1000/(6.02*10^23);
k_2 = k_2*1000/(6.02*10^23);
k3 = k3*1000/(6.02*10^23);
k_3 = k_3*1000/(6.02*10^23);

P1val = zeros(1,numcycles);      % these will log values over the course
P2val = zeros(1,numcycles);      % of the reaction for both primers and
T1val = zeros(1,numcycles);      % both strands of the target
T2val = zeros(1,numcycles);


    P1 = 400E-9;                     % conc of primer1 (M)
    P2 = P1;                         % conc of primers2 (M)

    P1 = P1*(25E-6)*(6.02E23);       % convert primers to copies
    P2 = P2*(25E-6)*(6.02E23);
    T1 = T;
    T2 = T;

    P1T1 = 0;
    P2T2 = 0;
    TT = 0;

    P1val(1) = P1;
    P2val(1) = P2;
    T1val(1) = T1;
    T2val(1) = T2;

for i=1:numcycles
    % ANNEALING PHASE
    % Let C(1)=P1 C(2)=P2 C(3)=T1 C(4)=T2 C(5)=P1T1 C(6)=P2T2 C(7)=TT
    fpcr = @(t1,C) [-k1*C(1)*C(3) + k_1*C(5); ...
                    -k2*C(2)*C(4) + k_2*C(6); ...
                    -k1*C(1)*C(3) + k_1*C(5) - k3*C(3)*C(4) + k_3*C(7); ...
                    -k2*C(2)*C(4) + k_2*C(6) - k3*C(3)*C(4) + k_3*C(7); ...
                    k1*C(1)*C(3) - k_1*C(5); ...
                    k2*C(2)*C(4) - k_2*C(6); ...
                    k3*C(3)*C(4) - k_3*C(7)];
    [t1,num1] = ode15s(fpcr, [0 tanneal], [P1 P2 T1 T2 P1T1 P2T2 TT]);
```

```
    P1 = num1(end,1);
    P2 = num1(end,2);
    T1 = num1(end,3);
    T2 = num1(end,4);
    P1T1 = num1(end,5);
    P2T2 = num1(end,6);
    TT = num1(end,7);

    % POLYMERASE EXTENSION PHASE
    % assuming that polymerase is able to extend all annealed primers!
    TT = TT + P1T1 + P2T2;
    P1T1 = 0;
    P2T2 = 0;

    % MELT PHASE
    T1 = T1 + TT;
    T2 = T2 + TT;
    TT = 0;

    % LOG DATA FOR PLOTS
    P1val(i) = P1;
    P2val(i) = P2;
    T1val(i) = T1;
    T2val(i) = T2;
end

x = 1:numcycles;

figure(1)
hold on
h1 = plot(x, T1val, 'r');
h2 = plot(x, T2val, 'r--');
h3 = plot(x, P1val, 'b');
h4 = plot(x, P2val, 'b--');
hxlabel = xlabel('Cycle');
hylabel = ylabel('Copy Number');

set(gca, ...
    'FontName',     'Helvetica', ...
    'FontSize',     11, ...
    'Box',          'off', ...
    'TickDir',      'out', ...
    'TickLength',   [.02 .02], ...
    'XMinorTick',   'on', ...
    'YMinorTick',   'off', ...
    'YGrid',        'off', ...
    'XColor',       [0 0 0], ...
    'YColor',       [0 0 0], ...
    'LineWidth',    1);
set([hxlabel, hylabel], ...
    'FontName',     'AvantGarde', ...
    'FontSize',     11);
set([h1 h2 h3 h4], ...
    'LineWidth',    1);
```

Appendix 4. Effect of magnetic beads on fluorescence measurements.

To achieve real-time fluorescence measurements in the autoPiLOT assay, fluorescence is read directly on the surface of the magnetic beads. A high concentration of magnetic beads may interfere with this measurement, but removing the DNA from the beads would terminate the reaction. To investigate the optical interference of magnetic beads on fluorescence measurements, the fluorescence of a dumbbell U1 at 50 nM was measured with varying amounts of magnetic beads added to solution. The results, shown in **Figure 43A**, show that there is a steep drop in fluorescent signal as the concentration of magnetic beads increases. To determine whether this drop affects the sensitivity of the measurements, fluorescence vs dumbbell concentration curves were created both with and without magnetic beads in solution. The fluorescence curves, shown in **Figure 43B**, have nearly identical slopes, which suggests that while the presence of magnetic beads does decrease fluorescent signal, it does not decrease the resolution with which fluorescent DNA can be detected. 0.50 mg/mL was selected as the magnetic bead concentration for optical measurements in the autoPiLOT. Subsequent results which show fluorescence measurements directly on the surface of the beads are shown in Chapter 4.

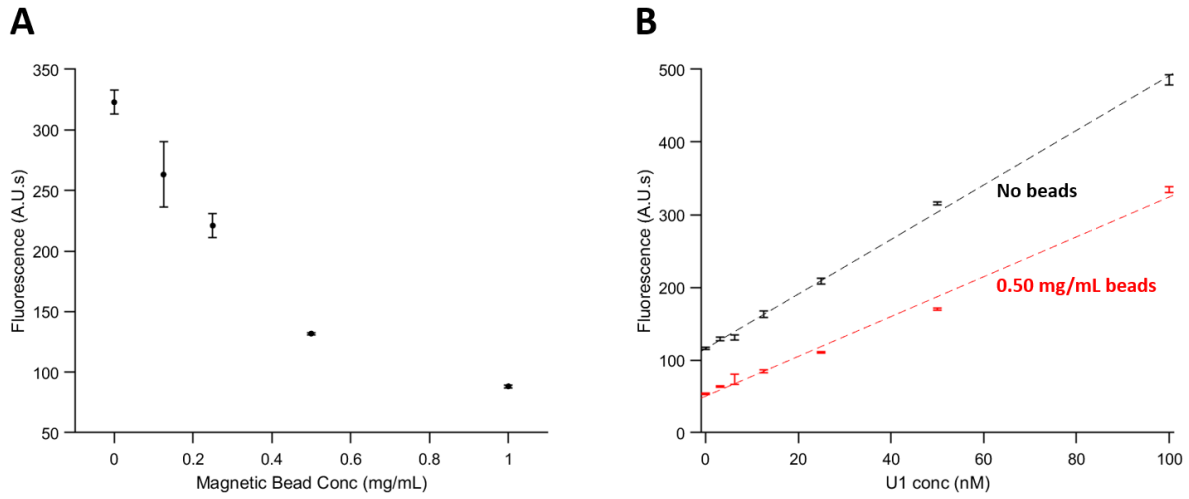

Figure 43. The effect of magnetic beads on fluorescence measurements. **A.** The fluorescence of U1 at 50 nM was measured with varying amounts of magnetic beads added to solution. **B.** Fluorescence curves for U1 ranging from 0-100 nM, both with (red) and without (black) magnetic beads included at 0.5 mg/mL. Error bars depict the mean of three trials ± one standard deviation.

Appendix 5. The effect of NaOH on DNA melt temperature

There is a well-documented decrease in DNA melt temperature caused by sufficiently high or low pH levels.[147, 148] To study the potential application of pH-induced melting to endpoint detection of DNA hybridized to magnetic beads, melt temperatures were determined for several pH values using NaOH as an alkaline agent. If the melt temperature can be reduced to room temperature or lower, then dsDNA should spontaneously dissociate upon introduction of the basic solution. Melt curves were created for fluorescently-labeled pf84 DNA (see **Table 1**), in which one strand was labeled with a 5' fluorophore and the complementary strand was labeled with a 3' quencher molecule. Solutions containing no NaOH, as well as NaOH at pH levels 7.3, 8.3, 9.3, 10.3, 11.3, and 12 were tested (partially shown in **Figure 44A**).

It is well-known that fluorescence is sensitive to changes in pH; this resulted in different fluorescence levels between samples. It is the change of fluorescence with temperature, however, that is used to calculate the melt temperature, so the effects of pH on fluorescence did not need to be taken into account. The results show that, compared to the baseline melt temperature in buffer without NaOH, the presence of NaOH always lowered the melt temperature. At pH 12, the DNA did not exist in the double-stranded state at any temperature above room temperature, indicating that this pH is sufficient to melt DNA at room temperature. The effect of NaOH on melting temperature is shown in **Figure 44B**.

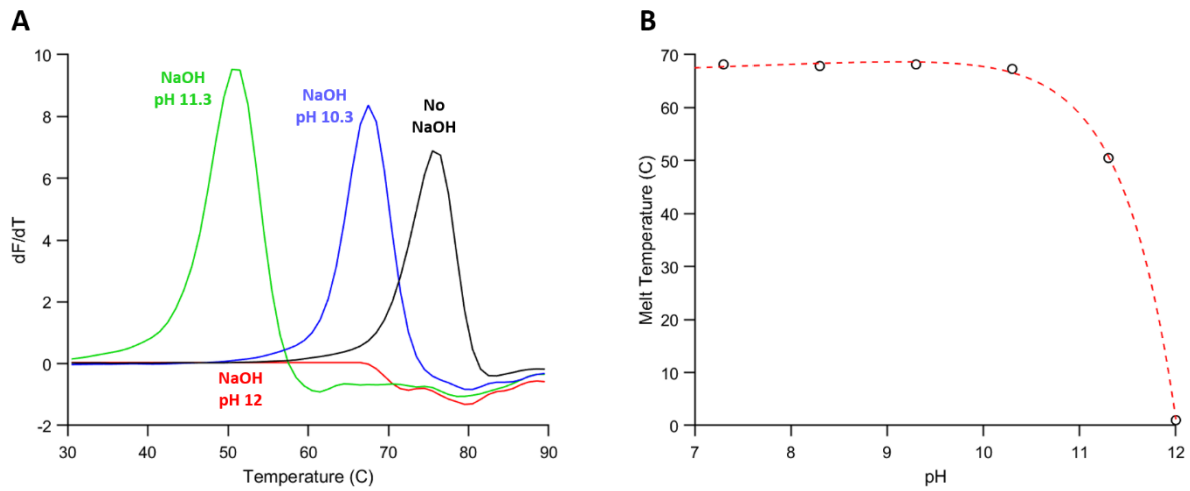

Figure 44. A. Melt curves for fluorescently-labeled pf84 DNA in several different buffer conditions. 5X SSC buffer is shown in black, and solutions containing varying amounts of added NaOH are shown in blue, green, and red. At pH 12, the DNA did not hybridize at any temperature, and thus no melt was observed. **B.** Plot of the calculated melt temperatures for pf84 DNA in buffers of pH 7.3, 8.3, 9.3, 10.3, 11.3, and 12. Note that the melt temperature for pH 12 was arbitrarily plotted at 0 °C to show that the DNA did not hybridize at any temperature tested.

Appendix 6. Endpoint removal of DNA from magnetic beads

There may be applications in which real-time fluorescence measurements are not required, or when the dumbbells bound to the beads must be removed for downstream use. In these situations, a convenient method to remove the dumbbells from the beads would be desired. Perhaps the most straightforward method would be to raise the temperature high enough to melt the DNA, removing all but the biotinylated capture sequence from the beads. This method, however, necessitates equipment to heat the reaction, adding additional components to the autoPiLOT. Alternatively, buffer conditions could be altered such that the DNA melts at room temperature. This can be achieved by raising the pH using NaOH. Finally, a third strategy to remove the dumbbells is via a targeted toehold-mediated strand displacement (TMSD) reaction, as shown in **Figure 45**. This strategy has the advantage of requiring no additional chemical reagents or equipment; a single oligonucleotide can be designed to separate the initial dumbbell U1* from the target DNA. To demonstrate this, a modified version of U1* was created with a 5' toehold region on U1-a* adjacent to the target-binding domain. This sequence, called U1-a* tag, binds to the sequence U1* removal at the exposed toehold. TMSD then proceeds to displace the target from U1* tag, effectively separating the dumbbell network from the magnetic bead.

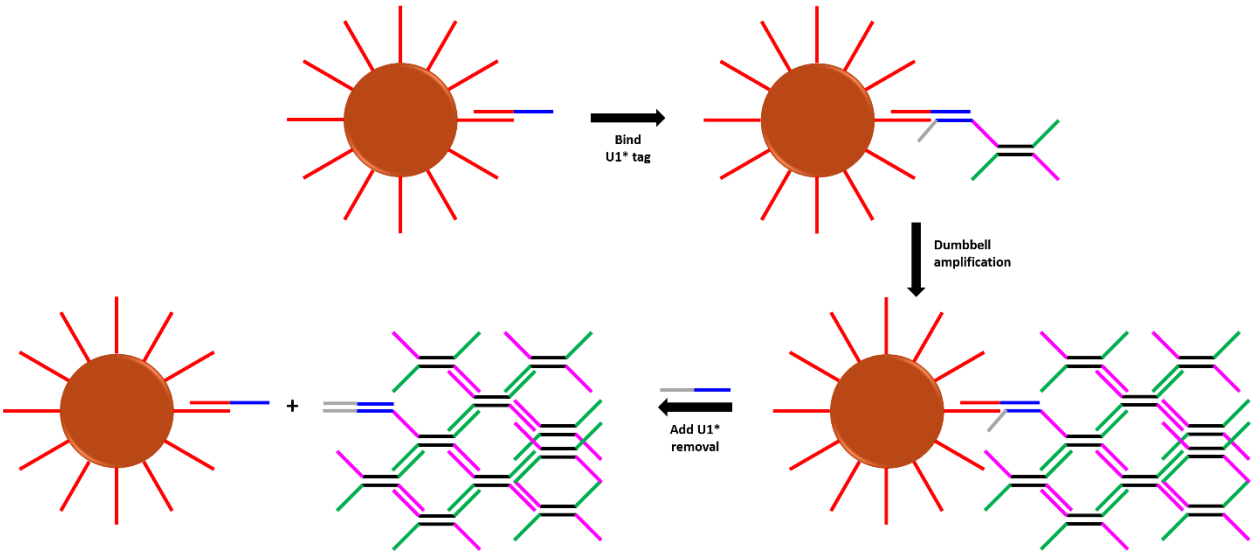

Figure 45. Overview of the TMSD strategy to remove the dumbbells from the magnetic beads. The dumbbell U1* is replaced with a modified version, U1* tag, which has an exposed toehold region (shown in grey). The addition of U1* removal initiates TMSD and displaces the target sequence from U1* tag.

All three of the previously mentioned strategies – increased temperature, increased pH, and TMSD – were tested on beads maximally loaded with fluorescently-labeled U1* (or U1* tag for the TMSD test). The beads were incubated in an excess of target, followed by an excess of U1* to load them with fluorescent DNA. They were then washed and subjected to either 95 °C heat, NaOH at pH 12, or the U1* removal oligonucleotide at a concentration of 1 µM. As a control, some beads were also simply resuspended in hybridization buffer. The beads were then magnetically separated and the fluorescence of the supernatant was measured. These results are shown in **Figure 46**. Each method removed approximately equal amounts of DNA from the beads, and no statistical significance was found in the differences between findings. Melting DNA at 95 °C could be called the gold standard method; PCR protocols regularly use this temperature to ensure that all DNA is melted. Therefore, the results shown in **Figure 46** suggest that DNA separation via high pH and TMSD reaction are both highly effective methods for endpoint detection of DNA dumbbells.

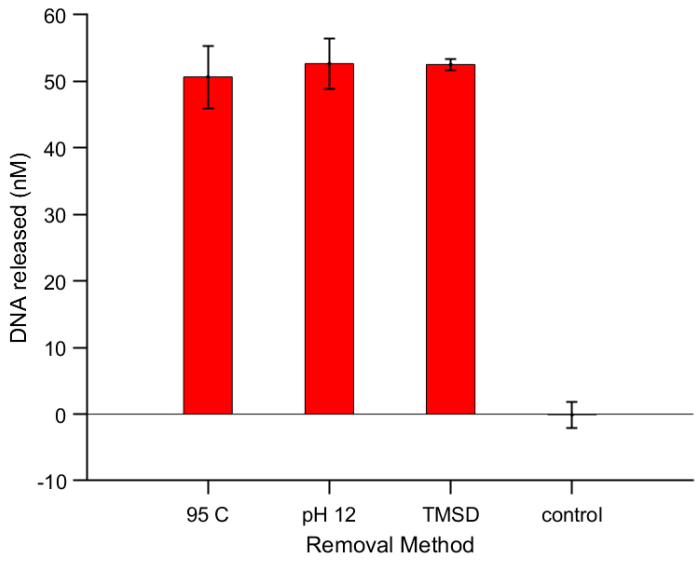

Figure 46. Three different DNA removal methods were tested to separate fluorescent DNA from magnetic beads. Fluorescence measurements were converted to DNA concentration values using fluorescence calibration curves. Error bars depict the mean of three trials ± one standard deviation.

Appendix 7. Optimization of bead blocking steps

There are two means by which non-specific amplification may occur: accumulation on the surface of the magnetic beads, and via fluid carryover between chambers. Even if the non-specific accumulation on the beads is reduced to zero, there will always be some level of fluid transfer between chambers, and therefore some level of non-specific signal amplification.[68] During autoPiLOT amplification, the magnetic beads are cyclically transferred between the two dumbbell chambers many times. Therefore, it is important to minimize both the non-specific binding of DNA by the beads and the non-specific amplification via fluid transfer. To this end, three different bead blocking agents were investigated: bovine serum albumin (BSA), salmon sperm DNA, and biotin. BSA is commonly used as a blocking agent in Western blots and ELISA assays. Single-stranded salmon sperm DNA is essentially random, with DNA fragments of varying sizes. Biotin binds very strongly to the streptavidin-coated surface of the magnetic beads; it is biotin that anchors the capture probe to the magnetic bead surface. All three of these blocking agents are thought to bind to available surfaces on the beads, decreasing subsequent non-specific binding of DNA dumbbells.

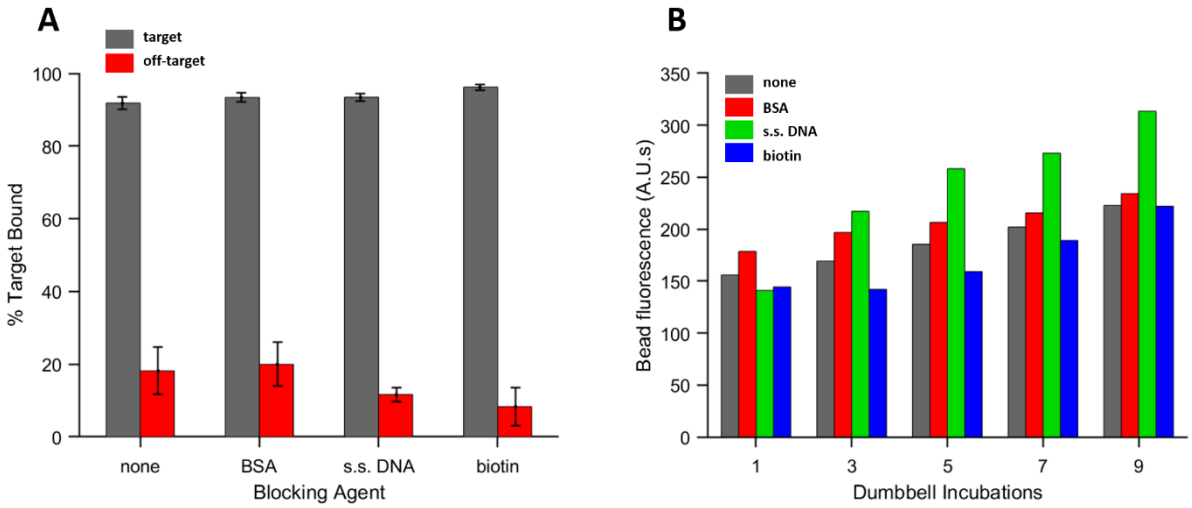

Figure 47. Comparison of different bead blocking protocols on non-specific binding and non-specific amplification. **A.** Target binding (grey) and non-specific DNA binding (red) for beads with different blocking agents. **B.** Each type of bead was used for autoPiLOT assays without any target DNA. The resulting fluorescence represents the non-specific signal amplification.

Magnetic beads were functionalized using each of these different blocking agents, as well as without any blocking. Each type of bead was then incubated in fluorescent target DNA. The fluorescence of this solution was measured before and after incubations to determine the fraction of DNA bound by the beads. This was repeated using a different fluorescent DNA sequence, previously published as a malaria PCR primer,[69] to measure off-target binding. The results are shown in **Figure 47A**. Biotin blocking produced the lowest average amount of off-target binding, although it was only significantly lower than that of BSA blocking (two-way t-test, $p < 0.1$). Each type of bead was also transported back and forth between dumbbells U1 and U2, to determine whether blocking method impacted the rate of non-specific amplification. The beads were loaded into the autoPiLOT reaction processor, and fluorescence was measured after every other incubation. The results in **Figure 47B** show the accumulation of dumbbells over time on the beads. The results were very similar for unblocked, BSA-blocked, and biotin-blocked beads. Only those blocked with salmon sperm DNA appeared to exhibit significantly higher non-specific amplification. In clinical applications, the blocking protocol likely needs to be tailored to the sample type. For the studies performed in Chapter 4, based on the results of **Figure 47**, biotin blocking was selected as the best protocol.

Appendix 8. Effect of dumbbell incubation time on amplification

The authors who first demonstrated the dumbbell amplification assay used 30-minute incubation times for each dumbbell. Based on this previous report, 30 minutes was used as the incubation time for autoPiLOT experiments. The hands-free nature of the autoPiLOT makes 30-minute incubations no more cumbersome than 1-minute incubations. In situations where time is a more serious constraint, however, there may be a desire for a shorter reaction timeframe. To investigate the effect of shortening the incubation time, the autoPiLOT assay was performed with incubation times of 30, 10, and 1 minutes per dumbbell. A total of 15 incubations between U1 and U2 were performed, and samples contained $3*10^8$ copies of target DNA. Decreasing the incubation time led to decreases in both D-DNA and L-DNA amplification, as shown in **Figure 48**. The ratio of these two signals, or signal-to-noise ratio, decreased with shortening incubation times. Increasing the incubation time, say from 1 to 10 minutes, increases the target-induced amplification more than it does the amount of non-specific L-DNA amplification.

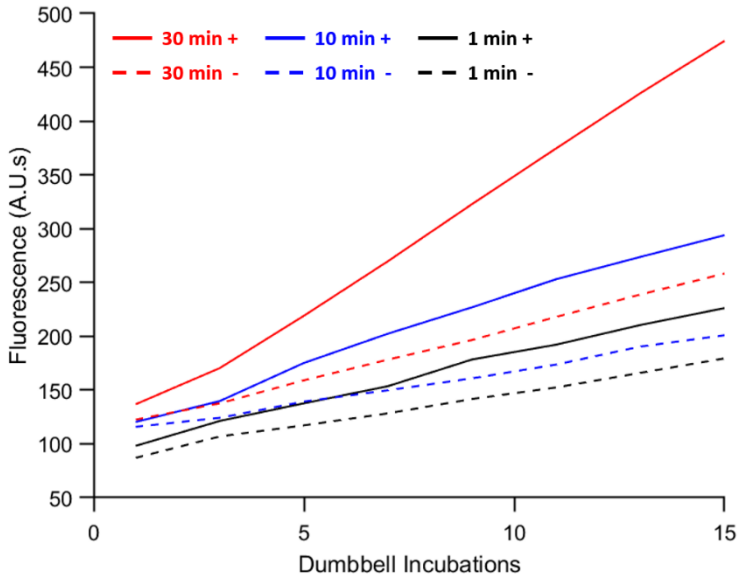

Figure 48. AutoPiLOT amplification trials using 30-minute (red), 10-minute (blue), and 1-minute (black) dumbbell amplification times. Solid lines show D-DNA signal, and dashed lines show L-DNA signal. Displayed values are the mean of three trials.

REFERENCES

1. Xu, G.; Zhao, H.; Reboud, J.; Cooper, J. M., Cycling of Rational Hybridization Chain Reaction To Enable Enzyme-Free DNA-Based Clinical Diagnosis. *ACS nano* **2018,** *12* (7), 7213-7219.
2. Lai, Y.-S.; Biedermann, P.; Ekpo, U. F.; Garba, A.; Mathieu, E.; Midzi, N.; Mwinzi, P.; N'Goran, E. K.; Raso, G.; Assaré, R. K., Spatial distribution of schistosomiasis and treatment needs in sub-Saharan Africa: a systematic review and geostatistical analysis. *The Lancet infectious diseases* **2015,** *15* (8), 927-940.
3. Steinmann, P.; Keiser, J.; Bos, R.; Tanner, M.; Utzinger, J., Schistosomiasis and water resources development: systematic review, meta-analysis, and estimates of people at risk. *The Lancet infectious diseases* **2006,** *6* (7), 411-425.
4. Hotez, P. J.; Brindley, P. J.; Bethony, J. M.; King, C. H.; Pearce, E. J.; Jacobson, J., Helminth infections: the great neglected tropical diseases. *The Journal of clinical investigation* **2008,** *118* (4), 1311-1321.
5. Colley, D. G.; Bustinduy, A. L.; Secor, W. E.; King, C. H., Human schistosomiasis. *The Lancet* **2014,** *383* (9936), 2253-2264.
6. Khatami, A.; Bahadory, S.; Ghorbani, S.; Saadati, H.; Zarei, M.; Soleimani, A.; Zibaei, M., Two rivals or colleagues in the liver? Hepatit B virus and Schistosoma mansoni co-infections: A systematic review and meta-analysis. *Microbial Pathogenesis* **2021**, 104828.
7. Chuah, C.; Gobert, G. N.; Latif, B.; Heo, C. C.; Leow, C. Y., Schistosomiasis in Malaysia: A review. *Acta tropica* **2019,** *190*, 137-143.
8. Andrade, G.; Bertsch, D. J.; Gazzinelli, A.; King, C. H., Decline in infection-related morbidities following drug-mediated reductions in the intensity of Schistosoma infection: A systematic review and meta-analysis. *PLoS neglected tropical diseases* **2017,** *11* (2), e0005372.
9. Gryseels, B.; Polman, K.; Clerinx, J.; Kestens, L., Human schistosomiasis. *The Lancet* **2006,** *368* (9541), 1106-1118.
10. Bottieau, E.; Clerinx, J.; De Vega, M. R.; Van den Enden, E.; Colebunders, R.; Van Esbroeck, M.; Vervoort, T.; Van Gompel, A.; Van den Ende, J., Imported Katayama fever: clinical and biological features at presentation and during treatment. *Journal of Infection* **2006,** *52* (5), 339-345.
11. Meltzer, E.; Artom, G.; Marva, E.; Assous, M. V.; Rahav, G.; Schwartz, E., Schistosomiasis among travelers: new aspects of an old disease. *Emerging infectious diseases* **2006,** *12* (11), 1696.
12. Nicolls, D. J.; Weld, L. H.; Schwartz, E.; Reed, C.; Von Sonnenburg, F.; Freedman, D. O.; Kozarsky, P. E., Characteristics of schistosomiasis in travelers reported to the GeoSentinel Surveillance Network 1997–2008. *The American journal of tropical medicine and hygiene* **2008,** *79* (5), 729-734.
13. Whitty, C. J.; Mabey, D. C.; Armstrong, M.; Wright, S. G.; Chiodini, P. L., Presentation and outcome of 1107 cases of schistosomiasis from Africa diagnosed in a non-endemic country. *Transactions of the Royal Society of Tropical Medicine and Hygiene* **2000,** *94* (5), 531-534.
14. Booth, M.; Vennervald, B.; Kabatereine, N.; Kazibwe, F.; Ouma, J.; Kariuki, C.; Muchiri, E.; Kadzo, H.; Ireri, E.; Kimani, G., Hepatosplenic morbidity in two neighbouring communities in Uganda with high levels of Schistosoma mansoni infection but very different durations of residence. *Transactions of the Royal Society of Tropical Medicine and Hygiene* **2004,** *98* (2), 125-136.
15. Richter, J., The impact of chemotherapy on morbidity due to schistosomiasis. *Acta tropica* **2003,** *86* (2-3), 161-183.
16. Imai, K.; Koibuchi, T.; Kumagai, T.; Maeda, T.; Osada, Y.; Ohta, N.; Koga, M.; Nakamura, H.; Miura, T.; Iwamoto, A., Cerebral schistosomiasis due to Schistosoma haematobium confirmed by PCR analysis of brain specimen. *Journal of clinical microbiology* **2011,** *49* (10), 3703-3706.
17. Christian, P.; Khatry, S. K.; West Jr, K. P., Antenatal anthelmintic treatment, birthweight, and infant survival in rural Nepal. *The Lancet* **2004,** *364* (9438), 981-983.
18. Grimes, J. E.; Croll, D.; Harrison, W. E.; Utzinger, J.; Freeman, M. C.; Templeton, M. R., The relationship between water, sanitation and schistosomiasis: a systematic review and meta-analysis. *PLoS neglected tropical diseases* **2014,** *8* (12), e3296.

19. Famakinde, D. O., Treading the path towards genetic control of snail resistance to schistosome infection. *Tropical medicine and infectious disease* **2018,** *3* (3), 86.
20. Chen, Z.; Wang, W.; Yao, J.; Li, S.; Zhang, X.; Hu, H.; Liu, X.; Luo, B.; Liu, Y.; Xu, H., Toxicity of a molluscicide candidate PPU07 against Oncomelania hupensis (Gredler, 1881) and local fish in field evaluation. *Chemosphere* **2019,** *222*, 56-61.
21. Pereira, L. P. L. A.; Ribeiro, E. C. G.; Brito, M. C. A.; Silveira, D. P. B.; Araruna, F. O. S.; Araruna, F. B.; Leite, J. A. C.; Dias, A. A. S.; Firmo, W. d. C. A.; da Rocha Borges, M. O., Essential oils as molluscicidal agents against schistosomiasis transmitting snails-a review. *Acta tropica* **2020,** *209*, 105489.
22. Organization, W. H., Schistosomiasis: progress report 2001-2011, strategic plan 2012-2020. **2013**.
23. Ismail, M.; Botros, S.; Metwally, A.; William, S.; Farghally, A.; Tao, L.-F.; Day, T. A.; Bennett, J. L., Resistance to praziquantel: direct evidence from Schistosoma mansoni isolated from Egyptian villagers. *The American journal of tropical medicine and hygiene* **1999,** *60* (6), 932-935.
24. William, S.; Botros, S.; Ismail, M.; Farghally, A.; Day, T.; Bennett, J., Praziquantel-induced tegumental damage in vitro is diminished in schistosomes derived from praziquantel-resistant infections. *Parasitology* **2001,** *122* (1), 63-66.
25. Katz, N.; Chaves, A.; Pellegrino, J., A simple device for quantitative stool thick-smear technique in schistosomiasis mansoni. *Rev Inst Med Trop Sao Paulo* **1972,** *14* (6), 397-400.
26. Sarhan, R. M.; Kamel, H. H.; Saad, G. A.; Ahmed, O. A., Evaluation of three extraction methods for molecular detection of Schistosoma mansoni infection in human urine and serum samples. *Journal of parasitic diseases* **2015,** *39* (3), 499-507.
27. Coulibaly, J. T.; Knopp, S.; N'Guessan, N. A.; Silué, K. D.; Fürst, T.; Lohourignon, L. K.; Brou, J. K.; N'Gbesso, Y. K.; Vounatsou, P.; N'Goran, E. K., Accuracy of urine circulating cathodic antigen (CCA) test for Schistosoma mansoni diagnosis in different settings of Côte d'Ivoire. *PLoS neglected tropical diseases* **2011,** *5* (11), e1384.
28. Enk, M. J.; e Silva, G. O.; Rodrigues, N. B., Diagnostic accuracy and applicability of a PCR system for the detection of Schistosoma mansoni DNA in human urine samples from an endemic area. *PloS one* **2012,** *7* (6), e38947.
29. Kinkel, H.-F.; Dittrich, S.; Bäumer, B.; Weitzel, T., Evaluation of eight serological tests for diagnosis of imported schistosomiasis. *Clinical and Vaccine Immunology* **2012,** *19* (6), 948-953.
30. Musso, D.; Roche, C.; Nhan, T.-X.; Robin, E.; Teissier, A.; Cao-Lormeau, V.-M., Detection of Zika virus in saliva. *Journal of Clinical Virology* **2015,** *68*, 53-55.
31. Yao, Q.; Wang, Y.; Wang, J.; Chen, S.; Liu, H.; Jiang, Z.; Zhang, X.; Liu, S.; Yuan, Q.; Zhou, X., An Ultrasensitive Diagnostic Biochip Based on Biomimetic Periodic Nanostructure-Assisted Rolling Circle Amplification. *ACS nano* **2018,** *12* (7), 6777-6783.
32. Vallejo, A. F.; Martínez, N. L.; González, I. J.; Arévalo-Herrera, M.; Herrera, S., Evaluation of the loop mediated isothermal DNA amplification (LAMP) kit for malaria diagnosis in P. vivax endemic settings of Colombia. *PLoS neglected tropical diseases* **2015,** *9* (1), e3453.
33. Watanabe, M.; Kawaguchi, T.; Isa, S.-i.; Ando, M.; Tamiya, A.; Kubo, A.; Saka, H.; Takeo, S.; Adachi, H.; Tagawa, T., Ultra-sensitive detection of the pretreatment EGFR T790M Mutation in non–small cell lung cancer patients with an EGFR-activating mutation using droplet digital PCR. *Clinical Cancer Research* **2015,** *21* (15), 3552-3560.
34. Karami, A.; Hasani, M.; Jalilian, F. A.; Ezati, R., Conventional PCR assisted single-component assembly of spherical nucleic acids for simple colorimetric detection of SARS-CoV-2. *Sensors and Actuators B: Chemical* **2021,** *328*, 128971.
35. Klotz, M.; Opper, S.; Heeg, K.; Zimmermann, S., Detection of Staphylococcus aureus enterotoxins A to D by real-time fluorescence PCR assay. *Journal of Clinical Microbiology* **2003,** *41* (10), 4683-4687.
36. Satokari, R. M.; Vaughan, E. E.; Akkermans, A. D.; Saarela, M.; de Vos, W. M., Bifidobacterial diversity in human feces detected by genus-specific PCR and denaturing gradient gel electrophoresis. *Applied and Environmental Microbiology* **2001,** *67* (2), 504-513.

37. Yun, W.; Jiang, J.; Cai, D.; Zhao, P.; Liao, J.; Sang, G., Ultrasensitive visual detection of DNA with tunable dynamic range by using unmodified gold nanoparticles and target catalyzed hairpin assembly amplification. *Biosensors and Bioelectronics* **2016,** *77*, 421-427.
38. Chandrasekaran, A. R.; Punnoose, J. A.; Zhou, L.; Dey, P.; Dey, B. K.; Halvorsen, K., DNA nanotechnology approaches for microRNA detection and diagnosis. *Nucleic acids research* **2019**.
39. George, A. K.; Singh, H., Enzyme-Free scalable DNA digital design Techniques: A review. *IEEE transactions on nanobioscience* **2016,** *15* (8), 928-938.
40. Abolhasan, R.; Mehdizadeh, A.; Rashidi, M. R.; Aghebati-Maleki, L.; Yousefi, M., Application of hairpin DNA-based biosensors with various signal amplification strategies in clinical diagnosis. *Biosensors and Bioelectronics* **2019,** *129*, 164-174.
41. Yin, P.; Choi, H. M.; Calvert, C. R.; Pierce, N. A., Programming biomolecular self-assembly pathways. *Nature* **2008,** *451* (7176), 318.
42. Li, B.; Ellington, A. D.; Chen, X., Rational, modular adaptation of enzyme-free DNA circuits to multiple detection methods. *Nucleic acids research* **2011,** *39* (16), e110-e110.
43. Wei, Y.; Zhou, W.; Li, X.; Chai, Y.; Yuan, R.; Xiang, Y., Coupling hybridization chain reaction with catalytic hairpin assembly enables non-enzymatic and sensitive fluorescent detection of microRNA cancer biomarkers. *Biosensors and Bioelectronics* **2016,** *77*, 416-420.
44. Yin, F.; Liu, H.; Li, Q.; Gao, X.; Yin, Y.; Liu, D., Trace microRNA quantification by means of plasmon-enhanced hybridization chain reaction. *Analytical chemistry* **2016,** *88* (9), 4600-4604.
45. Tang, S.; Gu, Y.; Lu, H.; Dong, H.; Zhang, K.; Dai, W.; Meng, X.; Yang, F.; Zhang, X., Highly-sensitive microRNA detection based on bio-bar-code assay and catalytic hairpin assembly two-stage amplification. *Analytica chimica acta* **2018,** *1004*, 1-9.
46. Chen, X.; Briggs, N.; McLain, J. R.; Ellington, A. D., Stacking nonenzymatic circuits for high signal gain. *Proceedings of the National Academy of Sciences* **2013,** *110* (14), 5386-5391.
47. Jiang, Y. S.; Bhadra, S.; Li, B.; Ellington, A. D., Mismatches Improve the Performance of Strand-Displacement Nucleic Acid Circuits. *Angewandte Chemie International Edition* **2014,** *53* (7), 1845-1848.
48. Jung, C.; Ellington, A. D., Diagnostic applications of nucleic acid circuits. *Accounts of chemical research* **2014,** *47* (6), 1825-1835.
49. Liu, L.; Liu, J.-W.; Wu, H.; Wang, X.-N.; Yu, R.-Q.; Jiang, J.-H., Branched hybridization chain reaction circuit for ultrasensitive localizable imaging of mRNA in living cells. *Analytical chemistry* **2018,** *90* (3), 1502-1505.
50. Bi, S.; Chen, M.; Jia, X.; Dong, Y.; Wang, Z., Hyperbranched hybridization chain reaction for triggered signal amplification and concatenated logic circuits. *Angewandte Chemie International Edition* **2015,** *54* (28), 8144-8148.
51. Xuan, F.; Hsing, I.-M., Triggering hairpin-free chain-branching growth of fluorescent DNA dendrimers for nonlinear hybridization chain reaction. *Journal of the American Chemical Society* **2014,** *136* (28), 9810-9813.
52. Das, S.; Peck, R. B.; Barney, R.; Jang, I. K.; Kahn, M.; Zhu, M.; Domingo, G. J., Performance of an ultra-sensitive Plasmodium falciparum HRP2-based rapid diagnostic test with recombinant HRP2, culture parasites, and archived whole blood samples. *Malaria journal* **2018,** *17* (1), 1-7.
53. Oliveira, W. J.; Magalhães, F. d. C.; Elias, A. M. S.; de Castro, V. N.; Favero, V.; Lindholz, C. G.; Oliveira, Á. A.; Barbosa, F. S.; Gil, F.; Gomes, M. A., Evaluation of diagnostic methods for the detection of intestinal schistosomiasis in endemic areas with low parasite loads: Saline gradient, Helmintex, Kato-Katz and rapid urine test. *PLoS neglected tropical diseases* **2018,** *12* (2), e0006232.
54. Acharya, K. R.; Dhand, N. K.; Whittington, R. J.; Plain, K. M., PCR inhibition of a quantitative PCR for detection of Mycobacterium avium subspecies Paratuberculosis DNA in feces: diagnostic implications and potential solutions. *Frontiers in microbiology* **2017,** *8*, 115.
55. Kenny, A.; Jiménez-Mateos, E. M.; Zea-Sevilla, M. A.; Rábano, A.; Gili-Manzanaro, P.; Prehn, J. H.; Henshall, D. C.; Ávila, J.; Engel, T.; Hernández, F., Proteins and microRNAs are differentially expressed in tear fluid from patients with Alzheimer's disease. *Scientific reports* **2019,** *9* (1), 1-14.

56. Xu, J.; Xu, L.; Yang, B.; Wang, L.; Lin, X.; Tu, H., Assessing methylation status of PAX1 in cervical scrapings, as a novel diagnostic and predictive biomarker, was closely related to screen cervical cancer. *International journal of clinical and experimental pathology* **2015,** *8* (2), 1674.
57. Ho, J.; Marks, G.; Fox, G., The impact of sputum quality on tuberculosis diagnosis: a systematic review. *The International Journal of Tuberculosis and Lung Disease* **2015,** *19* (5), 537-544.
58. Huggett, J.; Green, C.; Zumla, A., Nucleic acid detection and quantification in the developing world. Portland Press Limited: 2009.
59. Huang, J.; Wu, Y.; Chen, Y.; Zhu, Z.; Yang, X.; Yang, C. J.; Wang, K.; Tan, W., Pyrene-excimer probes based on the hybridization chain reaction for the detection of nucleic acids in complex biological fluids. *Angewandte Chemie International Edition* **2011,** *50* (2), 401-404.
60. Urata, H.; Ogura, E.; Shinohara, K.; Ueda, Y.; Akagi, M., Synthesis and properties of mirror-image DNA. *Nucleic acids research* **1992,** *20* (13), 3325-3332.
61. Hauser, N. C.; Martinez, R.; Jacob, A.; Rupp, S.; Hoheisel, J. D.; Matysiak, S., Utilising the left-helical conformation of L-DNA for analysing different marker types on a single universal microarray platform. *Nucleic acids research* **2006,** *34* (18), 5101-5111.
62. Young, B. E.; Kundu, N.; Sczepanski, J. T., Mirror-Image Oligonucleotides: History and Emerging Applications. *Chemistry–A European Journal* **2019**.
63. Purschke, W. G.; Radtke, F.; Kleinjung, F.; Klussmann, S., A DNA Spiegelmer to staphylococcal enterotoxin B. *Nucleic acids research* **2003,** *31* (12), 3027-3032.
64. Hayashi, G.; Hagihara, M.; Nakatani, K. In *Application of L-DNA as a molecular tag*, Nucleic Acids Symposium Series, Oxford University Press: 2005; pp 261-262.
65. Ke, G.; Wang, C.; Ge, Y.; Zheng, N.; Zhu, Z.; Yang, C. J., L-DNA molecular beacon: a safe, stable, and accurate intracellular nano-thermometer for temperature sensing in living cells. *Journal of the American Chemical Society* **2012,** *134* (46), 18908-18911.
66. Adams, N. M.; Gabella, W. E.; Hardcastle, A. N.; Haselton, F. R., Adaptive PCR Based on Hybridization Sensing of Mirror-Image l-DNA. *Analytical chemistry* **2017,** *89* (1), 728-735.
67. Bordelon, H.; Adams, N. M.; Klemm, A. S.; Russ, P. K.; Williams, J. V.; Talbot, H. K.; Wright, D. W.; Haselton, F. R., Development of a low-resource RNA extraction cassette based on surface tension valves. *ACS applied materials & interfaces* **2011,** *3* (6), 2161-2168.
68. Adams, N. M.; Creecy, A. E.; Majors, C. E.; Wariso, B. A.; Short, P. A.; Wright, D. W.; Haselton, F. R., Design criteria for developing low-resource magnetic bead assays using surface tension valves. *Biomicrofluidics* **2013,** *7* (1), 014104.
69. Bitting, A. L.; Bordelon, H.; Baglia, M. L.; Davis, K. M.; Creecy, A. E.; Short, P. A.; Albert, L. E.; Karhade, A. V.; Wright, D. W.; Haselton, F. R., Automated device for asynchronous extraction of RNA, DNA, or protein biomarkers from surrogate patient samples. *Journal of laboratory automation* **2016,** *21* (6), 732-742.
70. Scherr, T. F.; Ryskoski, H. B.; Doyle, A. B.; Haselton, F. R., A two-magnet strategy for improved mixing and capture from biofluids. *Biomicrofluidics* **2016,** *10* (2), 024118.
71. Umansky, S. R.; Tomei, L. D., Transrenal DNA testing: progress and perspectives. *Expert review of molecular diagnostics* **2006,** *6* (2), 153-163.
72. Chen, C.; Chen, C.; Sadeghi, M., Evaluation of cell-free DNA accuracy as diagnostic biomarker for prostate cancer: A systematic review and meta-analysis. *Biotechnology and Applied Biochemistry* **2021**.
73. Palomaki, G. E.; Chiu, R. W.; Pertile, M. D.; Sistermans, E. A.; Yaron, Y.; Vermeesch, J. R.; Vora, N. L.; Best, R. G.; Wilkins-Haug, L., International Society for Prenatal Diagnosis Position Statement: cell free (cf) DNA screening for Down syndrome in multiple pregnancies. *Prenatal Diagnosis* **2020**.
74. Hussein, H. M.; El-Tonsy, M. M.; Tawfik, R. A.; Ahmed, S. A.-E.-G., Experimental study for early diagnosis of prepatent schistosomiasis mansoni by detection of free circulating DNA in serum. *Parasitology research* **2012,** *111* (1), 475-478.
75. Green, C.; Huggett, J. F.; Talbot, E.; Mwaba, P.; Reither, K.; Zumla, A. I., Rapid diagnosis of tuberculosis through the detection of mycobacterial DNA in urine by nucleic acid amplification methods. *The Lancet infectious diseases* **2009,** *9* (8), 505-511.

76. Putaporntip, C.; Buppan, P.; Jongwutiwes, S., Improved performance with saliva and urine as alternative DNA sources for malaria diagnosis by mitochondrial DNA-based PCR assays. *Clinical Microbiology and Infection* **2011,** *17* (10), 1484-1491.
77. Krolewiecki, A. J.; Koukounari, A.; Romano, M.; Caro, N. N.; Scott, A. L.; Fleitas, P.; Cimino, R.; Shiff, C. J., Transrenal DNA-based diagnosis of Strongyloides stercoralis (Grassi, 1879) infection: Bayesian latent class modeling of test accuracy. *PLoS neglected tropical diseases* **2018,** *12* (6), e0006550.
78. Pillay, P.; Taylor, M.; Zulu, S. G.; Gundersen, S. G.; Verweij, J. J.; Hoekstra, P.; Brienen, E. A.; Kleppa, E.; Kjetland, E. F.; van Lieshout, L., Real-time polymerase chain reaction for detection of Schistosoma DNA in small-volume urine samples reflects focal distribution of urogenital Schistosomiasis in primary school girls in KwaZulu Natal, South Africa. *The American journal of tropical medicine and hygiene* **2014,** *90* (3), 546-552.
79. Hamburger, J.; Turetski, T.; Kapeller, I.; Deresiewicz, R., Highly repeated short DNA sequences in the genome of Schistosoma mansoni recognized by a species-specific probe. *Molecular and biochemical parasitology* **1991,** *44* (1), 73-80.
80. Wichmann, D.; Panning, M.; Quack, T.; Kramme, S.; Burchard, G.-D.; Grevelding, C.; Drosten, C., Diagnosing schistosomiasis by detection of cell-free parasite DNA in human plasma. *PLoS neglected tropical diseases* **2009,** *3* (4), e422.
81. Sandoval, N.; Siles-Lucas, M.; Perez-Arellano, J.; Carranza, C.; Puente, S.; Lopez-Aban, J.; Muro, A., A new PCR-based approach for the specific amplification of DNA from different Schistosoma species applicable to human urine samples. *Parasitology* **2006,** *133* (5), 581-587.
82. Armoo, S.; Cunningham, L. J.; Campbell, S. J.; Aboagye, F. T.; Boampong, F. K.; Hamidu, B. A.; Osei-Atweneboana, M. Y.; Stothard, J. R.; Adams, E. R., Detecting Schistosoma mansoni infections among pre-school-aged children in southern Ghana: a diagnostic comparison of urine-CCA, real-time PCR and Kato-Katz assays. *BMC infectious diseases* **2020,** *20* (1), 1-10.
83. Burnham, P.; Dadhania, D.; Heyang, M.; Chen, F.; Westblade, L. F.; Suthanthiran, M.; Lee, J. R.; De Vlaminck, I., Urinary cell-free DNA is a versatile analyte for monitoring infections of the urinary tract. *Nature communications* **2018,** *9* (1), 2412.
84. Enk, M. J.; e Silva, G. O.; Rodrigues, N. B., A salting out and resin procedure for extracting Schistosoma mansoni DNA from human urine samples. *BMC research notes* **2010,** *3* (1), 115.
85. Bordelon, H.; Russ, P. K.; Wright, D. W.; Haselton, F. R., A magnetic bead-based method for concentrating DNA from human urine for downstream detection. *PloS one* **2013,** *8* (7), e68369.
86. Adams, N. M.; Bordelon, H.; Wang, K.-K. A.; Albert, L. E.; Wright, D. W.; Haselton, F. R., Comparison of three magnetic bead surface functionalities for RNA extraction and detection. *ACS applied materials & interfaces* **2015,** *7* (11), 6062-6069.
87. Livak, K. J.; Flood, S.; Marmaro, J.; Giusti, W.; Deetz, K., Oligonucleotides with fluorescent dyes at opposite ends provide a quenched probe system useful for detecting PCR product and nucleic acid hybridization. *Genome Research* **1995,** *4* (6), 357-362.
88. Cardullo, R. A.; Agrawal, S.; Flores, C.; Zamecnik, P. C.; Wolf, D. E., Detection of nucleic acid hybridization by nonradiative fluorescence resonance energy transfer. *Proceedings of the National Academy of Sciences* **1988,** *85* (23), 8790-8794.
89. Qiu, X.; Guo, J.; Jin, Z.; Petreto, A.; Medintz, I. L.; Hildebrandt, N., Multiplexed Nucleic Acid Hybridization Assays Using Single-FRET-Pair Distance-Tuning. *Small* **2017,** *13* (25), 1700332.
90. Navani, N. K.; Li, Y., Nucleic acid aptamers and enzymes as sensors. *Current opinion in chemical biology* **2006,** *10* (3), 272-281.
91. Juskowiak, B., Nucleic acid-based fluorescent probes and their analytical potential. *Analytical and bioanalytical chemistry* **2011,** *399* (9), 3157-3176.
92. Marras, S. A.; Tyagi, S.; Kramer, F. R., Real-time assays with molecular beacons and other fluorescent nucleic acid hybridization probes. *Clinica Chimica Acta* **2006,** *363* (1-2), 48-60.
93. Qiu, J.; Wilson, A.; El-Sagheer, A. H.; Brown, T., Combination probes with intercalating anchors and proximal fluorophores for DNA and RNA detection. *Nucleic acids research* **2016,** *44* (17), e138-e138.

94. Ogawa, M.; Kosaka, N.; Longmire, M. R.; Urano, Y.; Choyke, P. L.; Kobayashi, H., Fluorophore− quencher based activatable targeted optical probes for detecting in vivo cancer metastases. *Molecular pharmaceutics* **2009,** *6* (2), 386-395.
95. Marras, S. A.; Kramer, F. R.; Tyagi, S., Efficiencies of fluorescence resonance energy transfer and contact-mediated quenching in oligonucleotide probes. *Nucleic acids research* **2002,** *30* (21), e122-e122.
96. Zheng, J.; Yang, R.; Shi, M.; Wu, C.; Fang, X.; Li, Y.; Li, J.; Tan, W., Rationally designed molecular beacons for bioanalytical and biomedical applications. *Chemical Society reviews* **2015,** *44* (10), 3036-3055.
97. Yang, R.; Jin, J.; Chen, Y.; Shao, N.; Kang, H.; Xiao, Z.; Tang, Z.; Wu, Y.; Zhu, Z.; Tan, W., Carbon nanotube-quenched fluorescent oligonucleotides: probes that fluoresce upon hybridization. *Journal of the American Chemical Society* **2008,** *130* (26), 8351-8358.
98. Wang, W.; Chen, C.; Qian, M. X.; Zhao, X. S., Aptamer biosensor for protein detection based on guanine-quenching. *Sensors and Actuators B: Chemical* **2008,** *129* (1), 211-217.
99. Shen, J.; Okamoto, Y., Efficient separation of enantiomers using stereoregular chiral polymers. *Chemical reviews* **2015,** *116* (3), 1094-1138.
100. Pu, L., Simultaneous determination of concentration and enantiomeric composition in fluorescent sensing. *Accounts of chemical research* **2017,** *50* (4), 1032-1040.
101. Anderson, D. J.; Reischer, R. J.; Taylor, A. J.; Wechter, W. J., Preparation and Characterization of Oligonucleotides of D-and L-2'Deoxyuridine. *Nucleosides & nucleotides* **1984,** *3* (5), 499-512.
102. Urata, H.; Shinohara, K.; Ogura, E.; Ueda, Y.; Akagi, M., Mirror-image DNA. *Journal of the American Chemical Society* **1991,** *113* (21), 8174-8175.
103. Lee, A.-Y.; Kim, K.-R.; Yu, J. H.; Ahn, D.-R., L-DNA linear duplex: An efficient drug delivery carrier with a simple structure. *Journal of Industrial and Engineering Chemistry* **2019,** *74*, 187-192.
104. Yatime, L.; Maasch, C.; Hoehlig, K.; Klussmann, S.; Andersen, G. R.; Vater, A., Structural basis for the targeting of complement anaphylatoxin C5a using a mixed L-RNA/L-DNA aptamer. *Nature communications* **2015,** *6*, 6481.
105. Williams, K. P.; Liu, X.-H.; Schumacher, T. N.; Lin, H. Y.; Ausiello, D. A.; Kim, P. S.; Bartel, D. P., Bioactive and nuclease-resistant L-DNA ligand of vasopressin. *Proceedings of the National Academy of Sciences* **1997,** *94* (21), 11285-11290.
106. You, Y.; Tataurov, A. V.; Owczarzy, R., Measuring thermodynamic details of DNA hybridization using fluorescence. *Biopolymers* **2011,** *95* (7), 472-486.
107. Moreira, B. G.; You, Y.; Owczarzy, R., Cy3 and Cy5 dyes attached to oligonucleotide terminus stabilize DNA duplexes: predictive thermodynamic model. *Biophysical chemistry* **2015,** *198*, 36-44.
108. Telser, J.; Cruickshank, K. A.; Morrison, L. E.; Netzel, T. L., Synthesis and characterization of DNA oligomers and duplexes containing covalently attached molecular labels: comparison of biotin, fluorescein, and pyrene labels by thermodynamic and optical spectroscopic measurements. *Journal of the American Chemical Society* **1989,** *111* (18), 6966-6976.
109. Leelawong, M.; Adams, N. M.; Gabella, W. E.; Wright, D. W.; Haselton, F. R., Detection of Single-Nucleotide Polymorphism Markers of Antimalarial Drug Resistance Directly from Whole Blood. *The Journal of Molecular Diagnostics* **2019**.
110. Gudnason, H.; Dufva, M.; Bang, D. D.; Wolff, A., Comparison of multiple DNA dyes for real-time PCR: effects of dye concentration and sequence composition on DNA amplification and melting temperature. *Nucleic acids research* **2007,** *35* (19), e127.
111. Ruijter, J.; Ramakers, C.; Hoogaars, W.; Karlen, Y.; Bakker, O.; Van den Hoff, M.; Moorman, A., Amplification efficiency: linking baseline and bias in the analysis of quantitative PCR data. *Nucleic acids research* **2009,** *37* (6), e45-e45.
112. Genot, A. J.; Bath, J.; Turberfield, A. J., Reversible logic circuits made of DNA. *Journal of the American Chemical Society* **2011,** *133* (50), 20080-20083.
113. Wang, F.; Lv, H.; Li, Q.; Li, J.; Zhang, X.; Shi, J.; Wang, L.; Fan, C., Implementing digital computing with DNA-based switching circuits. *Nature communications* **2020,** *11* (1), 1-8.

114. Venkataraman, S.; Dirks, R. M.; Rothemund, P. W.; Winfree, E.; Pierce, N. A., An autonomous polymerization motor powered by DNA hybridization. *Nature Nanotechnology* **2007,** *2* (8), 490-494.
115. Xiong, E.; Zhen, D.; Jiang, L., Homogeneous enzyme-free and entropy-driven isothermal fluorescent assay for nucleic acids based on a dual-signal output amplification strategy. *Chemical communications* **2018,** *54* (89), 12594-12597.
116. Dirks, R. M.; Pierce, N. A., Triggered amplification by hybridization chain reaction. *Proceedings of the National Academy of Sciences* **2004,** *101* (43), 15275-15278.
117. Dai, J.; He, H.; Duan, Z.; Guo, Y.; Xiao, D., Self-replicating catalyzed hairpin assembly for rapid signal amplification. *Analytical chemistry* **2017,** *89* (22), 11971-11975.
118. SantaLucia, J., A unified view of polymer, dumbbell, and oligonucleotide DNA nearest-neighbor thermodynamics. *Proceedings of the National Academy of Sciences* **1998,** *95* (4), 1460-1465.
119. Peyret, N.; Seneviratne, P. A.; Allawi, H. T.; SantaLucia, J., Nearest-Neighbor Thermodynamics and NMR of DNA Sequences with Internal A⊙ A, C⊙ C, G⊙ G, and T⊙ T Mismatches. *Biochemistry* **1999,** *38* (12), 3468-3477.
120. Allen, P. B.; Arshad, S. A.; Li, B.; Chen, X.; Ellington, A. D., DNA circuits as amplifiers for the detection of nucleic acids on a paperfluidic platform. *Lab on a Chip* **2012,** *12* (16), 2951-2958.
121. Zhang, Z.; Fan, T. W.; Hsing, I.-M., Integrating DNA strand displacement circuitry to the nonlinear hybridization chain reaction. *Nanoscale* **2017,** *9* (8), 2748-2754.
122. Wu, H.; Liu, Y.; Wang, H.; Wu, J.; Zhu, F.; Zou, P., Label-free and enzyme-free colorimetric detection of microRNA by catalyzed hairpin assembly coupled with hybridization chain reaction. *Biosensors and Bioelectronics* **2016,** *81*, 303-308.
123. Liu, S.; Wang, Y.; Ming, J.; Lin, Y.; Cheng, C.; Li, F., Enzyme-free and ultrasensitive electrochemical detection of nucleic acids by target catalyzed hairpin assembly followed with hybridization chain reaction. *Biosensors and Bioelectronics* **2013,** *49*, 472-477.
124. Fang, H.; Xie, N.; Ou, M.; Huang, J.; Li, W.; Wang, Q.; Liu, J.; Yang, X.; Wang, K., Detection of nucleic acids in complex samples via magnetic microbead-assisted catalyzed hairpin assembly and "DD–A" FRET. *Analytical chemistry* **2018,** *90* (12), 7164-7170.
125. Liu, Y.; Shen, T.; Li, J.; Gong, H.; Chen, C.; Chen, X.; Cai, C., Ratiometric fluorescence sensor for the microRNA determination by catalyzed hairpin assembly. *ACS sensors* **2017,** *2* (10), 1430-1434.
126. Shimizu, B.; Asai, M.; Hieda, H.; Miyaki, M.; Okazaki, H., Preparation of L-β-Ribonucleosides and L-β-Ribonucleotides. *Chemical and Pharmaceutical Bulletin* **1965,** *13* (5), 616-618.
127. Klußmann, S.; Nolte, A.; Bald, R.; Erdmann, V. A.; Fürste, J. P., Mirror-image RNA that binds D-adenosine. *Nature biotechnology* **1996,** *14* (9), 1112-1115.
128. Adams, N. M.; Gabella, W. E.; Hardcastle, A. N.; Haselton, F. R., Adaptive PCR Based on Hybridization Sensing of Mirror-Image l-DNA. *Analytical chemistry* **2016,** *89* (1), 728-735.
129. Lee, A.-Y.; Kim, K.-R.; Yu, J. H.; Ahn, D.-R., L-DNA linear duplex: an efficient drug delivery carrier with a simple structure. *Journal of Industrial and Engineering Chemistry* **2019**.
130. Zimmers, Z. A.; Adams, N. M.; Gabella, W. E.; Haselton, F. R., Fluorophore-quencher interactions effect on hybridization characteristics of complementary oligonucleotides. *Analytical Methods* **2019,** *11* (22), 2862-2867.
131. Ji, Q.; Pang, M.; Han, J.; Feng, S.; Zhang, X.; Ma, Y.; Meng, J., A simple and efficient synthesis of 2-deoxy-L-ribose from 2-deoxy-D-ribose. *Synlett* **2006,** *2006* (15), 2498-2500.
132. Shi, Z.-D.; Yang, B.-H.; Wu, Y.-L., A stereospecific synthesis of L-deoxyribose, L-ribose and L-ribosides. *Tetrahedron* **2002,** *58* (16), 3287-3296.
133. Kabza, A. M.; Sczepanski, J. T., l-DNA-Based Catalytic Hairpin Assembly Circuit. *Molecules* **2020,** *25* (4), 947.
134. Armbruster, D. A.; Pry, T., Limit of blank, limit of detection and limit of quantitation. *The clinical biochemist reviews* **2008,** *29* (Suppl 1), S49.
135. Perez, J. W.; Vargis, E. A.; Russ, P. K.; Haselton, F. R.; Wright, D. W., Detection of respiratory syncytial virus using nanoparticle amplified immuno-polymerase chain reaction. *Analytical biochemistry* **2011,** *410* (1), 141-148.

136. Manning, G. S., The molecular theory of polyelectrolyte solutions with applications to the electrostatic properties of polynucleotides. *Quarterly reviews of biophysics* **1978,** *11* (2), 179-246.
137. Egli, M., DNA-cation interactions: quo vadis? *Chemistry & biology* **2002,** *9* (3), 277-286.
138. Chiu, T. K.; Dickerson, R. E., 1 Å crystal structures of B-DNA reveal sequence-specific binding and groove-specific bending of DNA by magnesium and calcium. *Journal of molecular biology* **2000,** *301* (4), 915-945.
139. Fan, Z.; Yao, B.; Ding, Y.; Zhao, J.; Xie, M.; Zhang, K., Entropy-driven amplified electrochemiluminescence biosensor for RdRp gene of SARS-CoV-2 detection with self-assembled DNA tetrahedron scaffolds. *Biosensors and Bioelectronics* **2021,** *178*, 113015.
140. Zimmers, Z. A.; Adams, N. M.; Haselton, F. R., Addition of mirror-image L-DNA elements to DNA amplification circuits to distinguish leakage from target signal. *Biosensors and Bioelectronics* **2021,** *188*, 113354.
141. Creecy, A.; Russ, P. K.; Solinas, F.; Wright, D. W.; Haselton, F. R., Tuberculosis biomarker extraction and isothermal amplification in an integrated diagnostic device. *PloS one* **2015,** *10* (7), e0130260.
142. Russ, P. K.; Karhade, A. V.; Bitting, A. L.; Doyle, A.; Solinas, F.; Wright, D. W.; Haselton, F. R., A Prototype Biomarker Detector Combining Biomarker Extraction and Fixed Temperature PCR. *Journal of laboratory automation* **2016,** *21* (4), 590-598.
143. Knowlton, S.; Joshi, A.; Syrrist, P.; Coskun, A. F.; Tasoglu, S., 3D-printed smartphone-based point of care tool for fluorescence-and magnetophoresis-based cytometry. *Lab on a Chip* **2017,** *17* (16), 2839-2851.
144. Sung, Y.; Campa, F.; Shih, W.-C., Open-source do-it-yourself multi-color fluorescence smartphone microscopy. *Biomedical optics express* **2017,** *8* (11), 5075-5086.
145. Ong, D.; Poljak, M., Smartphones as mobile microbiological laboratories. *Clinical Microbiology and Infection* **2020,** *26* (4), 421-424.
146. Barton, D., *Comprehensive natural products chemistry*. Newnes: 1999.
147. Lando, D. Y.; Haroutiunian, S.; Kulʹ ba, A.; Dalian, E.; Orioli, P.; Mangani, S.; Akhrem, A., Theoretical and experimental study of DNA helix-coil transition in acidic and alkaline medium. *Journal of Biomolecular Structure and Dynamics* **1994,** *12* (2), 355-366.
148. Williams, M. C.; Wenner, J. R.; Rouzina, I.; Bloomfield, V. A., Effect of pH on the overstretching transition of double-stranded DNA: evidence of force-induced DNA melting. *Biophysical Journal* **2001,** *80* (2), 874-881.